

Top-Quark Physics at the CLIC Electron-Positron Linear Collider



CLICdp collaboration

H. Abramowicz,¹ N. Alipour Tehrani,² D. Arominski,^{2,a} Y. Benhammou,¹ M. Benoit,³
 J.-J. Blaising,⁴ M. Boronat,⁵ O. Borysov,¹ R.R. Bosley,⁶ I. Božović Jelisavčić,⁷ I. Boyko,⁸
 S. Brass,⁹ E. Brondolin,² P. Bruckman de Renstrom,¹⁰ M. Buckland,¹¹ P.N. Burrows,¹²
 M. Chefdeville,⁴ S. Chekanov,¹³ T. Coates,¹⁴ D. Dannheim,² M. Demarteau,¹³ H. Denizli,¹⁵
 G. Durieux,¹⁶ G. Eigen,¹⁷ K. Elsener,² E. Fullana,⁵ J. Fuster,⁵ M. Gabriel,¹⁸ F. Gaede,^{2,16}
 I. García,⁵ J. Goldstein,¹⁹ P. Gomis Lopez,⁵ C. Graf,¹⁸ S. Green,²⁰ C. Grefe,^{2,c} C. Grojean,^{16,21}
 A. Hoang,^{22,23} D. Hynds,^{2,d} A. Joffe,¹ J. Kalinowski,²⁴ G. Kačarević,⁷ W. Kilian,⁹
 N. van der Kolk,^{18,e} M. Krawczyk,^{†24} M. Kucharczyk,¹⁰ E. Leogrande,² T. Lesiak,¹⁰ A. Levy,¹
 I. Levy,¹ L. Linssen,² A.A. Maier,² V. Makarenko,²⁵ J.S. Marshall,²⁰ V. Martin,²⁶ V. Mateu,^{27,28}
 O. Matsedonskyi,¹⁶ J. Metcalfe,¹³ G. Milutinović Dumbelović,⁷ R.M. Munker,² Yu. Nefedov,⁸
 K. Nowak,²⁴ A. Nürnberg,^{2,f} M. Pandurović,⁷ M. Perelló,⁵ E. Perez Codina,² M. Petric,²
 F. Pitters,^{2,g} T. Price,⁶ T. Quast,^{2,h} S. Redford,^{2,i} J. Repond,¹³ A. Robson,²⁹ P. Roloff,²
 E. Ros,⁵ K. Rozwadowska,²⁴ A. Ruiz-Jimeno,³⁰ A. Sailer,² F. Salvatore,¹⁴ U. Schnoor,²
 D. Schulte,² A. Senol,¹⁵ G. Shelkov,⁸ E. Sicking,² F. Simon,¹⁸ R. Simoniello,^{2,j} P. Sopicki,¹⁰
 S. Spannagel,² S. Stapnes,² R. Ström,² M. Szalay,¹⁸ M.A. Thomson,²⁰ B. Turbiarz,¹⁰
 O. Viazlo,² M. Vicente,^{3,b} I. Vila,³⁰ M. Vos,⁵ J. Vossebeld,¹¹ M.F. Watson,⁶ N.K. Watson,⁶
 M.A. Weber,² H. Weerts,¹³ J.D. Wells,³¹ A. Widl,²² M. Williams,^{2,k} A.G. Winter,⁶ T. Wojtoń,¹⁰
 A. Wulzer,² B. Xu,²⁰ L. Xia,¹³ T. You,^{20,32} A.F. Żarnecki,²⁴ L. Zawiejski,¹⁰ C. Zhang,³³
 J. Zhang,¹³ Y. Zhang,²⁶ Z. Zhang,³¹ and A. Zhemchugov⁸

*Corresponding Editors

^aAlso at Warsaw University of Technology, Warsaw, Poland

^bAlso at CERN, Geneva, Switzerland

^cNow at University of Bonn, Bonn, Germany

^dNow at NIKHEF, Amsterdam, The Netherlands

^eNow at NIKHEF/Utrecht University

^fNow at Karlsruhe Institute of Technology, Karlsruhe, Germany

^gAlso at Vienna University of Technology, Vienna, Austria

^hAlso at RWTH Aachen University, Aachen, Germany

ⁱNow at Paul Scherrer Institute, Villigen, Switzerland

^jNow at Johannes Gutenberg Universität, Mainz, Germany

^kAlso at University of Glasgow, Glasgow, UK

[†]Deceased

- ¹*Raymond & Beverly Sackler School of Physics & Astronomy, Tel Aviv University, Tel Aviv, Israel*
- ²*CERN, Geneva, Switzerland*
- ³*Département de Physique Nucléaire et Corpusculaire (DPNC), Université de Genève, Genève, Switzerland*
- ⁴*Laboratoire d'Annecy-le-Vieux de Physique des Particules, Annecy-le-Vieux, France*
- ⁵*IFIC, CSIC-Universidad de Valencia, Valencia, Spain*
- ⁶*University of Birmingham, Birmingham, United Kingdom*
- ⁷*Vinča Institute of Nuclear Sciences, University of Belgrade, Belgrade, Serbia*
- ⁸*Joint Institute for Nuclear Research, Dubna, Russian Federation*
- ⁹*Department of Physics, University of Siegen, Siegen, Germany*
- ¹⁰*Institute of Nuclear Physics, Polish Academy of Sciences, Cracow, Poland*
- ¹¹*University of Liverpool, Liverpool, United Kingdom*
- ¹²*University of Oxford, Oxford, United Kingdom*
- ¹³*Argonne National Laboratory, Argonne, USA*
- ¹⁴*University of Sussex, Brighton, United Kingdom*
- ¹⁵*Department of Physics, Abant İzzet Baysal University, Bolu, Turkey*
- ¹⁶*DESY, Hamburg, Germany*
- ¹⁷*Department of Physics and Technology, University of Bergen, Bergen, Norway*
- ¹⁸*Max-Planck-Institut für Physik, Munich, Germany*
- ¹⁹*University of Bristol, Bristol, United Kingdom*
- ²⁰*Cavendish Laboratory, University of Cambridge, Cambridge, United Kingdom*
- ²¹*Institut für Physik, Humboldt-Universität zu Berlin, Berlin, Germany*
- ²²*Faculty of Physics, University of Vienna, Vienna, Austria*
- ²³*Erwin Schrödinger International Institute for Mathematical Physics, University of Vienna, Vienna, Austria*
- ²⁴*Faculty of Physics, University of Warsaw, Warsaw, Poland*
- ²⁵*National Scientific and Educational Centre of Particle and High Energy Physics, Belarusian State University, Minsk, Belarus*
- ²⁶*University of Edinburgh, Edinburgh, United Kingdom*
- ²⁷*Departamento de Física Fundamental and IUFFyM, Universidad de Salamanca, Salamanca, Spain*
- ²⁸*Instituto de Física Teórica, CSIC-Universidad Autónoma de Madrid, Madrid, Spain*
- ²⁹*University of Glasgow, Glasgow, United Kingdom*
- ³⁰*IFCA, CSIC-Universidad de Cantabria, Santander, Spain*
- ³¹*Physics Department, University of Michigan, Ann Arbor, MI, USA*
- ³²*DAMTP, University of Cambridge, Cambridge, United Kingdom*
- ³³*Institute of High Energy Physics, Chinese Academy of Sciences, Beijing, China*

E-mail: clidp-top-paper-editors@cern.ch

ABSTRACT: The Compact Linear Collider (CLIC) is a proposed future high-luminosity linear electron-positron collider operating at three energy stages, with nominal centre-of-mass energies $\sqrt{s} = 380\text{ GeV}$, 1.5 TeV , and 3 TeV . Its aim is to explore the energy frontier, providing sensitivity to physics beyond the Standard Model (BSM) and precision measurements of Standard Model processes with an emphasis on Higgs boson and top-quark physics. The opportunities for top-quark physics at CLIC are discussed in this paper. The initial stage of operation focuses on top-quark pair production measurements, as well as the search for rare flavour-changing neutral current (FCNC) top-quark decays. It also includes a top-quark pair production threshold scan around 350 GeV which provides a precise measurement of the top-quark mass in a well-defined theoretical framework. At the higher-energy stages, studies are made of top-quark pairs produced in association with other particles. A study of $t\bar{t}H$ production including the extraction of the top Yukawa coupling is presented as well as a study of vector boson fusion (VBF) production, which gives direct access to high-energy electroweak interactions. Operation above 1 TeV leads to more highly collimated jet environments where dedicated methods are used to analyse the jet constituents. These techniques enable studies of the top-quark pair production, and hence the sensitivity to BSM physics, to be extended to higher energies. This paper also includes phenomenological interpretations that may be performed using the results from the extensive top-quark physics programme at CLIC.

KEYWORDS: Electron-positron collisions, Top quark physics

ARXIV EPRINT: [1807.02441](https://arxiv.org/abs/1807.02441)

Contents

1	Introduction	1
2	Experimental environment at CLIC	2
2.1	Accelerator and beam conditions	2
2.2	Staging scenario	3
2.3	Detectors	3
3	Theoretical description of top-quark production and decay	4
3.1	Overview of top-quark production at CLIC	4
3.2	Top-quark mass schemes	7
3.3	$t\bar{t}$ production at threshold	8
3.4	QCD and electroweak corrections to $t\bar{t}$ and $t\bar{t}H$ in the continuum	9
3.5	EFT interpretations of electroweak couplings	9
3.6	Beyond Standard Model (BSM) top-quark decay	11
4	Event generation, detector simulation, and reconstruction	12
4.1	Event generation	12
4.2	Detector simulation	13
4.3	Reconstruction	13
5	Boosted top-quark tagging	14
5.1	Top tagging algorithm and performance	15
6	Top-quark mass measurements at the initial energy stage	18
6.1	Threshold scan around 350 GeV	18
6.2	Top-quark mass from radiative events at 380 GeV	23
6.3	Direct top-quark mass reconstruction in the continuum at 380 GeV	25
7	Kinematic properties of top-quark pair production	26
7.1	$t\bar{t}$ production at 380 GeV	30
7.2	Radiative events at 1.4 TeV	33
7.3	Boosted event topologies	37
7.4	Cross section and asymmetry measurements	41
7.5	Systematic uncertainties	42
8	Associated $t\bar{t}$ production processes at high energy	43
8.1	Study of $t\bar{t}H$ production	43
8.1.1	Cross section measurement and top Yukawa coupling	43
8.1.2	CP mixing in the $t\bar{t}H$ coupling	45
8.2	Vector boson fusion production	46

9	Flavour-changing neutral current top-quark decays	48
9.1	$t \rightarrow c\gamma$	49
9.2	$t \rightarrow cH$	51
9.3	$t \rightarrow c\cancel{E}$	53
10	Phenomenological interpretations	57
10.1	General top-philic interpretation	57
10.2	Top-quark compositeness	60
11	Summary and conclusions	62
A	Additional event selection tables	72
A.1	Radiative events at 1.4 TeV	72

1 Introduction

As the heaviest known fundamental particle, the top quark provides a unique probe of the Standard Model (SM) of particle physics and occupies an important role in many theories of new physics beyond the SM (BSM). So far the top quark has been produced only in hadron collisions, at the Tevatron and Large Hadron Collider (LHC); however, top-quark production in electron-positron collisions would herald a new frontier of complementary and improved precision measurements. For example: a top-quark pair production threshold scan would provide a precise measurement of the top-quark mass, which is a fundamental SM parameter; precise measurements of top-quark production observables could give unique sensitivity to new physics effects, as could the search for rare top-quark decays; new particles could be observed that couple preferentially to top quarks; and improved measurements of the top Yukawa coupling could illuminate the Higgs sector.

The Compact Linear Collider (CLIC) is a proposed multi-TeV high-luminosity linear e^+e^- collider that is currently under development as a possible large-scale installation at CERN. It is based on a novel two-beam acceleration technique that can reach accelerating gradients of 100 MV/m. CLIC is proposed as a staged collider providing high-luminosity e^+e^- collisions at centre-of-mass energies, \sqrt{s} , from a few hundred GeV up to 3 TeV [1]. Top-quark pair production is accessible at the first energy stage, and an energy scan over the $t\bar{t}$ production threshold is also proposed. The higher-energy stages will supplement the initial energy datasets with large samples of top quarks, further enhancing the sensitivity to new physics.

The following sections describe the CLIC experimental conditions, an overview of top-quark production at CLIC, and the simulation and event reconstruction used for the subsequent studies, including dedicated identification of boosted top quarks. Thereafter, sections are dedicated to measurements of the top-quark mass, top-quark pair production, the study of the associated production of top quarks and a Higgs boson, and searches for rare flavour-changing neutral current (FCNC) top-quark decays. Measurements are considered at all energy stages of the collider. Finally, the

$\sqrt{s} =$	380 GeV	1.5 TeV	3 TeV
Total instantaneous luminosity / $10^{34} \text{ cm}^{-2} \text{ s}^{-1}$	1.5	3.7	5.9
Total integrated luminosity / ab^{-1}	0.5	1.5	3
Fraction of luminosity above 99% of \sqrt{s}	60%	38%	34%

Table 1: Instantaneous and integrated luminosities for the baseline CLIC staging scenario, and fraction of the luminosity delivered above 99% of \sqrt{s} [1].

phenomenological interpretation of these measurements is discussed. The work is carried out in the context of the CLIC Detector and Physics (CLICdp) collaboration.

2 Experimental environment at CLIC

The CLIC accelerator technology produces a unique beam structure that results in the need for specially-developed detector concepts to allow precise reconstruction of complex final states up to multi-TeV centre-of-mass energies. The accelerator, energy staging, and detector concepts are introduced in the following sections.

2.1 Accelerator and beam conditions

CLIC is based on room-temperature accelerating structures in a two-beam scheme. Power from a low-energy, high-current drive beam is extracted to generate radio-frequency power at 12 GHz, which is used to accelerate the main particle beams. Accelerating gradients exceeding 100 MV/m have been demonstrated at the CLIC test facility, CTF3 [2].

Each bunch train consists of 312 bunches (352 bunches for the initial energy stage) with 0.5 ns between bunch crossings at the interaction point, with a bunch train repetition rate of 50 Hz. The beam emittance is reduced in damping rings in the injector complex, and very small emittances are maintained through the accelerator chain, so that the resulting beams are highly-focused and intense. This results in significant beamstrahlungⁱ [3], which means that although the average number of hard e^+e^- interactions per single bunch train crossing is less than one, there are high rates of two-photon processes that deposit additional energy in the detector [4]. Furthermore, the beamstrahlung results in a long lower-energy tail to the luminosity spectrum, as shown in Figure 1 for operation at $\sqrt{s} = 380 \text{ GeV}$ and 3 TeV [4, 5]. The fractions of the total luminosity delivered above 99% of the nominal \sqrt{s} are given in Table 1, and the effect is seen to be particularly significant at $\sqrt{s} > 1 \text{ TeV}$. The CLIC detector design and event reconstruction techniques are optimised to mitigate the influence of the beam-induced backgrounds, as discussed in Section 4.3. The impact of ISR on the effective centre-of-mass energy is similar to that of beamstrahlung.

The baseline accelerator design allows for up to $\pm 80\%$ longitudinal electron spin polarisation by using GaAs-type cathodes [3]; positron polarisation is a possible upgrade option.

ⁱRadiation of photons from the colliding electrons or positrons in the electric field of the other beam.

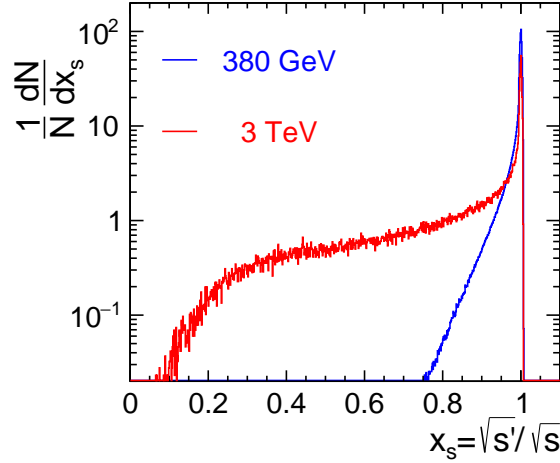


Figure 1: The luminosity spectra for CLIC operating at $\sqrt{s} = 380\text{ GeV}$ and 3 TeV , where x_s denotes the ratio of the effective centre-of-mass energy after beamstrahlung, $\sqrt{s'}$, to the nominal centre-of-mass energy \sqrt{s} [4, 5].

2.2 Staging scenario

To maximise the physics potential of CLIC, runs are foreseen at three energy stages [1]. Initial operation is at $\sqrt{s} = 380\text{ GeV}$, and will also incorporate an energy scan over the $t\bar{t}$ production threshold around $\sqrt{s} = 350\text{ GeV}$. The second stage is at $\sqrt{s} = 1.5\text{ TeV}$, which is the highest collision energy reachable with a single CLIC drive beam complex. The second-stage energy of 1.5 TeV has recently been adopted and will be used for future studies. In the work presented here, the previous baseline of 1.4 TeV is used. The third stage of $\sqrt{s} = 3\text{ TeV}$ is the ultimate energy of CLIC and features two drive beam complexes. The expected instantaneous and total luminosities are given in Table 1. For the staging scenario assumed in this paper, each stage will consist of four to five years of operation.

2.3 Detectors

The detector concepts, CLIC_ILD and CLIC_SiD, used for the CLIC physics studies described here and elsewhere [6], are adapted from the ILD [7, 8] and SiD [8, 9] detector concepts for the International Linear Collider (ILC). Design modifications are motivated by the smaller bunch spacing and different beam conditions as well as the higher-energy collisions at CLIC; both detectors are optimised for 3 TeV . The two detector concepts, shown schematically in Figure 2, are discussed in detail in [4]. The detectors are described using a right-handed coordinate system with the z -axis along the electron beam direction, and θ denotes the polar angle from the z -axis. CLIC_SiD employs central silicon-strip tracking detectors, whereas CLIC_ILD includes a large central gaseous time projection chamber. In both concepts, the central tracking system is supplemented by silicon-pixel inner tracking detectors.

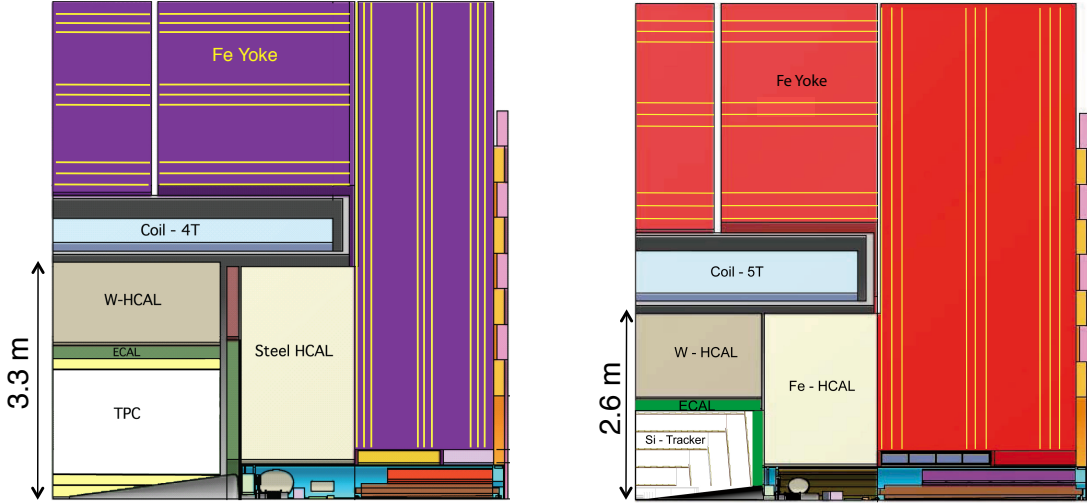


Figure 2: Longitudinal cross section of the top right quadrant of the CLIC_ILD (left) and CLIC_SiD (right) detector concepts [4].

Vertex and tracking systems provide excellent track momentum resolution of $\sigma_{p_T}/p_T^2 \lesssim 2 \cdot 10^{-5} \text{ GeV}^{-1}$ needed for the reconstruction of high- p_T charged leptons, as well as high impact parameter resolution, defined by $a \lesssim 5 \mu\text{m}$ and $b \lesssim 15 \mu\text{m GeV}$ in $\sigma_{d_0}^2 = a^2 + b^2/(p^2 \sin^3 \theta)$. This allows accurate vertex reconstruction and enables flavour tagging with clean b-, c- and light-quark jet separation, crucial for top-quark identification and background rejection at the initial CLIC energy stage. In highly-boosted top-quark events, a significant fraction of the resulting b-hadrons decay outside the vertex detector, and the jet environment is dense, motivating the development of alternative approaches to top-quark reconstruction that do not depend on flavour tagging.

Fine-grained electromagnetic and hadronic calorimeters (ECAL and HCAL) are optimised for particle-flow reconstruction, which aims to reconstruct individual particles within a jet using the combined tracking and calorimeter measurements. The resulting jet-energy resolution, for isolated central light-quark jets with energy in the range 100 GeV to 1 TeV, is $\sigma_E/E \lesssim 3.5\%$. Strong solenoidal magnets located outside the HCAL provide an axial magnetic field of 4 T in CLIC_ILD and 5 T in CLIC_SiD. Two compact electromagnetic calorimeters in the forward region, LumiCal and BeamCal, allow electrons and photons to be measured down to around 10 mrad in polar angle; this is particularly important for the determination of the luminosity spectrum via measurements of Bhabha scattering [10].

3 Theoretical description of top-quark production and decay

3.1 Overview of top-quark production at CLIC

Operation at the initial CLIC energy stage, $\sqrt{s} = 380 \text{ GeV}$, will allow top-quark pair production with close to maximal cross section as illustrated in Figure 3. The expected cross section, includ-

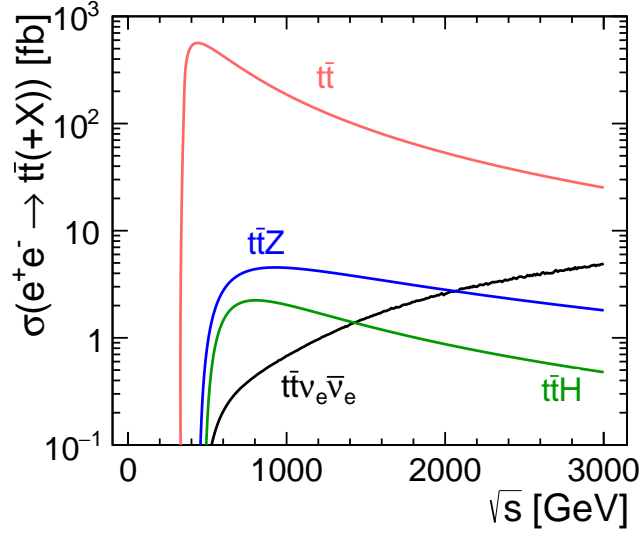


Figure 3: Cross section as a function of centre-of-mass energy for the main top-quark pair production processes at an e^+e^- collider for a top-quark mass of $m_t = 174$ GeV and a Higgs boson mass of $m_H = 125$ GeV. The leading-order expectations for unpolarised beams with initial-state radiation are shown. The effect of beamstrahlung is not included.

ing higher-order quantum chromodynamics (QCD) effects and with initial-state radiation, is about 700 fb for unpolarised beams [11].

Top-quark pair production is dominated by the Z^*/γ^* exchange diagram shown in Figure 4a. The dominant top-quark decay mode in the SM is to a b-quark and W boson (about 99.8%). The topology of the $t\bar{t} \rightarrow 6$ -fermion final state is defined by the decay channels of the two W bosons. Most of the analyses described in this paper consider fully-hadronic events, where both W bosons decay hadronically, or semi-leptonic events, where one of the W bosons decays to a lepton and a neutrino and the other W boson decays hadronically. Fully-leptonic events, which account for about 11% of the events, have not been studied so far.

The contribution from non- $t\bar{t}$ processes, such as single-top production (see Figure 4b) and triple gauge boson production, to the inclusive $e^+e^- \rightarrow 6$ -fermion process cannot be fully separated due to interference. At $\sqrt{s} = 380$ GeV its contribution to the final event sample is expected to be negligible. In contrast, at higher centre-of-mass energies where the fraction of non- $t\bar{t}$ events is significantly larger [12], such events make up the main part of the remaining background after all selections have been applied.

All three energy stages contribute to the determination of the electroweak couplings of the top quark by analysis of $t\bar{t}$ production. These measurements make use of the electron beam polarisation available at CLIC: the cross section for $e^+e^- \rightarrow t\bar{t}$ is enhanced (reduced) by 34% at 380 GeV for the -80% (+80%) polarisation configuration; and at the higher-energy stages, the cross section is 30% larger (smaller) when operating with -80% (+80%) beam polarisation.

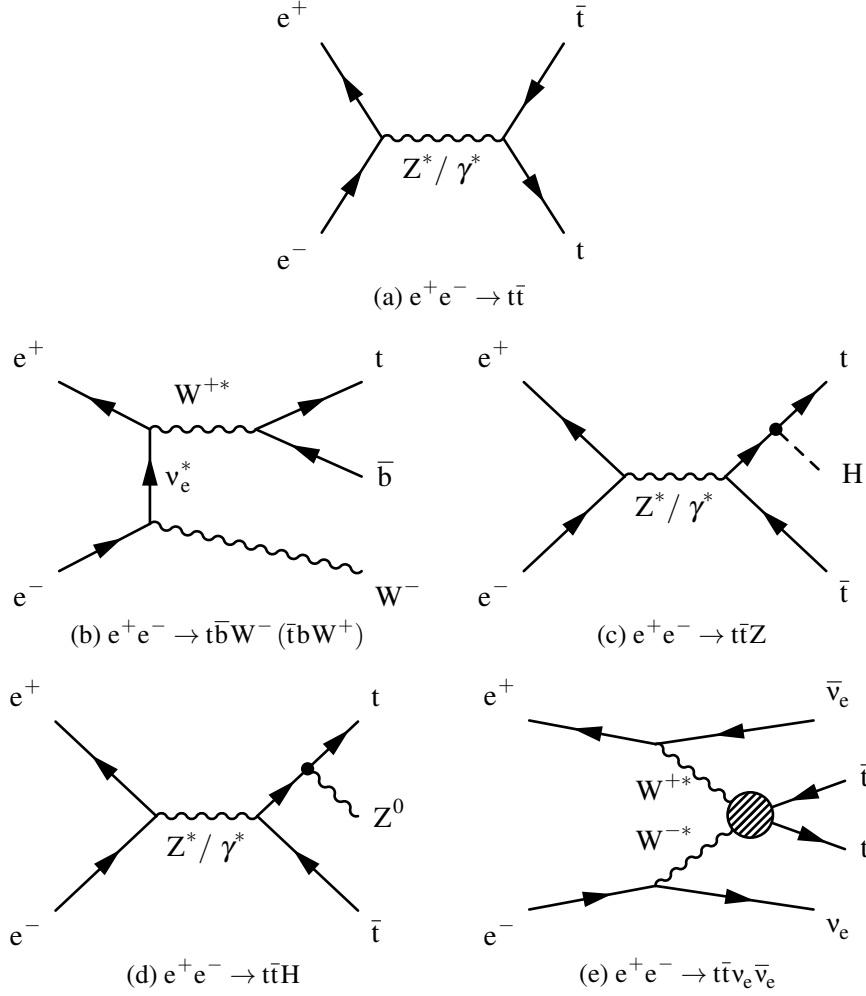


Figure 4: Relevant top-quark production processes at CLIC; (a) $t\bar{t}$, (b) single-top, (c) $t\bar{t}Z$, (d) $t\bar{t}H$, (e) $t\bar{t}\nu_e\bar{\nu}_e$.

At higher energies, processes where the top-quark pair is produced in association with other particles are accessible, see for example [Figure 4c](#) and [Figure 4d](#). The $t\bar{t}H$ cross section has a maximum around $\sqrt{s} = 800$ GeV. This process enables direct measurements of the top Yukawa coupling and allows the study of CP properties of the Higgs boson in the $t\bar{t}H$ coupling. As the luminosity of a linear collider increases with the centre-of-mass energy, the optimal energy in terms of yield at which to study this process is above the maximum of the cross section. The energy stage at 1.5 TeV (or the previous baseline of 1.4 TeV as used here) is ideally suited for studying this process as the production rate is close to its maximum.

The cross section for top-quark pair production in vector boson fusion (VBF), such as $e^+e^- \rightarrow t\bar{t}\nu_e\bar{\nu}_e$ (see [Figure 4e](#)), has an approximately logarithmic increase with the centre-of-mass energy. Hence, studies of such processes benefit from the highest possible centre-of-mass energy available at CLIC.

The cross sections and expected numbers of events for the processes discussed above are sum-

$\sqrt{s} =$	380 GeV	1.4 TeV	3 TeV
$\sigma(e^+e^- \rightarrow t\bar{t})$	723 fb	102 fb	25.2 fb
$\sigma(e^+e^- \rightarrow t\bar{t}H)$	-	1.42 fb	0.478 fb
$\sigma(e^+e^- \rightarrow t\bar{t}v_e\bar{v}_e)$	-	1.33 fb	4.86 fb
$\int \frac{d\mathcal{L}}{ds'} ds'$	500 fb^{-1}	$1,500 \text{ fb}^{-1}$	$3,000 \text{ fb}^{-1}$
No. $t\bar{t}$ events	346,000	216,000	157,800
No. $t\bar{t}H$ events	-	2,370	2,140
No. $t\bar{t}v_e\bar{v}_e$ events	-	1,590	11,300

Table 2: Unpolarised cross sections for $t\bar{t}$, $t\bar{t}H$ and $t\bar{t}v_e\bar{v}_e$ production assuming $m_t = 174 \text{ GeV}$ and $m_H = 125 \text{ GeV}$ at the three centre-of-mass energies studied in this paper. The numbers for 380 GeV include QCD corrections (see text) while leading-order results are given for the higher energy stages. $\sqrt{s'}$ is the effective centre-of-mass energy of the e^+e^- collision. The presented cross sections include the effects of initial state radiation but not the effects of beamstrahlung. Also given are numbers of expected events, including both effects. The presented cross sections and event numbers do not include possible enhancements from polarised beams.

marised in [Table 2](#).

3.2 Top-quark mass schemes

Observables with the highest sensitivity to the top-quark mass are related to production thresholds or resonances involving the top quark. However, the fact that the top quark is unstable and coloured causes nontrivial and in general sizeable QCD and electroweak corrections, which currently can be systematically controlled only for a small number of observables (such as for the $t\bar{t}$ threshold). At the level of currently achievable experimental uncertainties for top-quark mass measurements these corrections, which significantly modify the simple leading-order picture of a particle with a definite mass that decays to an observable final state, cannot be neglected. Most experimental studies of the top-quark mass therefore rely on multi-purpose MC event generators to measure a parameter of the generator associated with the top-quark mass. The interpretation of these top-quark mass measurements relies on the quality of the MC modelling of the observables used, and also suffers from the fact that the exact field theoretical interpretation of the MC top-quark mass parameter is not fully understood.

In theory calculations, different mass schemes are used, which are renormalisation-scale dependent. A common scheme is the “pole mass”, defined as the pole of the quark propagator. The top-quark pole mass is numerically close to the mass parameter of the generator but may not be identified with it; another scheme that has a close numerical relation to the generator mass parameter is the MSR mass, see for example [13]. In precision calculations at high energies, the $\overline{\text{MS}}$ (modified minimal subtraction) mass scheme is frequently used. However, for the treatment of the threshold region (shown in [Figure 5](#)), neither the pole mass nor the $\overline{\text{MS}}$ mass is adequate, since they both show

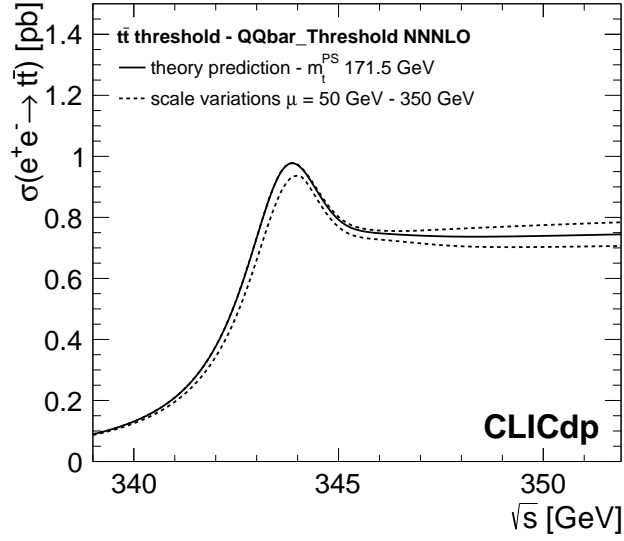


Figure 5: Cross section of top-quark pair production in the threshold region, showing the NNNLO QCD theory cross section obtained with `QQbar_threshold` [22] and the associated renormalisation scale uncertainties.

poor convergence and are subject to larger QCD corrections. At the threshold, two commonly used mass schemes are the 1S [14] and the PS [15] mass schemes, both of which result in stable behaviour of the calculated cross section in the threshold region and can also be related to the $\overline{\text{MS}}$ mass in a theoretically rigorous way with high precision [16], for use in other perturbative calculations. Additional uncertainties from the precision of the strong coupling constant enter into this conversion.

For the studies at the top-quark pair production threshold discussed in Section 3.3 and 6.1, the PS mass scheme is used, assuming a top-quark mass of $m_t^{\text{PS}} = 171.5$ GeV. With the assumed value of the strong coupling constant of 0.1185, this value corresponds to a top-quark pole mass of 173.3 GeV, which is consistent with measurements of the pole mass at the LHC [17, 18]. Since the numerical value of the mass parameter in the event generator is close to the pole mass, the mass used in the threshold studies is also consistent with the top-quark mass used to generate event samples for the other analyses in this paper, as presented in Section 4.1.

3.3 $t\bar{t}$ production at threshold

Top-quark pair production in the threshold region (340-355 GeV) is characterised by a fast rise of the cross section induced by the formation of a quasi toponium bound state, and by additional higher-order effects from interactions of the quark pair, predominantly via the strong interaction [19–21], but also via Higgs boson exchange.

Figure 5 shows the cross section of the process $e^+e^- \rightarrow t\bar{t}$ as a function of centre-of-mass energy calculated at next-to-next-to-next-to-leading order (NNNLO) QCD [22], taking next-to-leading or-

der (NLO) Higgs effects and electroweak effects into account. Theoretical uncertainties obtained from variations of the renormalisation scale are also indicated. Consistent predictions with comparable uncertainties are provided also by NNLO + NNLL calculations containing logarithmic corrections to all orders not included in the NNNLO results [23]. The observable cross section is obtained by including effects from initial state radiation and the luminosity spectrum of the collider, as discussed in more detail in [Section 6.1](#).

The cross section, the position of the turn-on of the top-quark pair production, and the overall shape of the cross section as a function of collision energy are strongly dependent on the precise value of the top-quark mass as well as on the width, the Yukawa coupling, and the strength of the strong coupling [19–21, 24, 25]. A precise measurement of the top-quark pair threshold line shape can thus be used to extract the top-quark mass to excellent precision and with a rigorously defined mass scheme as introduced in [Section 3.2](#), and can also be used to obtain other top-quark properties [26–28].

3.4 QCD and electroweak corrections to $t\bar{t}$ and $t\bar{t}H$ in the continuum

The fully differential cross section for top-quark pair production at lepton colliders was computed in [29–31] at next-to-next-to-leading order (NNLO) in QCD. In the continuum region, i.e. for collider energies above around 400 GeV, scale uncertainties on the relevant observables such as the total cross section, the top-quark forward-backward asymmetry (A_{FB}), and the differential top-quark p_T distribution are at the few per mille level [31]. While top-quark decays can be directly included in these calculations by working in the narrow-width approximation, a full treatment of finite-width effects requires instead computing $W^+W^-b\bar{b}$ production, which is known only at NLO in QCD [32–34]. Automated NLO computations of these processes are available in WHIZARD [35] and MADGRAPH5_AMC@NLO [36]. The same tools also allow simulation of top-quark pair production in association with a Higgs or a Z boson at NLO in QCD and including finite-width effects. Electroweak NLO corrections [37–39] are known to be sizeable at high energy, reaching order 20% on the total cross section and A_{FB} for a 1 TeV collider [40]. They will thus play a role in the high-energy stages of CLIC. The resummation of log-enhanced QCD effects might also be important in the regime of boosted top quarks. Such calculations have been performed for the LHC [41] and for lepton colliders [42, 43]. It is expected that a complete treatment of these effects for all the relevant observables will be available for CLIC data analyses.

3.5 EFT interpretations of electroweak couplings

BSM effects induced by heavy new physics (above the direct reach of CLIC) are universally described by Effective Field Theory (EFT) operators of energy dimension (d) larger than 4 that modify the low-energy dynamics with respect to SM predictions. Lower-dimensional operators normally [44] induce larger effects, and by assuming lepton (and baryon) number conservation the first EFT operators are those of dimension $d = 6$. We thus restrict this study to $d = 6$ operators and employ, whenever possible, the “Warsaw basis” notation [44], where a complete non-redundant basis for these operators was first presented. The EFT Lagrangian is expressed as a sum over local

operators Q_i multiplied by coupling constants C_i , referred to as (dimensionful) Wilson coefficients:

$$\mathcal{L}_{\text{EFT}} = \mathcal{L}_{\text{SM}} + \sum_i C_i Q_i^{d=6}.$$

The $d = 6$ operators that contribute, at tree-level, to top-quark production at lepton colliders are conveniently classified as follows. “Universal” operators [45–47] emerge from the direct couplings of heavy BSM particles to the SM gauge and Higgs bosons. Given that such couplings are unavoidable in any BSM scenario that is connected with EW or EW symmetry-breaking physics, universal operators are very robust BSM probes. Universal operators do contribute to top-quark physics; however, they also produce correlated effects in a variety of other processes such as di-lepton, di-boson, associated Higgs boson production, and vector boson scattering processes. Since they are expected to be probed better in these other channels, we will not consider them here. Relevant operators are instead the ones, dubbed “top-philic”, that emerge from the direct BSM coupling to the top-quark fields $q = \{t_L, b_L\}$ and $t = t_R$.ⁱⁱ There are valid reasons, supported by concrete BSM scenarios (see Section 10 for a discussion), to expect strong new physics couplings with the top quark, and consequently enhanced top-philic operator coefficients. Top-philic effects can thus be more effective indirect probes of new physics than the universal ones, where such an enhancement might not appear.

The top-philic operators are identified by first classifying all the $d = 6$ gauge-invariant operators involving q and t fields, plus an arbitrary number of derivative and bosonic SM fields.ⁱⁱⁱ Next, we apply Equations of Motion (EOM) and other identities to write each of them as a linear combination of Warsaw basis operators [44] and we identify the independent combinations. This results in the nine top-philic operators, listed in Table 3, which will be focused on in this document. Note that because of the usage of the EOM for the gauge fields, some of the top-philic operators involve more than just q , t and the bosonic fields. For instance $Q_{l,t,B}$ is a four-fermion lepton-top-quark operator that emerges from

$$\bar{t}\gamma^\mu t D^\nu B_{\mu\nu} \stackrel{\text{EOM}}{=} -\frac{g'}{2} Q_{\varphi t} + g' Q_{l,t,B} + \dots,$$

where g' is the hypercharge coupling, and the dots stand for four-fermion operators involving the top-quark, light quarks and leptons other than the electron. The latter ones can be safely ignored in the present analysis. Similarly one can construct $Q_{lq,B}$ and $Q_{l,t,W}$, for a total of three four-fermion operators that are specific linear combinations of the 4 four-fermion operators that contribute to $e^+e^- \rightarrow t\bar{t}$, identified in [49]. Operators of this kind induce effects that grow quadratically with the centre-of-mass energy, hence they can be very efficiently probed by the high-energy stages of CLIC.

Operators that belong neither to the universal nor to the top-philic categories are due to sizable BSM couplings to the light fermions, a possibility that is generically disfavoured by flavour constraints for relatively light new physics, in the range of 10 – 100 TeV. Operators in this class can thus be generated only in BSM scenarios with exotic flavour structures, hence they would be more

ⁱⁱTop-philic operators have also been adopted as one of the standards for top-quark measurements at the LHC [48].

ⁱⁱⁱWe ignore operators with gluon fields because they do not contribute at leading order to the final states considered in this paper.

$Q_{\phi t} = (\phi^\dagger i \overleftrightarrow{D}_\mu \phi) (\bar{t} \gamma^\mu t)$
$Q_{t\phi} = (\phi^\dagger \phi) (\bar{q} t \tilde{\phi})$
$Q_{tB} = (\bar{q} \sigma^{\mu\nu} t) \tilde{\phi} B_{\mu\nu}$
$Q_{\phi q}^{(1)} = (\phi^\dagger i \overleftrightarrow{D}_\mu \phi) (\bar{q} \gamma^\mu q)$
$Q_{\phi q}^{(3)} = (\phi^\dagger i \overleftrightarrow{D}_\mu^I \phi) (\bar{q} \tau^I \gamma^\mu q)$
$Q_{tW} = (\bar{q} \sigma^{\mu\nu} t) \tau^I \tilde{\phi} W_{\mu\nu}^I$

$Q_{lt,B} = (\bar{t} \gamma^\mu t) (\bar{e} \gamma_\mu e + \frac{1}{2} \bar{l} \gamma_\mu l) \stackrel{\text{EOM}}{=} \frac{1}{2} Q_{\phi t} + \frac{1}{g} \bar{t} \gamma^\mu t D^\nu B_{\mu\nu} + \dots$
$Q_{lq,B} = (\bar{q} \gamma^\mu q) (\bar{e} \gamma_\mu e + \frac{1}{2} \bar{l} \gamma_\mu l) \stackrel{\text{EOM}}{=} \frac{1}{2} Q_{\phi q}^{(1)} + \frac{1}{g} \bar{q} \gamma^\mu q D^\nu B_{\mu\nu} + \dots$
$Q_{lq,W} = (\bar{q} \tau^I \gamma^\mu q) (\bar{l} \tau^I \gamma_\mu l) \stackrel{\text{EOM}}{=} -Q_{\phi q}^{(3)} - \frac{2}{g} \bar{q} \tau^I \gamma^\mu q D^\nu W_{\mu\nu}^I + \dots$

Table 3: The top-philic operators. All the conventions and the operator names are those in Ref. [44], with the exception of $Q_{lt,B}$, $Q_{lq,B}$ and $Q_{lq,W}$, which are linear combinations of Warsaw basis four-fermion operators.

conveniently studied in the context of specific flavour models. For this reason we restrict the EFT analysis presented in this paper to top-philic BSM scenarios ^{iv}.

3.6 Beyond Standard Model (BSM) top-quark decay

One of the possible ways to look for possible BSM physics effects in top-quark physics at CLIC is the search for rare top-quark decays. With more than half a million top quarks and anti-quarks expected at the initial stage of $\sqrt{s} = 380$ GeV, discoveries or limits down to branching fractions of about 10^{-5} should be reachable. FCNC top-quark decays, $t \rightarrow qX$ ($q = u, c$; $X = \gamma, g, Z, H$) ^v, are of particular interest as they are very strongly suppressed in the SM. They are forbidden at tree level, and the loop level contributions are suppressed by the GIM-mechanism [50]. The suppression is not perfect because of the non-negligible b-quark mass; the corresponding partial widths are proportional to the square of the element V_{qb} of the CKM-quark-mixing matrix [51, 52] and to the fourth power of the ratio of the b quark and W boson masses. These suppression factors ^{vi} result in extremely small branching ratios. For decays involving a charm quark, SM expectations [53] are:

$$\begin{aligned}
\text{BR}(t \rightarrow cg) &\sim 5 \cdot 10^{-12}, \\
\text{BR}(t \rightarrow c\gamma) &\sim 5 \cdot 10^{-14}, \\
\text{BR}(t \rightarrow cZ) &\sim 1 \cdot 10^{-14}, \\
\text{BR}(t \rightarrow cH) &\sim 3 \cdot 10^{-15}.
\end{aligned}$$

^{iv}Note that when describing the CLIC capabilities to detect exotic top-quark decays we will implicitly be probing operators of the above mentioned type, however we will not phrase those results in the EFT language, but rather in terms of sensitivity to the branching ratios.

^vCharge conjugation is implied unless explicitly stated otherwise.

^{vi}The GIM mechanism is not strictly applicable to the $t \rightarrow cH$ channel as the Higgs coupling is proportional to the quark mass. Still, the expected FCNC branching ratio for this channel is the smallest in the SM.

The SM expectations for decays with an up quark in the final state decrease by another two orders of magnitude [53]. Observation of decays involving either a charm or up quark would therefore constitute a direct signature for BSM physics.

Many extensions of the SM predict significant enhancements of the FCNC top-quark decays [53]. These enhancements can be due to FCNC couplings at tree level, but in most models they result from contributions of new particles or from modified particle couplings at the loop level. For most BSM scenarios, significant deviations in the (light) Higgs boson couplings or contributions from additional Higgs bosons to the loop diagrams result in the significant enhancement of the $t \rightarrow cH$ decay. For the Two Higgs Doublet Model (2HDM), which is one of the simplest extensions of the SM, loop contributions can be enhanced up to the level of $BR \sim 10^{-4}$ [54]. For the “non-standard” scenarios, 2HDM(III) or “Top 2HDM”, where one of the Higgs doublets only couples to the top quark, tree level FCNC couplings are also allowed. Here an enhancement of up to 10^{-2} is possible [55]. For the $t \rightarrow c\gamma$ decay, enhancement up to the level of 10^{-5} is possible for some supersymmetric models with R -parity violation [56]. For an overview of top-quark FCNC predictions for different BSM scenarios see [53].

In the study presented here, the FCNC couplings involving the charm quark are considered, as they are expected to be favoured in many BSM scenarios. This also allows us to take advantage of the c -tagging capabilities of the CLIC detector. Three channels selected for detailed study (see Section 9) are: $t \rightarrow c\gamma$, $t \rightarrow cH$, and $t \rightarrow c\cancel{E}$ where a top quark decays into a c -jet and invisible heavy particle.

4 Event generation, detector simulation, and reconstruction

The results reported here are based on detailed Monte Carlo (MC) simulation studies with GEANT4 [57, 58] based simulations of the CLIC detector concepts and a full event reconstruction, unless indicated otherwise. All relevant background processes are included. Event simulation and reconstruction is performed using the ILCDIRAC grid production tools [59, 60].

4.1 Event generation

The signal processes and main physics backgrounds, with up to six particles in the final state, are generated using the WHIZARD 1.95 [61] program. ISR is described using the leading logarithmic approximation structure function [62] including hard collinear photons up to the third order. For many analyses only the backgrounds from e^+e^- collisions contribute. However, for some studies it is important also to include MC event samples from $e^+\gamma$, γe^- , and $\gamma\gamma$ interactions, with photons originating from beamstrahlung. In all cases the expected energy spectra for the CLIC beams, including the effects from beamstrahlung and the intrinsic energy spread, are used for the initial-state electrons, positrons and beamstrahlung photons. Low- Q^2 processes with quasi-real photons are described using the Weizsäcker-Williams approximation as implemented in WHIZARD.

The process of fragmentation and hadronisation is simulated using PYTHIA 6.4 [63] with a parameter set tuned to OPAL e^+e^- data recorded at LEP [64] (see [4] for details). The impact of

other PYTHIA tunes in top-quark pair production events is illustrated in [65]. The decays of τ leptons are simulated using TAUOLA [66]. The MC samples for the study of the top Yukawa coupling measurement (see Section 8.1) with eight final-state fermions are obtained using the PHYSSIM [67] package; again PYTHIA is used for fragmentation and hadronisation. The mass of the Higgs boson is taken to be 125 GeV and the decays of the Higgs boson are simulated using PYTHIA with the branching fractions listed in [68]. Apart from the special MC samples used for the threshold and radiative top-quark mass studies, the top-quark mass is set to $m_t = 174.0$ GeV.

4.2 Detector simulation

The GEANT4 detector simulation toolkits MOKKA [69] and SLIC [70] are used to simulate the detector response to the generated events in the CLIC_ILD and CLIC_SiD concepts, respectively. The QGSP_BERT physics list is used to model the hadronic interactions of particles in the detectors. The digitisation, i.e. the translation of the raw simulated energy deposits into detector signals, is performed using the MARLIN [71] and `org.lcsim` [72] software packages.

The most important beam-induced background are particles from the $\gamma\gamma \rightarrow$ hadrons process, a result of the high bunch charge density at high collision energy. These interactions are simulated separately using PYTHIA 6.4 [63] with the photon spectra from GUINEAPIG [73]. Events corresponding to 60 bunch crossings are superimposed on the physics events before digitisation; this is equivalent to 30 ns and is much longer than the offline reconstruction window, which is assumed to be 10 ns around the hard physics event. At $\sqrt{s} = 380$ GeV, the impact of this background is found to be small, but is larger at $\sqrt{s} = 3$ TeV, where approximately 1.2 TeV of energy is deposited in the calorimeters during the 10 ns time window [4].

4.3 Reconstruction

Track reconstruction is performed using the MARLIN and, for the CLIC_SiD detector model, the `org.lcsim` software packages. Calorimeter clustering and particle flow reconstruction is performed using PANDORAPFA [74–76], creating a collection of so-called Particle-Flow Objects (PFOs). Time-stamping information is used to suppress beam-related backgrounds: three levels of timing selections based on the identified particle type, p_T , and detector region define `loose`, `default`, and `tight` selections of PFOs that are used for further analysis [4]. The `loose` collection is normally used for the lower-energy running, while the `default` and `tight` collections apply more stringent selections that are found to perform better for higher-energy running.

The classification of candidate top-quark events as fully-hadronic, semi-leptonic, or fully-leptonic requires efficient identification of high-energy, isolated charged leptons. Lepton finding is optimised to identify e^\pm and μ^\pm originating from the decay of W bosons^{vii}; these leptons are typically of much higher energy than those coming from hadronic decays inside quark jets, and are well-separated from other activity in the event. Isolated leptons candidates are identified by studying their energy depositions in the ECAL and HCAL, impact parameters, and isolation in a cone

^{vii} τ^\pm leptons are searched for using a dedicated TauFinder [77] algorithm implemented in MARLIN. The algorithm studies the presence of highly energetic and low-multiplicity jets in the detector.

around each input track. The lepton charge is determined by the curvature of the helix from a standard Kalman-filter-based track reconstruction of the associated hits in the tracking system.

In most cases, jet clustering is performed by the FASTJET package [78], in exclusive mode. Both the longitudinally-invariant k_t algorithm [79, 80] and the VLC algorithm [81] are used; these are sequential recombination algorithms that are found to give better robustness against $\gamma\gamma \rightarrow \text{hadrons}$ than traditional lepton collider jet clustering algorithms [4, 75, 81, 82]. The former uses the particle transverse momenta p_T and angular separation $\Delta R_{ij}^2 = (y_i - y_j)^2 + (\phi_i - \phi_j)^2$, where y_i and ϕ_i are the rapidity and azimuth of particle i , to compute a clustering distance parameter $d_{ij} = \min(p_{Ti}^2, p_{Tj}^2) \Delta R_{ij}^2 / R^2$, where R is the radius parameter that determines the maximum area of the jet. The VLC algorithm uses the particle energies E , and angular separation θ , to compute a clustering distance parameter $d_{ij} = 2 \min(E_i^{2\beta}, E_j^{2\beta}) (1 - \cos \theta_{ij}) / R^2$. Here, β regulates the clustering order; the default choice is $\beta = 1.0$ unless otherwise specified.

Both algorithms are effective for identifying particles that are likely to have originated from beam-beam backgrounds; if particles are found to be closer to the beam axis than to other particles then they are removed from the event, which mitigates the effect of $\gamma\gamma \rightarrow \text{hadrons}$ pile-up. For the k_t algorithm, the distance to the beam axis is measured by $d_{iB} = p_{Ti}^2$ and for the VLC algorithm by $d_{iB} = E_i^{2\beta} \sin^2 \theta_{iB}^\gamma$, where the γ parameter controls the rate of shrinking in jet size in the forward region; the default choice is $\gamma = 1.0$ unless otherwise specified. The jet clustering algorithm is chosen and optimised for each analysis to achieve the best balance between losing signal particles and including extra background particles.

Flavour tagging is essential for the identification and combinatoric assignment of top-quark events. Vertex reconstruction and heavy-flavour tagging is performed by the LCFIPLUS program [83]. This consists of a topological vertex finder that reconstructs secondary interactions, and a neural network-based classifier that provides b- and c-jet probabilities for each jet reconstructed in the event, based on variables such as the number of tracks, track impact parameters, decay lengths, and vertex masses. For analyses heavily dependent on flavour-tagging, LCFIPLUS is also used for jet clustering on the secondary vertices, using the same algorithms discussed above, to improve the tagging performance.

5 Boosted top-quark tagging

At the higher energy stages of CLIC, a large proportion of the top quarks in $e^+e^- \rightarrow t\bar{t}$ events is produced with significant boosts leading to a more collimated jet environment. In particular, the topology is very different from that of top quarks produced close to the production threshold. Traditional methods, based on b-tagging and the combination of individual jets to form top-quark candidates, may not be efficient at these high collision energies since the separation between the individual top-quark decay products in general is too small. In this section we present a method exploiting the internal sub-structure of typically large- R jets. This plays an important role in the physics programme, extending the physics reach to higher energies.

The reconstruction of boosted top quarks was studied in full simulation using the CLIC_ILD de-

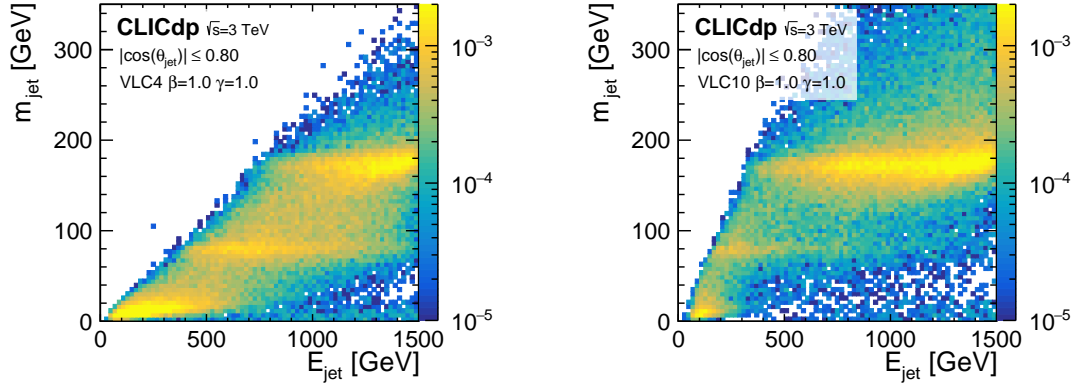


Figure 6: Normalised distribution of the number of events as a function of reconstructed jet mass and energy for fully-hadronic $t\bar{t}$ events at $\sqrt{s} = 3$ TeV. The particles are reconstructed into two exclusive jets using the VLC algorithm using a jet clustering radius of 0.4 (VLC4, left), and a radius of 1.0 (VLC10, right). The β and γ parameters are both set to 1.0.

tector model, including $\gamma\gamma \rightarrow \text{hadrons}$ background. Events were reconstructed into two exclusive jets using the VLC algorithm. Figure 6 shows the reconstructed jet mass as a function of the reconstructed jet energy for fully-hadronic $t\bar{t}$ events in CLIC at $\sqrt{s} = 3$ TeV, for two different choices of jet clustering radius. As expected, the jet clustering performs well for jets at higher energy, while the ability to capture the full top-quark jet is significantly reduced below ~ 800 GeV, for the typical jet radius of 0.4. The use of a large radius, as illustrated in the right figure, significantly improves the reach to lower energy, extending the coverage down to ~ 500 GeV.

The optimal jet radius for boosted $t\bar{t}$ events at $\sqrt{s} = 1.4$ TeV and $\sqrt{s} = 3$ TeV was found to be $R = 1.4$ and $R = 1.0$, respectively. The optimisation was done for hadronically decaying top quarks with a polar angle θ satisfying the condition^{viii} $37^\circ \leq \theta \leq 143^\circ$ and for events with a reconstructed collision energy above 1.2 TeV or 2.6 TeV, respectively^{ix}. The optimal jet clustering parameters were selected as the best trade-off between achieving a narrow top-quark mass peak and minimal loss of energy in the forward direction that would produce a fake jet mass peak at m_W . The resulting large- R jets serve as input for the top tagger algorithm described below.

5.1 Top tagging algorithm and performance

The tagging of boosted top quarks at CLIC is based on the Johns Hopkins top tagger [84] as implemented in FASTJET [78, 85]. This tagger is explicitly designed for the identification of top quarks by recursively iterating through a jet cluster to search for up to three or four hard subjets and then imposing mass constraints on these subjets. This procedure provides strong discrimination power for hadronically decaying top quarks against QCD-induced light parton jets. Although the

^{viii}The detector coverage goes down to about 8° . Excluding a larger area in the forward direction for the optimisation reduces the effect of losing energy down the beam pipe and adds some margin for the finite size of the jets.

^{ix}Using the definition of reconstructed collision energy as outlined in Section 7.3

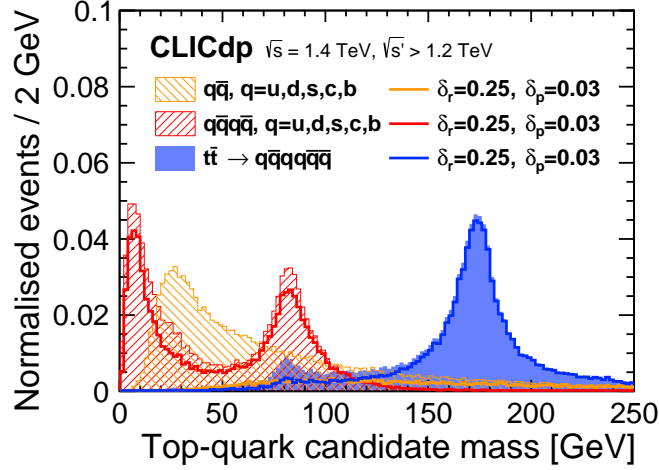


Figure 7: Reconstructed top-quark candidate mass distributions at $\sqrt{s} = 1.4$ TeV for events with $\sqrt{s'} \geq 1.2$ TeV. The filled distributions represent the top-quark candidate mass before application of the top tagger and are normalised to unity. The solid lines show the effect of applying the de-clustering procedure outlined in the text. Note that additional cuts on the invariant mass of both the top-quark and W candidates are applied in a later step. Fully-hadronic $t\bar{t}$ events are shown in blue, four-jet events in red, and dijet events in orange. A cut, $|\cos \theta| \leq 0.95$, is applied on the polar angle of the individual top and light quarks.

method was originally designed for fully-hadronic $t\bar{t}$ events in hadron colliders, in this paper it is applied to the hadronically decaying top quark in semi-leptonic $t\bar{t}$ events in CLIC, see [Section 7.3](#).

The tagging is based on an iterative de-clustering of the input jet and is carried out by reversing each step of the jet clustering. The algorithm is governed by two parameters: δ_r , the subjet distance; and δ_p , the fraction of subjet p_T relative to the p_T of the input jet. These parameters control whether to accept the objects, resulting from the split, as subjets for further de-clustering or whether, for example, the de-clustering should continue only on the harder of the two objects. An object is rejected if its p_T fraction is lower than δ_p or if its distance to another objects is smaller than δ_r . The de-clustering loop is terminated when two successive splittings have been accepted resulting in two, three, or four subjets of the input jet. The case with two final subjets is rejected and the other cases are further analysed. The input jet is considered to be top-tagged if the total invariant mass of the subjets is within ± 55 GeV of m_t and one subjet pair has an invariant mass within ± 30 GeV of m_W .

The optimisation and efficiency of the tagging algorithm was studied using fully-hadronic $t\bar{t}$ events, four-jet events $q\bar{q}q\bar{q}$ (u, d, s, c, b), and dijet events $q\bar{q}$ (u, d, s, c, b). Since the background environment at a lepton collider is substantially lower than at a hadron collider, a higher fake rate is acceptable and the optimisation of the algorithm is tuned to a high-efficiency operating point for the fully-hadronic $t\bar{t}$ sample. The corresponding top tagger parameters are chosen by minimising the fake rate from four-jet events resulting in $\delta_p = 0.25$ (0.11) and $\delta_r = 0.03$ (0.03), for the samples at $\sqrt{s} = 1.4$ (3) TeV, respectively. [Figure 7](#) shows the reconstructed top-quark candidate mass before

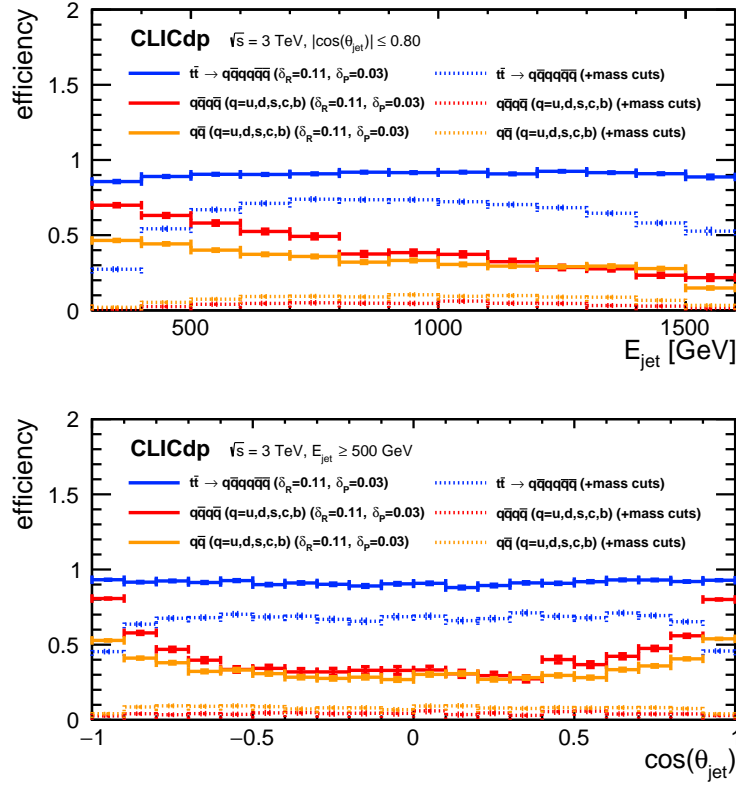


Figure 8: Top tagger efficiency for fully-hadronic $t\bar{t}$ events (blue), four-jet events (red), and dijet events (orange) as function of jet energy (top) and jet polar angle θ (bottom). The solid lines show the effect of applying the de-clustering procedure outlined in the text, while the dashed lines show the efficiency including also the cuts on the reconstructed invariant mass of the top-quark and W candidates.

and after application of the top tagger declustering step for operation at $\sqrt{s} = 1.4$ TeV. A small peak close to m_W is clearly seen for the $t\bar{t}$ distribution (blue) and is caused by top-quark events not fully captured by the large- R jet.

The resulting efficiency for top-quark jets from the $\sqrt{s} = 3$ TeV dataset is 69% in the central region of the detector (defined as $|\cos \theta| \leq 0.8$) and with an energy in the range from 500 GeV to 1500 GeV. The corresponding fake rate is 4.4% (8.8%) for jets from the four-jet (di-jet) background sample^x. The resulting efficiency for top-quark jets from the $\sqrt{s} = 1.4$ TeV dataset is 71% in the central region of the detector (defined as $|\cos \theta| \leq 0.8$) and with an energy in the range from 400 GeV to 700 GeV. The corresponding fake rate is 5.7% (6.9%) for jets from the four-jet (di-jet) background sample. Figure 8 shows the top-quark tagging efficiency from the $\sqrt{s} = 3$ TeV dataset as a function of the large- R jet energy (top) and polar angle θ (bottom). As expected, the efficiency drops at energies below 500 GeV where the jets are no longer sufficiently boosted to be contained

^xAlternatively, adopting a tighter operating point at $\sqrt{s} = 3$ TeV results in a top-quark jet efficiency of 54% and a fake rate of 2.7% (3.7%)

within one large- R jet. The slightly lower efficiency for large jet energies is also anticipated and is mainly due to a more challenging environment for the PANDORAPFA algorithm and the subject de-clustering. Furthermore, the limited detector acceptance in the forward direction reduces the efficiency in the corresponding region significantly.

The top tagger performs about 23% better than a simple cut on the reconstructed large- R jet mass in the corresponding range (within ± 55 GeV of m_t). In addition, the declustering procedure provides additional handles on the jet substructure such as the mass and kinematic variables of the W boson candidate and the reconstructed helicity angle θ_W that examine whether the subjects are consistent with a top decay^{xi}. As illustrated in [Section 7](#), these handles are useful to discriminate against the remaining background events.

6 Top-quark mass measurements at the initial energy stage

A precise measurement of the mass of the top quark is one of the key objectives of the top-physics programme at CLIC. Conceptually, there are two different approaches to this measurement.

The first is the determination of the top-quark mass from measurements of the top-quark pair production cross section. These measurements can either be carried out directly, in a dedicated energy scan of the top-quark pair production threshold (see [Section 6.1](#)), or for radiative events at higher collision energies (see [Section 6.2](#)). The advantage of this approach is that the top-quark mass is extracted in well-defined mass schemes, as introduced in [Section 3.2](#).

The second approach is the measurement of the mass from kinematic observables reconstructed in continuum production, such as the measurement of the invariant mass of the decay products of top quarks (see [Section 6.3](#)). Since the extracted mass value is obtained as a parameter of the event generators used in template fits, this technique suffers from ambiguities in the interpretation comparable to the issues encountered in most top-quark mass measurements at the LHC. On the other hand, the higher integrated luminosities collected well above the top-quark production threshold provide high statistics.

A combination of both classes of measurements may ultimately help to better constrain the systematics and to improve the theoretical understanding of the continuum reconstruction, also contributing to the interpretation of the top-quark measurements at hadron colliders.

6.1 Threshold scan around 350 GeV

At e^+e^- colliders, the top-quark mass is expected to be measured with high accuracy in a scan of the top-quark pair production threshold [[19–21](#), [25](#)]. Earlier studies have shown that a statistical precision of a few tens of MeV on the top-quark mass is achievable in such measurements when performed simultaneously with a fit to determine physical parameters such as the strong coupling constant or the top Yukawa coupling [[26–28](#)].

^{xi}The helicity angle is measured in the rest frame of the reconstructed W boson and is defined as the opening angle of the top quark to the softer of the two W boson decay subjects. Too shallow an angle would be an indication of a false splitting, where one of the pairs of subjects produces a small mass compatible with QCD-like emission.

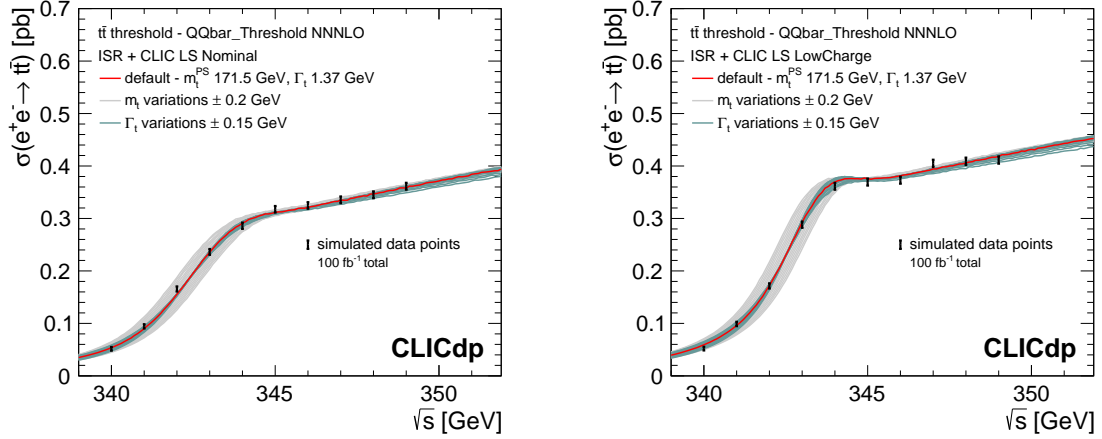


Figure 9: Illustration of a top-quark threshold scan at CLIC with a total integrated luminosity of 100 fb^{-1} , for two scenarios for the luminosity spectrum, nominal (left) and LowCharge (right). The bands around the central cross section curve show the dependence of the cross section on the top-quark mass and width, illustrating the sensitivity of the threshold scan. The error bars on the simulated data points show the statistical uncertainties of the cross section measurement, taking into account signal efficiencies and background levels.

The analysis is based on the study discussed in detail in [27], which uses signal and background reconstruction efficiencies slightly above threshold, obtained from full detector simulations for the CLIC_ILD detector concept. The emphasis of the event selection is on maximising the signal significance and it considers both fully-hadronic as well as semi-leptonic events, the latter excluding τ final states. The selection proceeds through the identification of isolated charged leptons, jet clustering into either six or four exclusive jets, flavour-tagging, and pairing of W boson candidates and b-jets into the two top-quark candidates via a kinematic fit. The constraints imposed by the kinematic fit already result in a substantial rejection of background. The kinematic fit is followed by an additional background rejection cut making use of a binned likelihood function combining flavour tagging information event shape and kinematic variables. After this selection, a highly pure sample of top-quark pair events is available for the measurement of the cross section. An overall signal selection efficiency of 70.2%, including the relevant branching fractions, is achieved, whereas the dominant background channels are rejected at the 99.8% level, resulting in an effective cross section of 73 fb for the remaining background.

The analysis is combined with higher order theory calculations of the signal process. Here, the latest NNNLO QCD calculations, available in the program `QQbar_threshold` [22], are used. The theory cross section is corrected for ISR and the luminosity spectrum of the collider using the techniques described in [27]. This corrected cross section is then used to generate pseudo data and the templates needed to fit the simulated data points to extract the top quark mass.

For the threshold scan, a baseline scenario of ten equidistant points is assumed, with 10 fb per point and a point-to-point spacing of 1 GeV, in the energy range from $2m_t^{\text{PS}} - 3 \text{ GeV}$ to $2m_t^{\text{PS}} + 6 \text{ GeV}$. Such a threshold scan is shown in Figure 9, for two luminosity spectrum scenarios discussed below.

The bands illustrate the dependence of the cross section on the generated top-quark mass and width. The error bars on the data points are statistical, taking into account signal efficiencies and background levels. The top quark mass is extracted using a template fit to the measured cross sections as a function of centre-of-mass energy. The cross section templates are simulated for different input mass values. The top-quark width is given by the SM expectation provided by `QQbar_threshold`, which is around 1.37 GeV for the range of masses considered here. For the calculation of the templates the width corresponding to the respective mass is used. The extraction of the mass is performed directly in the PS mass scheme.

The luminosity spectrum of CLIC has a strong impact on the shape of the cross section in the threshold region, which influences the extraction of top-quark properties. The smearing of the turn-on behaviour and the would-be 1S peak of the cross section depends on the level of beamstrahlung and the beam energy spread. A larger beam energy spread results in a more pronounced tail to lower energies while the level of beamstrahlung influences the behaviour in the resonance region and above, reducing the effective cross section. Both of these effects result in a broadening of the threshold curve. This in turn reduces the statistical sensitivity of a mass measurement for a given total integrated luminosity, and degrades the precision for the combined extraction of several top-quark properties, such as mass and width or mass and Yukawa coupling. The beam energy spread and the level of beamstrahlung can be tuned by modifying the bunch charge and the beam focusing, allowing optimisation of the spectrum specifically for a top-quark threshold scan. This illustrates well the flexibility of CLIC to optimise the luminosity spectrum without physically changing the accelerator. This aspect might also be useful for other physics applications such potential threshold scans for newly discovered particles. However, an improvement of the quality of the luminosity

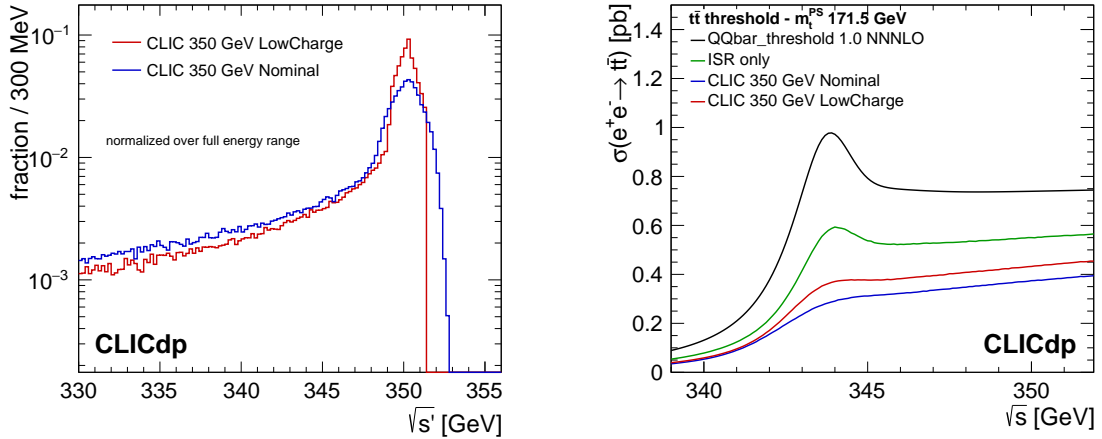


Figure 10: Two scenarios of the CLIC luminosity spectrum for a threshold scan (left); one based on the nominal accelerator parameters of the 380 GeV initial stage of CLIC (optimised for instantaneous luminosity), and one optimised for reduced beamstrahlung (“LowCharge”). The impact of the luminosity spectra on the top-quark pair production cross section, where the blue and red curves show the visible cross section for the nominal and the LowCharge luminosity spectra, respectively (right).

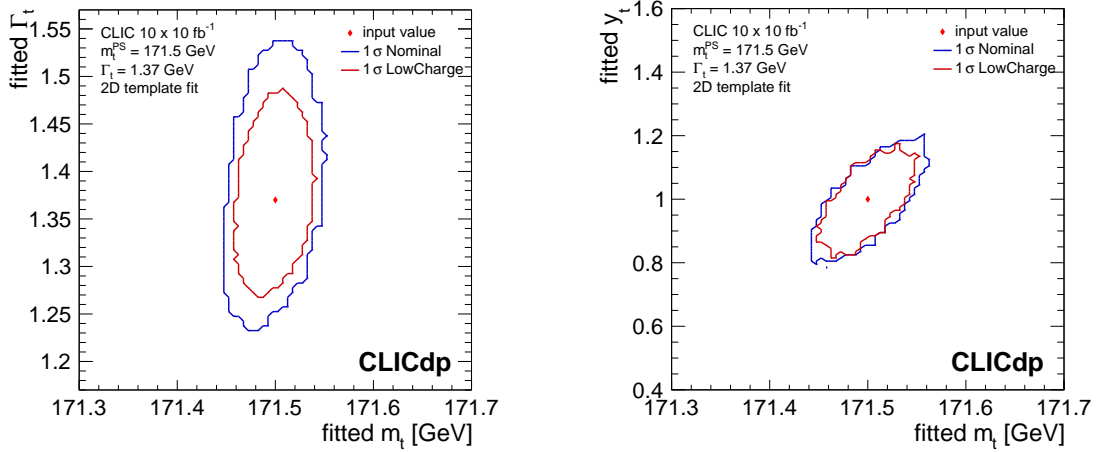


Figure 11: 1σ statistical uncertainty contours of two-parameter fits to the top threshold region, combining the top-quark mass and width (left) and the top-quark mass and the top Yukawa coupling (right). The contours are shown for both the nominal luminosity spectrum and the “LowCharge” option, in both cases assuming an integrated luminosity of 100 fb^{-1} .

spectrum also results in a reduction of the instantaneous luminosity.

Figure 10 shows the effects of initial state radiation only, and of ISR and the luminosity spectrum combined on the top-quark pair production cross section. Here, two scenarios for the luminosity spectrum at the threshold are considered: one based on the nominal accelerator parameters optimised for luminosity (denoted “nominal luminosity spectrum”), and one with a reduced beam energy spread and correspondingly a narrower and more pronounced main luminosity peak, using a bunch charge reduced to 70% of the nominal charge (denoted “LowCharge luminosity spectrum”) [5]. For the latter scenario, the instantaneous luminosity is reduced by 50% compared to the nominal parameters, resulting in a two-fold increase of the required running time for a 100 fb^{-1} threshold scan.

The expected statistical uncertainty for the top-quark mass in the PS scheme, assuming equal integrated luminosity of 100 fb^{-1} , is 23 (19) MeV for the nominal (LowCharge) luminosity spectrum. From running time considerations alone, the ‘LowCharge’ luminosity spectrum does not offer advantages for the top-quark mass measurement. This conclusion changes when extending the analysis to other parameters such as the top-quark width or Yukawa coupling. As is apparent from the width of the green band representing the effect of changes in top-quark width in Figure 9, the sensitivity to the width is considerably lower using the nominal luminosity spectrum compared with the LowCharge scenario. Figure 11 shows the 1σ -contours for a simultaneous fit of the top-quark mass and width (left) and top-quark mass and the Yukawa coupling (right). In particular, for the combined extraction of the mass and the width, the LowCharge option provides an improved resolution that compensates the penalty of the reduced luminosity.

It should also be noted that the energy points for the threshold scan, and the integrated luminosities recorded at each, can be optimised to maximise the precision for a given observable. Owing to the steeper turn-on behaviour of the cross section in the LowCharge option, the potential for this

Table 4: The impact of QCD scale uncertainties at NNNLO and of uncertainties of the strong coupling constant on the measured top-quark mass in a threshold scan. The parametric uncertainty originating from the strong coupling corresponds to an uncertainty of 0.001 in α_s . The sign of the change in mass is opposite to the sign of the change in α_s .

	Δm_t^{PS} nominal spectrum	Δm_t^{PS} LowCharge spectrum
QCD scale uncertainties	$\pm 42 \text{ MeV}$	$\pm 40 \text{ MeV}$
parametric α_s	$\mp 30 \text{ MeV}$	$\mp 27 \text{ MeV}$

optimisation is expected to be bigger in this case, in particular for measurements of the mass and width.

Systematic uncertainties in a threshold scan

Given the high statistical precision of the top-quark mass measurement at threshold, systematic uncertainties are likely to limit the ultimate precision. Various sources of uncertainties have been investigated, including beam energy [27], knowledge of the luminosity spectrum [86], selection efficiencies and residual background levels [27], non-resonant contributions [12, 87–91], parametric uncertainties from the strong coupling [92], and theoretical uncertainties estimated from factorisation and renormalisation scale variations [92, 93].

The combined theoretical and parametric uncertainties are expected to be in the range 30 MeV to 50 MeV, depending on assumptions on the expected improvement in the theoretical description and the knowledge of input parameters such as the strong coupling constant. They have been evaluated for CLIC in the context of the different scenarios for the luminosity spectrum. The results are summarised in Table 4. Similarly, the combined experimental systematic uncertainties are expected to be around 25 MeV to 50 MeV. The beam energy is expected to be known with a relative uncertainty of approximately 10^{-4} , both from machine parameter measurements and from detector measurements of the luminosity spectrum peak from Bhabha scattering, where the momentum scale can be calibrated using Z boson decays with sufficient accuracy. The precision of the measurement of the total luminosity, which has a direct impact on the precision of the cross section measurement used to extract the top quark mass, is expected to be in the few per mille range [94, 95]. This results in an uncertainty on the top-quark mass of a few MeV, substantially smaller than other uncertainties considered here. As discussed above, the luminosity spectrum plays an important role in the analysis of a threshold scan, so the uncertainties of the knowledge of the spectrum are highly relevant. The studies discussed in [86] make use of a study scaled from 3 TeV [10]. A dedicated study for the 380 GeV case has recently been performed in the context of the analysis discussed in Section 6.2, which will be used in the future to further refine the uncertainty estimate for a threshold scan.

Systematic uncertainties also play an important role for the two-parameter studies shown in Figure 11. Here, the symmetrised theory uncertainties given by scale variations are 55 MeV for the top-quark width and 16% for the top Yukawa coupling. The latter is also sensitive to parametric

uncertainties from the strong coupling constant, with an uncertainty of 0.001 in α_s leading to an uncertainty 6.5% on the top Yukawa coupling.

6.2 Top-quark mass from radiative events at 380 GeV

In the continuum, the top-quark mass can be extracted from the cross section of radiative events, $e^+e^- \rightarrow t\bar{t}\gamma$, where a top-quark pair is produced in association with an energetic ISR photon radiated from the incoming electron or positron beam. This method is illustrated here using a parton-level study at $\sqrt{s} = 380$ GeV. As with the threshold scan, the top-quark mass is extracted directly in theoretically well-defined mass schemes, avoiding interpretation uncertainties. Figure 12 illustrates the dependence of the cross section on the top-quark mass as a function of the effective $t\bar{t}$ centre-of-mass energy,

$$s' = s \left(1 - \frac{2E_\gamma}{\sqrt{s}} \right),$$

where E_γ is the energy of the ISR photon. The top-quark mass is extracted from a measurement of $d\sigma_{t\bar{t}\gamma}/d\sqrt{s'}$, by fitting templates computed from:

$$\frac{d\sigma_{t\bar{t}\gamma}}{d\cos\theta d\sqrt{s'}} = \frac{\alpha_{\text{em}}}{\pi^2} g(x, \theta) \sigma_{t\bar{t}}(s').$$

Here, $g(x, \theta)$ is a calculable function of the polar angle θ of the emitted photon, and the photon energy fraction $x = E_\gamma/\sqrt{s}$. The polar angle is integrated over a range in which the photon can be measured in the detector, which excludes the photon being collinear with the incoming electron or positron. This method requires only identification, rather than complete kinematic reconstruction, of the top-quark candidates.

An accurate prediction of the $\sqrt{s'}$ distribution requires a matched calculation that includes the enhancement of the cross section at the $t\bar{t}$ production threshold from bound-state effects and remains valid at centre-of-mass energies well above threshold. The theoretical predictions used in this study are based on the NNLL renormalization group improved threshold cross section of [23], and $\mathcal{O}(\alpha_s^3)$ predictions for the continuum production [96, 97], which have been smoothly matched together [98]. The cross section for $e^+e^- \rightarrow t\bar{t} + X + \gamma_{\text{ISR}}$ factorises into the ISR photon emission from the incoming leptons and the $e^+e^- \rightarrow t\bar{t} + X$ inclusive production.

The differential cross section of the $e^+e^- \rightarrow t\bar{t} + X + \gamma_{\text{ISR}}$ process is given as a function of $\sqrt{s'}$ (or, equivalently, E_γ) for specific values of s and m_t . The input mass for the cross section is expressed in the $\overline{\text{MS}}$ scheme, although for the calculation itself the 1S [99–101] and the MSR [102–104] schemes are used. The polar angle θ of the emitted photon is limited to the interval $10^\circ < \theta < 170^\circ$, which agrees with the acceptance of the CLIC detector. The differential distribution in $\sqrt{s'}$ is shown on the left hand side of Figure 12 for two different values of the top quark mass. The maximum sensitivity of the observable is reached at the $t\bar{t}$ pair production threshold.

The CLIC luminosity spectrum has an important effect on the observable distribution. The two dashed curves on the left hand side of Figure 12 represent the distribution weighted by the luminosity spectrum. Compared with the ideal calculation shown in solid lines, the threshold peak is smeared out considerably. The loss of sensitivity leads to an increase of the statistical uncertainty

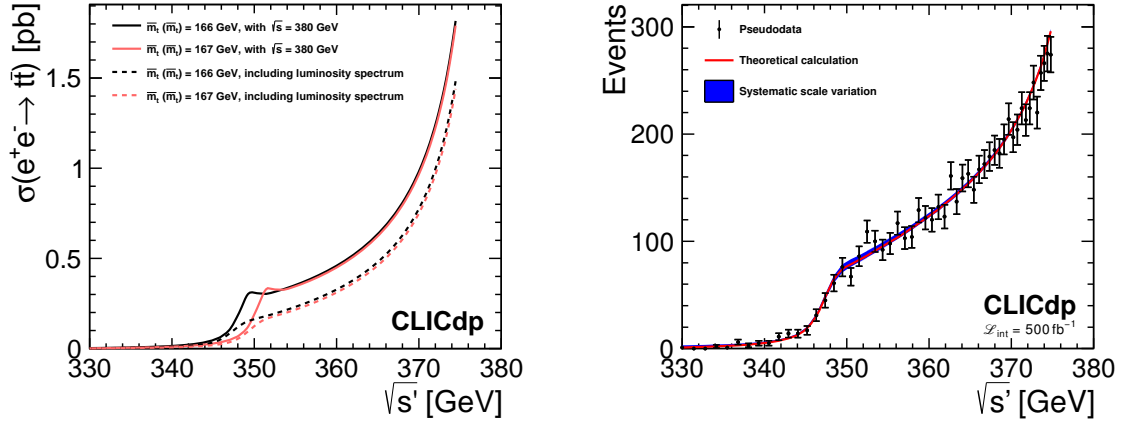


Figure 12: Prediction of the observable (left) for $\bar{m}_t(\bar{m}_t) = 166, 167$ GeV (where $\bar{m}_t(\bar{m}_t)$ denotes the top-quark mass in the $\overline{\text{MS}}$ scheme, evaluated at the top-quark mass in the $\overline{\text{MS}}$ scheme) with the matched NNLL threshold and NNLO continuum calculation for $\sqrt{s} = 380$ GeV (solid line) and folded with the CLIC luminosity spectrum (dashed line). Pseudodata (right) generated with the matched NNLL threshold and NNLO continuum calculation for $\sqrt{s} = 380$ GeV and folded with the CLIC luminosity spectrum. The markers give a statistical uncertainty estimated from the $\pm 1\sigma$ envelope of 1500 datasets of 500fb^{-1} . The binning corresponds to the expected energy resolution of the electromagnetic calorimeter. The shaded area gives the envelope of the scale variation presented in Table 5.

on the top-quark mass of $\sim 60\%$ for an integrated luminosity of 500fb^{-1} . An estimate of the statistical precision is obtained by fitting large numbers of pseudo-experiments, each corresponding to an integrated luminosity of 500fb^{-1} , to the theoretical prediction with the mass as a free parameter. Pseudodata corresponding to one mass point are shown on the right hand side of Figure 12. The distribution includes the effect of the CLIC luminosity spectrum. Assuming a selection and reconstruction efficiency of 50% for $t\bar{t}X\gamma$ radiative events, consistent with the expected $t\bar{t}$ event selection and photon reconstruction efficiency, the resulting statistical precision on the top-quark mass is 104 MeV. The propagation of the luminosity spectrum uncertainty adds an uncertainty less than 10 MeV on the top-quark mass determination.

The uncertainty on the mass measurement from theoretical uncertainties is estimated by varying the renormalisation scales used in the non-relativistic QCD (NRQCD) calculation. Two parameters, h and f , are used to vary the scales; factors of h , hf , and hf^2 are applied to the hard, soft, and ultra-soft scales, respectively. These parameters are varied in the intervals given in [105] and corresponding cross-section distributions are generated, folded with the CLIC luminosity spectrum, and fitted using the nominal distribution with the $\overline{\text{MS}}$ mass $\bar{m}_t(\bar{m}_t)$ as a free parameter. The results are shown in Table 5 and combined results in a theoretical uncertainty estimate of ± 100 MeV. The final precision on the top-quark mass is around 177 MeV for 500fb^{-1} .

h	1/2	1/2	1/2	1	1	1	2	2	2
f	1	3/2	2	2	$\sqrt{1/2}$	1	1/2	3/4	1
$\Delta\bar{m}_t(\bar{m}_t)$ [MeV]	-120	-113	-113	1	0	+1	+77	+63	+63

Table 5: Parameter variation [105] and associated shifts in the extracted value of $\bar{m}_t(\bar{m}_t)$ when fitting to the observable with the default values $(h, f) = (1, 1)$.

6.3 Direct top-quark mass reconstruction in the continuum at 380 GeV

The top-quark invariant mass can be extracted from the large sample of top-quark pairs collected above the threshold, in the continuum at 380 GeV. For this study only hadronic and semi-leptonic final states are considered. In these final states the top-quark mass can be directly reconstructed for the hadronic top-quark decay(s), without applying kinematic constraints. The VLC algorithm is applied using a radius of 1.6 ($\beta, \gamma = 0.8$) to cluster the final state hadrons into six or four exclusive jets, for hadronic and semi-leptonic event reconstruction, respectively. For suppression of four-fermion production and quark-pair production processes, which are the dominant background contributions, two jets are required to be flavour-tagged as b-jets by LCFIPLUS. This pre-selection removes about 80% of the quark-pair and 92% of the four-fermion backgrounds, while removing only about 12% of the top-pair production events.

Multivariate BDT (Boosted Decision Tree) classifiers are used for additional suppression of the non- $t\bar{t}$ background and classification of the $t\bar{t}$ candidate events as either hadronic or semi-leptonic events. The algorithms are trained separately for hadronic and semi-leptonic event selection. The classification is based on the following variables: total energy of the event, total transverse and longitudinal momenta, reconstructed missing mass, sphericity and acoplanarity of the event, number of isolated leptons, energy of isolated lepton with highest transverse momentum, minimum jet energy for the six-jet final state, minimum and maximum distance cuts for six-, four-, and two-jet reconstruction with the VLC algorithm.^{xii} Response distributions of the BDT classifier trained for selection of fully-hadronic and of semi-leptonic events are shown in Figure 13. Events having at least one of the classifier responses greater than zero are selected for mass extraction. Events which are selected in both channels are assigned to the category corresponding to the higher BDT response. The BDT classification efficiency for top-pair production events is about 90%, while the four-fermion and quark-pair production backgrounds are suppressed by a factor of about 20 and 100 respectively.

For the mass reconstruction, the jet combination that minimises a χ^2 value for the event is selected. The χ^2 formula includes constraints on the invariant masses and Lorentz boosts of the two reconstructed top-quark candidates, as well as on the two ratios of the reconstructed W boson and the parent top-quark masses. The use of the mass ratio instead of the W mass constraint is motivated by the correlation between the reconstructed masses of the W boson and the parent top quark. For

^{xii}For four- and two-jet clustering, isolated leptons are not included in the clustering.

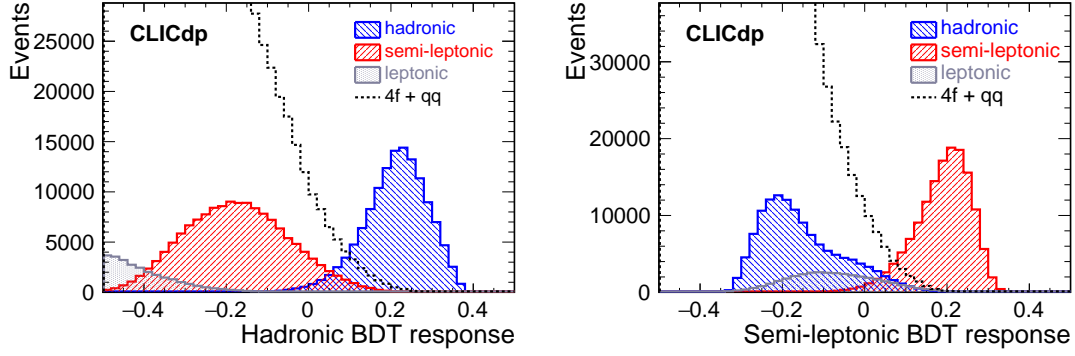


Figure 13: Response distributions for BDT classifiers trained to recognise hadronic top-quark pair events (left) and semi-leptonic top-quark pair events (right). Distributions for different samples of $t\bar{t}$ events and other SM backgrounds are compared for 500 fb^{-1} at 380 GeV CLIC.

semi-leptonic events exactly one isolated lepton (electron or muon) with energy of at least 15 GeV is required. Distributions of the reconstructed top-quark mass for hadronic and semi-leptonic top-quark pair production events are shown in Figure 14. Using a template fit method the position of the maximum in the invariant mass distribution can be extracted with a statistical uncertainty of 42 MeV and 56 MeV, for hadronic and semi-leptonic events respectively. Varying the value of the top-quark mass assumed in the χ^2 minimisation for the event reconstruction has little influence on the reconstructed peak position. The expected statistical precision on the top-quark mass, taking into account both the hadronic and the semi-leptonic channels and the dilution due to the use of the fixed mass in the χ^2 formula, is about 40 MeV.

With high statistical precision of the measurement, systematic effects could become the dominant source of the uncertainty. In particular, to match the expected level of statistical precision, the absolute jet energy scale should be controlled at the level of 0.025%. Preliminary studies suggest that this level of precision could be achieved by including a short calibration run at the Z-pole at the start of each year. A more detailed analysis is required to give a quantitative estimate of the expected jet energy scale resolution.

Systematic effects resulting from the uncertainty of the jet energy scale can be significantly reduced by relating the reconstructed top-quark mass to the mass of the W boson. The statistical uncertainty on the extracted ratio of the top-quark and W boson masses corresponds to a top-quark mass uncertainty of about 60 MeV. The measurement is hardly sensitive to the absolute jet energy scale. However, the energy scale of b-jets, relative to light-quark jets, should still be controlled to about 0.1%, to match the statistical precision.

7 Kinematic properties of top-quark pair production

The top-quark electroweak couplings are precisely determined in the SM but may receive substantial corrections from BSM physics; for example, theories with extra dimensions [106] and com-

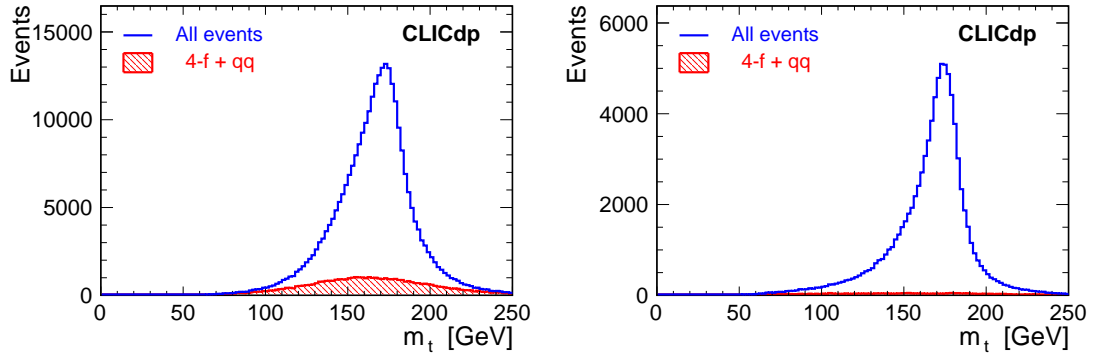


Figure 14: Distributions of the top-quark mass reconstructed from the hadronic top-quark decays for hadronic (left) and semi-leptonic (right) events, for 500 fb^{-1} at 380 GeV CLIC.

positeness [107] can modify the couplings significantly. A deviation from the SM expectation of A_{FB} for b-quarks at the Z pole was observed by the experiments operating at the electron-positron colliders SLC and LEP. This measurement is in tension with the SM prediction at the level of 2.8σ [108], and it is the most significant discrepancy of the electroweak precision data fit. Since these measurements directly involve the third family of quarks, they reinforce the importance of further precision studies of the top quark counterpart.

The precision studies of observables such as the $t\bar{t}$ production cross section, $\sigma_{t\bar{t}}$, and the top-quark forward-backward asymmetry constitute powerful tools for discovery and a deeper understanding of the nature of the electro-weak symmetry breaking. The latter is particularly important to probe and disentangle EFT operators that have a strong angular dependence. Measurements with different beam polarisation, enriching the event samples in either left-handed or right-handed top-quarks, allow to disentangle the photon and Z-boson contributions [109], while data from two (or more) different centre-of-mass energies effectively constrain BSM operators whose effects grow with energy [110, 111]. Extracting $\sigma_{t\bar{t}}$ and A_{FB} for the full CLIC staging programme, thus allows all degrees of freedom in a global fit to be constrained.

In addition, the clean environment of lepton colliders is well suited for the accurate measurement of observables that characterise the differential distributions of the top-quark scattering and decay kinematics. The extra information contained in such observables can improve the sensitivity to certain EFT operators. For example, the corrections induced by anomalous dipole moment operators (i.e., Q_{tB} and Q_{tW} in Table 3) to the distribution of the azimuthal decay angle of the top quark grow with energy, while the corresponding effect on $\sigma_{t\bar{t}}$ and A_{FB} is essentially energy-independent [111].^{xiii} Exploiting these and other differential features of the signal requires a multivariate statistical framework. For the $t\bar{t}$ analyses presented in Section 7.1 and 7.3, we adopt an approach based on “statistically optimal observables” [113–115]. This method has been used in the context of top-quark pair production at lepton colliders in [111, 113, 116–118]. The following sections describe the event selection and extraction of $\sigma_{t\bar{t}}$ and A_{FB} , while the results for the global EFT

^{xiii} Similar considerations hold for CP-violating EFT operators that could be efficiently probed by specifically designed CP-odd observables [112].

fit using these observables and the statistically optimal observables are presented in [Section 10](#).

The analyses presented in this section use the CLIC_ILD detector concept and focus on “lepton+jets” final states $t\bar{t} \rightarrow q\bar{q}q\bar{q}l\nu$, where the reconstructed charged lepton is used to determine the charge of the hadronically decaying top quark. Isolated lepton identification hence constitutes an important part of the analyses. Events without any identified leptons are discarded along with events with more than one reconstructed lepton. Further, we do not consider semi-leptonic $t\bar{t}$ events with a tau lepton as signal since these are more difficult to reconstruct because of the additional missing energy. The investigation of such events is left for future study.

After having removed the identified isolated lepton, the VLC algorithm is used to cluster the remaining particles into either two or four exclusive jets. While the former configuration is suitable at the higher energy stages where a boosted topology is expected, the latter is used for the initial stage of CLIC at 380 GeV.

For the top-quark coupling analyses presented here, we assume an even split in operation time between the two polarisation states considered: $P(e^-) = -80\%$ and $P(e^-) = +80\%$. At 380 GeV this is consistent with the current overall understanding of the CLIC physics programme. At 1.4 TeV and 3 TeV single-Higgs production in WW-fusion and the measurement of the Higgs self-coupling from the double Higgs production cross section significantly benefits from $P(e^-) = -80\%$ polarisation and hence a larger fraction of data taking in this polarisation configuration is preferred [6]. For the general top-philic interpretation discussed in [Section 10.1](#) some data with $P(e^-) = +80\%$ is needed, but a fraction lower than 50% does not degrade the results significantly.

Final states with six fermions are generally dominated by the $t\bar{t}$ production process, but have a contribution from non- $t\bar{t}$ processes such as single-top production and triple gauge boson production. An irreducible number of non- $t\bar{t}$ events is expected in the final analysis since these contributions cannot be fully separated due to interference. While no algorithm can separate them completely, attempts are made in the event selection to reduce the fraction of non- $t\bar{t}$ events using some of the characteristic features of the $t\bar{t}$ process.

$t\bar{t}$ events are simulated as part of an inclusive 6-fermion sample with final states consistent with $t\bar{t}$ production. For the analyses at $\sqrt{s} = 1.4$ TeV and $\sqrt{s} = 3$ TeV, the $t\bar{t}$ events are extracted using a parton-level categorisation requiring two on-shell top-quark candidates. Each candidate consists of three of the six final state particles and should have a mass within ~ 7.6 GeV of the generated top-quark mass; this value corresponds to five times the generated top-quark width. To stay conservative we treat the non- $t\bar{t}$ contributions as background in the following. The analyses further consider a range of additional relevant background processes as presented in the tables below. These include di-quark events as well as final states from WW- and ZZ-fusion.

The unique beam conditions at CLIC give rise to a luminosity spectrum with a peak at the nominal collision energy as shown in [Figure 1](#). This results in a distribution of effective collision energies $\sqrt{s'}$ as illustrated in [Figure 15](#), where the $t\bar{t}$ cross section is shown including the effects of beamstrahlung and ISR. This enables an extension of the $t\bar{t}$ analyses to include radiative events, with a collision energy below the nominal collision energy \sqrt{s} . Such events are studied for the 1.4 TeV dataset. In addition, we study the $t\bar{t}$ production at the nominal collision energies of 380 GeV,

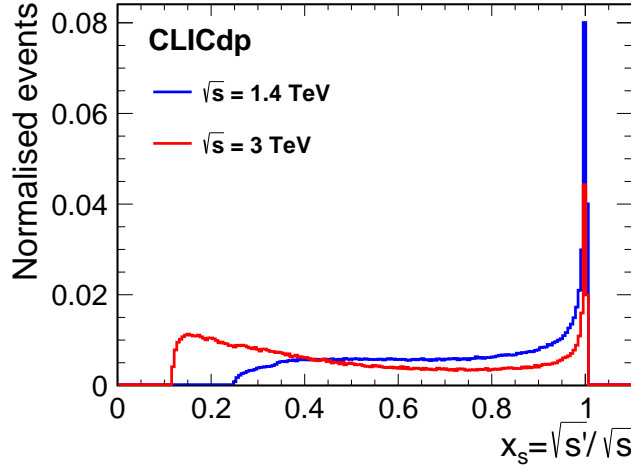


Figure 15: The $\sqrt{s'}$ distribution for $t\bar{t}$ events at $\sqrt{s} = 1.4$ (3) TeV in blue (red), including QED ISR, electroweak corrections, and the CLIC luminosity spectrum.

1.4 TeV, and 3 TeV.

The differential cross section, as a function of polar angle of the top quark in the $t\bar{t}$ centre-of-mass system, is described by

$$\frac{d\sigma}{d(\cos(\theta^*))} = \sigma_1(1 + \cos(\theta^*))^2 + \sigma_2(1 - \cos(\theta^*))^2 + \sigma_3(1 - \cos^2(\theta^*)). \quad (7.1)$$

At tree level the three terms can be related to the cross sections, $\sigma_{1,2,3}$, for producing top-quark pairs with different helicity combinations for the two top quarks in the final state with θ^* being the angle between the incoming electron and the produced top quark in the $t\bar{t}$ rest system. The forward and backward cross sections, σ_F and σ_B , can be obtained by integrating the differential cross section over the top-quark polar angle ranges, $0 < \theta^* < \pi/2$ and $\pi/2 < \theta^* < \pi$. The total production cross section, $\sigma_{t\bar{t}}$, can be expressed as $\sigma_{t\bar{t}} = \sigma_F + \sigma_B = (4/3)(2\sigma_1 + 2\sigma_2 + \sigma_3)$. The top-quark forward-backward asymmetry is defined as

$$A_{FB} \equiv \frac{\sigma_F - \sigma_B}{\sigma_F + \sigma_B} = \frac{1}{\sigma_{t\bar{t}}} 2(\sigma_1 - \sigma_2). \quad (7.2)$$

The top-quark forward-backward asymmetry and the total production cross section are extracted by fitting Equation 7.1 to the reconstructed polar-angle distribution of the hadronically decaying top quark (or anti-top quark) as calculated in the $t\bar{t}$ centre-of-mass system. Note that the sign of $\cos(\theta^*)$ is inverted for events with hadronically decaying anti-top quarks, when added into this distribution. The fit is performed after background subtraction and correction for finite selection efficiencies. The measured cross sections represent a convolution of $\sigma_{t\bar{t}}$ with the luminosity spectrum. In the analyses at $\sqrt{s} = 1.4$ TeV and 3 TeV the extraction of $\sigma_{t\bar{t}}$ is performed in a range of effective collision energies close to the nominal collision energy.

The analysis at 380 GeV is presented in Section 7.1. Radiative events are used to extract the top-quark production observables in three intervals of $\sqrt{s'}$ for operation at $\sqrt{s} = 1.4$ TeV. Here the

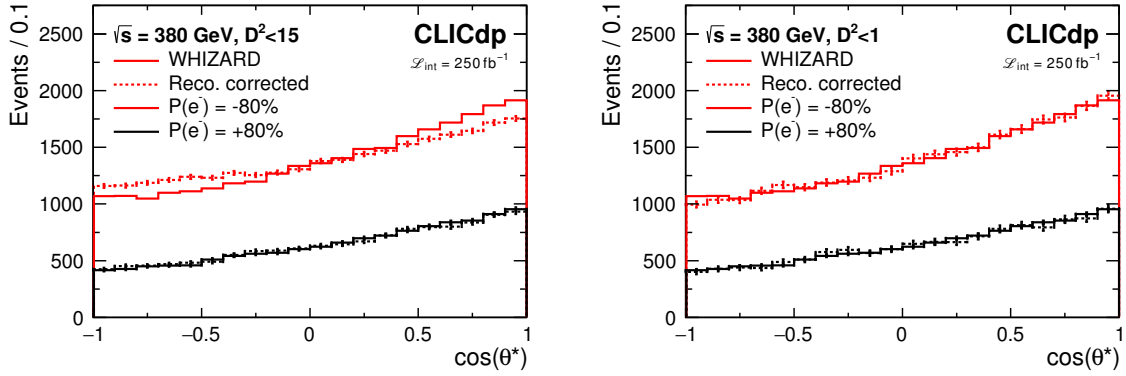


Figure 16: Top-quark polar angle distributions for operation at $\sqrt{s} = 380$ GeV after the application of a quality cut based on the kinematic variable D^2 . A cut of $D^2 < 15$ (1) was applied for the left (right) figure. The solid lines show the reconstructed distributions including the effects of detector modelling, event reconstruction and candidate selection, while the dashed lines show the WHIZARD parton-level distributions, for the two beam polarisation configurations considered. Note that efficiency corrections have been applied, corresponding to the parton-level expectation for $D^2 < 15$.

$t\bar{t}$ events are selected using a multivariate classifier including variables sensitive to the top-quark sub-structure; the analysis is presented in detail in [Section 7.2](#). Events that are either partially or substantially boosted are studied at 1.4 and 3 TeV, where we apply a dedicated tagger for identification of boosted top quarks; see a description of the tagger in [Section 5](#) and analysis in [Section 7.3](#). The results of the three analyses are presented in [Section 7.4](#), while [Section 7.5](#) includes a discussion of the dominant systematic uncertainties.

7.1 $t\bar{t}$ production at 380 GeV

At the 380 GeV stage of CLIC, top-quark candidates are formed by combining jets into larger objects. The input jets result from an initial clustering of PFOs with loose timing cuts as explained in [Section 4.3](#). The PFOs are clustered into exactly four jets using the VLC algorithm with a radius of 1.6 (β , $\gamma = 0.8$). The use of such a large jet radius is made possible by the low level of beam-induced background at 380 GeV. Note that this analysis is based on that developed in [\[109\]](#). A summary of the analysis is presented in this section; further details are available in [\[119\]](#).

The general selection relies extensively on b-tagging as well as the identification of one isolated lepton. Two jets must satisfy high and intermediate purity b-tagging selection criteria. In addition, the non-b-tagged jets are required to have an energy above 15 GeV. The b-tagging criteria are applied using the standard flavour-tagging tools described in [Section 4.3](#) and alone suppress about 97% of the dominant W^+W^- background. Lepton candidates are selected as outlined in [Section 4.3](#), with a resulting efficiency of about 85% for $t\bar{t}$ events with a leptonic decay (e, μ). The lepton candidate is removed from the list of PFOs considered for jet clustering. Additionally, we require that the p_T of the isolated lepton candidate fulfils $p_T \geq 10$ GeV.

Top-quark candidates are formed by merging the two non-b-tagged jets, that form the hadronically decaying W boson, with each of the two b-tagged jets. The ambiguity in this reconstruction is resolved by minimising the kinematic variable d^2 defined as

$$d^2 = \left(\frac{m_t - 174 \text{ GeV}}{\sigma_{m_t}} \right)^2 + \left(\frac{E_t - 190 \text{ GeV}}{\sigma_{E_t}} \right)^2 + \left(\frac{E_b^* - 68 \text{ GeV}}{\sigma_{E_b^*}} \right)^2 + \left(\frac{\cos \theta_{bW} - \langle \cos \theta_{bW} \rangle}{\sigma_{\cos \theta_{bW}}} \right)^2,$$

where m_t and E_t are the invariant mass and energy of the hadronically decaying top-quark candidate, E_b^* is the energy of the b-quark in the centre-of-mass frame of the top quark, and $\cos \theta_{bW}$ is the angle between the b-tagged jet and the W boson candidate in the lab frame. The reference values for the two first quantities correspond to the simulated values of the top-quark mass and energy, while the third quantity is the expectation value from the two-body decay kinematics of the top quark. The fourth quantity, $\langle \cos \theta_{bW} \rangle = -0.67$, is the mean of the corresponding distribution from studies using full simulation. The denominator in each term represents the width of the observed distribution. Achieving a good pairing of the jets from the hadronically decaying W boson with the associated b-tagged jet from the top-quark decay is particularly important at 380 GeV, where the event topology is isotropic and substantial mixing between the jets from the top- and anti-top quark occur.

The above jet pairing gives a source of mis-reconstruction that can lead to severe effects predominately for the $P(e^-) = -80\%$ sample that is enriched with top quarks of left-handed helicity. For top quarks with left-handed helicity, the W boson is emitted opposite to the flight-direction of the top quark and decays nearly at rest. The resulting final state has two hard jets from the b-quarks and soft jets from the hadronically decaying W boson; a configuration that leads to substantial migrations in the top-quark polar angle distribution when paired wrongly. Since the directional measurement depends very strongly on the correct association of top-quark decay particles, the final step of the analysis is carried out separately for the two polarisation states with stricter quality cuts applied for the extraction of A_{FB} for the negative beam polarisation.

The selection criteria $40 \text{ GeV} < m_W < 190 \text{ GeV}$ and $100 \text{ GeV} < m_t < 250 \text{ GeV}$ are applied to the reconstructed top candidates. Note that the loose upper cut on m_W is mainly applied to reject mis-reconstructed events. The preselection requirements on the lepton, jets and candidate top-quark defined above, efficiently reduce the number of background events as seen in [Table 6](#) and [Table 7](#).

The effect of migration in the top-quark polar angle distribution is reduced by applying a quality cut on D^2 , defined as

$$D^2 = \left(\frac{\gamma_t - \langle \gamma_t \rangle}{\sigma_{\gamma_t}} \right)^2 + \left(\frac{E_b^* - 68 \text{ GeV}}{\sigma_{E_b^*}} \right)^2 + \left(\frac{\cos \theta_{bW} - \langle \cos \theta_{bW} \rangle}{\sigma_{\cos \theta_{bW}}} \right)^2,$$

where $\langle \gamma_t \rangle = \sqrt{s}/2m_t \approx 1.09$ and σ_{γ_t} is the mean and width, respectively, of the observed distribution of the top-quark Lorentz factor obtained from studies using full simulation. [Figure 16](#) shows the top-quark polar angle distributions for the hadronically decaying top quarks in the signal sample after application of the quality cut $D^2 < 15$ ($D^2 < 1$). As expected, the effect of migration is most clearly seen for $P(e^-) = -80\%$ where the impact is reduced by placing a strict cut.

Process	σ [fb]	ϵ_{Pre} [%]	$\epsilon_{D^2 < 15}$ [%]	$\epsilon_{D^2 < 1}$ [%]	$N_{D^2 < 15}$	$N_{D^2 < 1}$
$e^+e^- \rightarrow qq\bar{q}q\bar{l}v$ ($l = e, \mu$)	161	69	93	34	25,540	9,401
$e^+e^- \rightarrow qq\bar{q}q\bar{l}v$ ($l = \tau$)	80.5	16	90	29	2,973	950
$e^+e^- \rightarrow qq\bar{q}q\bar{q}q$	215	0.61	67	6.6	220	22
$e^+e^- \rightarrow q\bar{q}l\bar{v}l\bar{v}$	61.8	5.6	58	5.5	503	48
$e^+e^- \rightarrow qq\bar{q}q$	8,910	0.01	44	2.9	113	8
$e^+e^- \rightarrow q\bar{q}l\bar{v}$	9,800	0.03	20	1.6	151	12
$e^+e^- \rightarrow q\bar{q}l\bar{l}$	1,840	0.25	43	3.4	485	38
$e^+e^- \rightarrow q\bar{q}$	26,100	0.01	32	0.57	180	3

Table 6: Pre-selection and final event selection efficiencies and expected number of events for the $t\bar{t}$ analysis of CLIC at a nominal collision energy of 380 GeV. The numbers are shown for $P(e^-) = -80\%$ assuming 250fb^{-1} .

Process	σ [fb]	ϵ_{Pre} [%]	$\epsilon_{D^2 < 15}$ [%]	$\epsilon_{D^2 < 1}$ [%]	$N_{D^2 < 15}$	$N_{D^2 < 1}$
$e^+e^- \rightarrow qq\bar{q}q\bar{l}v$ ($l = e, \mu$)	76	72	93	34	12,660	4,699
$e^+e^- \rightarrow qq\bar{q}q\bar{l}v$ ($l = \tau$)	38.1	17	89	28	1,427	456
$e^+e^- \rightarrow qq\bar{q}q\bar{q}q$	102	0.65	70	9.1	117	15
$e^+e^- \rightarrow q\bar{q}l\bar{v}l\bar{v}$	29.2	5.7	56	5.2	233	22
$e^+e^- \rightarrow qq\bar{q}q$	1,240	0.03	39	1.4	34	1
$e^+e^- \rightarrow q\bar{q}l\bar{v}$	1,360	0.03	17	0.52	17	1
$e^+e^- \rightarrow q\bar{q}l\bar{l}$	1,690	0.21	42	2.0	369	18
$e^+e^- \rightarrow q\bar{q}$	16,400	0.01	26	2.0	81	6

Table 7: Pre-selection and final event selection efficiencies and expected number of events for the $t\bar{t}$ analysis of CLIC at a nominal collision energy of 380 GeV. The numbers are shown for $P(e^-) = +80\%$ assuming 250fb^{-1} .

The signal selection efficiency for the dataset at $P(e^-) = -80\%$, relevant for the extraction of A_{FB} , is 69% after the initial pre-selection and drops to 23% when applying the quality cut $D^2 < 1$. The corresponding numbers for $P(e^-) = +80\%$ are 72% after the initial pre-selection and 67% after the application of the quality cut $D^2 < 15$. As the extraction of $\sigma_{t\bar{t}}$ is less sensitive to mis-reconstructions, a cut at $D^2 < 15$ is applied for both polarisations since it already suppresses background events efficiently. The efficiencies for signal and dominant background processes are presented in Table 6 and Table 7. Contributions from other backgrounds such as $e^+e^- \rightarrow qq\nu\bar{\nu}$ and additional six-fermion processes are found to be negligibly small.

The looser cut is also applied in the construction of the statistically optimal observables. In addition, for $P(e^-) = -80\%$, we apply an additional quality cut that puts constraints on both the leptonic and the hadronic side of the event; this reduces the efficiency by an additional $\sim 40\%$, resulting in 15,516 events in the final event sample.

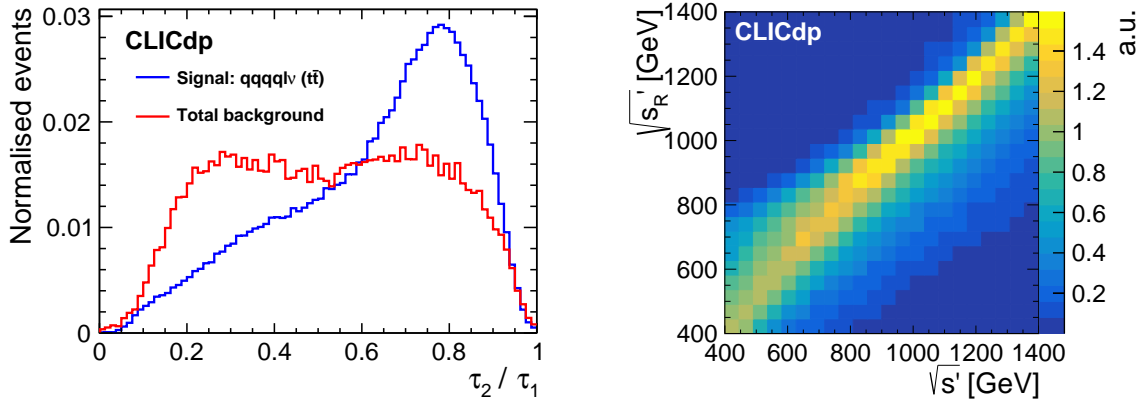


Figure 17: The N-subjettiness ratio τ_2/τ_1 for the leptonically decaying large- R jet (left). Reconstructed centre-of-mass energy $\sqrt{s'_R}$ from kinematic fitting vs the generated collision energy, $\sqrt{s'}$, including the effects of the luminosity spectrum and ISR (right). To illustrate the correlation down to lower $\sqrt{s'}$, the $\sqrt{s'}$ distribution is reweighted so that each column contains the same number of entries, leading to a flat distribution in $\sqrt{s'}$.

7.2 Radiative events at 1.4 TeV

This section describes an analysis using radiative events to extract $\sigma_{t\bar{t}}$ and A_{FB} in regions of $\sqrt{s'}$ below the nominal collision energy of $\sqrt{s} = 1.4$ TeV. The A_{FB} is evaluated across three mutually exclusive intervals in $\sqrt{s'}$: 0.40–0.90 TeV, 0.90–1.2 TeV and ≥ 1.2 TeV.

This analysis uses jet-shape variables such as N-subjettiness [120] as input to a multivariate classifier. These variables are well suited for the identification of boosted objects with multi-body kinematics and discriminate effectively against QCD background jets.

The first stage of the event reconstruction is the identification of isolated charged leptons. In this analysis we apply a jet-based procedure where initially all PFOs are clustered into five jets using the Durham algorithm [78]. In the next step all PFOs identified as a charged lepton by the PANDORAPFA algorithm are considered as a candidate. The energy ratio between each such candidate and the corresponding jet it was clustered into is evaluated and the candidate with the highest energy ratio is selected as the isolated lepton. For events without explicit input candidates from PANDORAPFA, 2% (1%) of events with a final state electron (muon), the PFO with the highest energy ratio is chosen to ensure high efficiency. This method yields a charge tagging efficiency of 93% (96%) for electrons (muons).

The remaining PFOs are clustered into two exclusive large- R jets using the VLC algorithm with a jet radius of 1.5 ($\beta, \gamma = 1$). The large- R jets are associated with either the hadronically decaying top quark or the b-quark from the leptonically decaying top quark. After evaluating the association based on invariant mass, energy, b-quark tagging, and separation of jets from the isolated lepton, associating the jet with the highest energy with the hadronically decaying top quark is found to give the best performance for reconstructing the correct top-quark decay angle.

The sub-structure of each large- R jet is characterised by the N-subjettiness [120], the jet-multiplicity and the splitting scales. N-subjettiness, τ_N , is defined as

$$\tau_N = \frac{1}{d_0} \sum_k p_{T,k} \min\{\Delta R_{1,k}, \Delta R_{2,k}, \dots, \Delta R_{N,k}\},$$

where k runs over the constituent particles of the jet, each with transverse momentum $p_{T,k}$. The distance in the pseudorapidity-azimuth plane, between each candidate subjet J and constituent particle k , is denoted $\Delta R_{J,k} = \sqrt{\Delta\eta^2 + \Delta\phi^2}$ and $d_0 = R_0 \cdot \sum_k p_{T,k}$, where R_0 is the jet radius used in the large- R jet clustering. τ_N quantifies to what degree a jet can be regarded as composed of N subjets. A large value would indicate that the jets have a large fraction of their energy distributed away from the candidate subjet directions, i.e. that it has at least $N + 1$ subjets. A key step for defining N-subjettiness is to make an appropriate choice of the candidate subjets. In this analysis they are produced by reclustering the large- R jets into J exclusive jets (k_t algorithm, $R = 0.3$). The analysis studied several ratios τ_{N+1}/τ_N for both the hadronically and leptonically decaying top quark. The N-subjettiness ratio τ_2/τ_1 for the leptonically decaying large- R jet is shown to the left of Figure 17. This variable is used to distinguish the b-quark of the leptonic top-quark decay from jets with a multi-pronged sub-structure as present in some of the background processes considered. The distributions are shown after both pre-selection and quality cuts and are normalised to unity.

The jet-multiplicity is calculated by reclustering each large- R jet (k_t algorithm, $R = 0.05$) and counting the number of inclusive so-called micro-jets present. The splitting scales of each jet are characterised by the jet-resolution parameters y_{12} , y_{23} , and y_{34} , as well as the relative angles between each subjet, and are produced by reclustering the large- R jet into three exclusive jets (k_t algorithm, $R = 0.3$). For the latter we expect a small separation due to fake splittings of single-quark jets while genuinely distinctive sub-structures would yield larger separations.

Kinematic fitting, as implemented in MarlinKinFit [121], is used to reconstruct the $\sqrt{s'}$ of each collision, allowing for ISR and beamstrahlung. The fit has four degrees of freedom (the 3-momentum of the neutrino and the z component of the photon momentum) and six constraints (the total 4-momentum of the system, the mass of the leptonically decaying W boson, and the masses of the two top-quark candidates). It is assumed that any unobserved ISR and beamstrahlung contributions have negligible transverse momentum. This method yields a resolution of ~ 75 GeV on $\sqrt{s'}$. A cut is placed on the resulting reconstructed $\sqrt{s'_R}$, as part of the pre-selection. The cut value corresponds to the definition of the kinematic region for each signal interval considered. The reconstruction performance is illustrated to the right of Figure 17. The figure shows the correlation between the reconstructed and generated values on an event-by-event basis, down to the lowest collision energies. All subsequent references to jet kinematic properties in this section refer to those of the fitted objects.

The full event selection is performed in three stages: a pre-selection to suppress apparent backgrounds, a cut on reconstruction quality, and finally a multivariate classification algorithm. The selection is based on PFOs with `tight` timing cuts.^{xiv}

^{xiv}This choice is motivated by the study of jet substructure variables that have lower contamination from beam jets.

The pre-selection consists of the following requirements:

- scalar sum of transverse momenta $> 200 \text{ GeV}$,
- energy of the hadronically decaying top quark $> 100 \text{ GeV}$,
- transverse momentum of b-quark jet $> 20 \text{ GeV}$,
- and jet splitting scales $-\log_{10}(y_{23}) < 7$ and $-\log_{10}(y_{34}) < 9$.

These cuts are followed by a series of quality cuts aimed at removing events in which the polar angle of the hadronically decaying top quark is poorly reconstructed, for example due to proximity to the edge of the detector acceptance. The cuts used are:

- invariant mass and transverse momentum of the hadronically decaying top quark $> 100 \text{ GeV}$,
- invariant mass of the leptonically decaying top quark $< 100 \text{ GeV}$,
- angle θ_{12} between the leading and next-to-leading energy subjects of the hadronically decaying top quark $0.2 < \cos \theta_{12} < 0.9$,
- jet splitting scale $-\log_{10}(y_{23}) > 3$,
- z component of the total event momentum from the kinematic fitter $< 100 \text{ GeV}$ (used as a quality cut for the kinematic fitter routine).

The final stage of the event selection was performed by training two BDTs to search for $t\bar{t}$ events, one with a centre-of-mass energy $\sqrt{s'}$ above 1.2 TeV and one with a centre-of-mass energy $\sqrt{s'}$ below or equal to 1.2 TeV . Each BDT uses 21 variables based on the kinematics of the hadronically decaying top quark, lepton and b-jet, the substructure of both large- R jets, the number of lepton candidates with energy $> 30 \text{ GeV}$, b-quark tagging information, and event shapes.

The event selection efficiencies for the signal and dominant background processes are shown in [Table 16](#), [Table 17](#), and [Table 18](#) in the Appendix, along with the total number of selected events. Contributions from additional backgrounds such as $e^+e^- \rightarrow qq\nu\nu$ and additional six-fermion processes are found to be negligibly small. Note that most events with a large energy loss due to photon radiation also have a large net boost along the z -direction which makes them more difficult to reconstruct. In particular, this results in a significantly lower overall efficiency for the selection in the interval $0.40 \leq \sqrt{s'} \leq 0.90 \text{ TeV}$.

The polar-angle distributions of the hadronically decaying top-quark candidates are shown in [Figure 18](#). The dashed black curve shows the reconstructed distribution for the total MC, while the grey area indicates the level of background only. These include the effects of detector modelling, event reconstruction, and candidate selection. The blue data points represent one pseudo-experiment performed for the given luminosity, after subtraction of background and correction for finite selection efficiencies as described in [Section 7](#). The blue dotted line shows the fit performed to the pseudo-experiment data and is used to extract $\sigma_{t\bar{t}}$ and A_{FB} . The red solid line displays the simulated distribution at parton-level (WHIZARD). The distributions are shown for the fiducial region $-0.9 \leq \cos \theta^* \leq 0.9$.

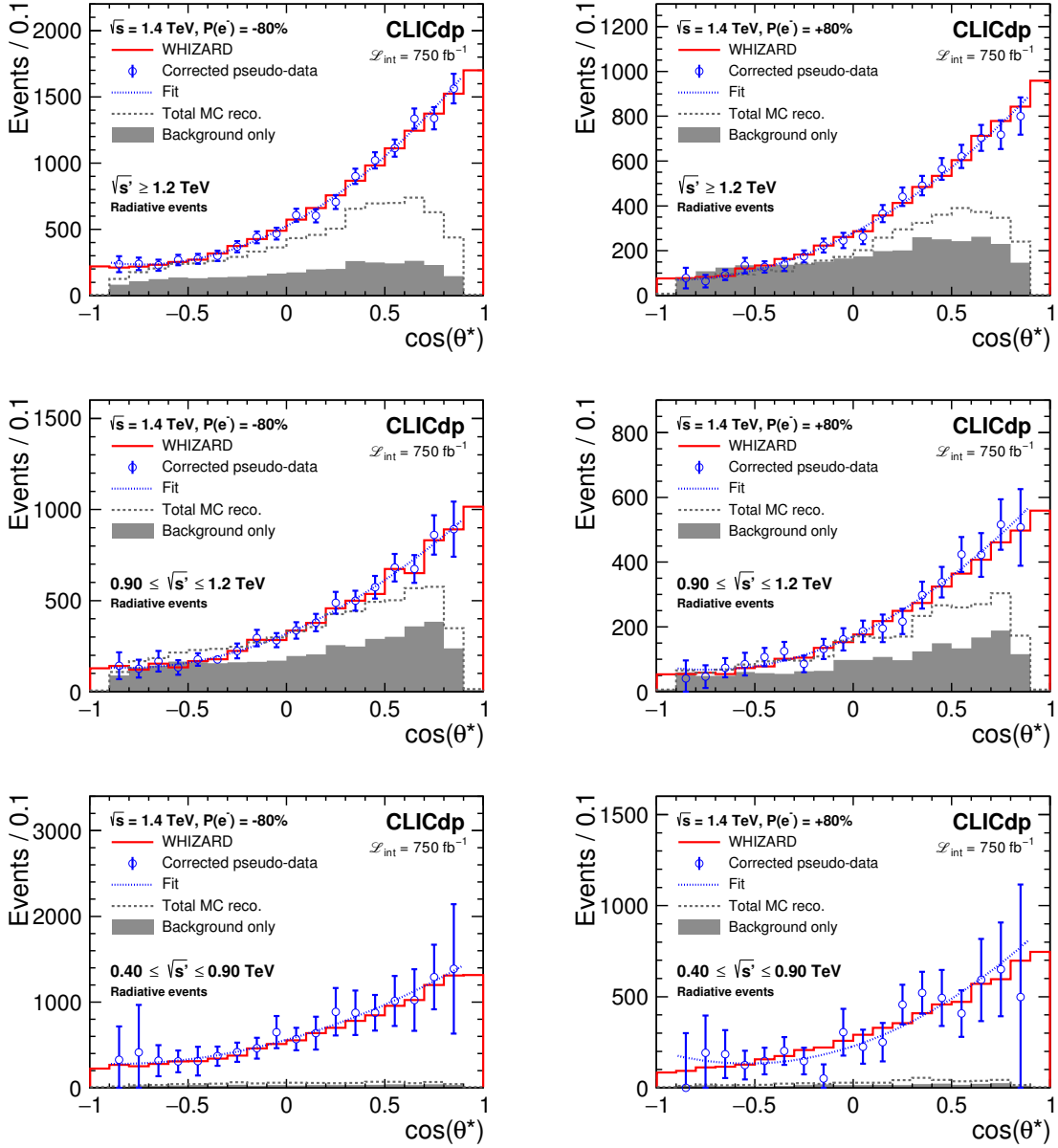


Figure 18: The top-quark polar angle distributions for the analysis of radiative semi-leptonic $t\bar{t}$ events at $\sqrt{s} = 1.4$ TeV, for $P(e^-) = -80\%$ (left column) and $P(e^-) = +80\%$ (right column), and an integrated luminosity of 750 fb^{-1} . Distributions are shown for the three signal regions in $\sqrt{s'}$. The dashed black curve shows the reconstructed total MC distribution, while the grey area indicates the level of background only. The blue data points and dotted line represent one pseudo-experiment after subtraction of background and correction for finite selection efficiencies, and the corresponding fit, respectively. The red solid line represents the simulated parton-level distribution.

7.3 Boosted event topologies

For operation above ~ 1 TeV a large fraction of the top quarks will be produced with significant boosts. In particular, the event topology is very different from that of the analysis described in [Section 7.1](#), where the top quarks are produced close to the threshold with a resulting isotropic event topology. [Figure 19](#) shows a boosted semi-leptonic $t\bar{t}$ event at 3 TeV with clear separation between the decay products of the top- and anti-top quark respectively. Owing to the boost, the top-quark candidates are more easily distinguishable from each other and the relative effect of migrations, as discussed in [Section 7.1](#), is therefore expected to be smaller. This section describes the event selection and results for an analysis targeting semi-leptonic $t\bar{t}$ events ($l = e, \mu$) at the collision energies of 1.4 TeV and 3 TeV. The signal events are restricted to the kinematic region defined as $\sqrt{s'} \geq 1.2$ TeV and $\sqrt{s'} \geq 2.6$ TeV, respectively. A corresponding cut is applied to the reconstructed collision energy, $\sqrt{s'_R}$, as part of the pre-selection defined below.

The event selection proceeds through the identification of one isolated charged lepton in association with one boosted top quark, the latter being identified using a dedicated top-quark tagger algorithm whose details and performance are described in [Section 5](#). The selection is based on PFOs with selected timing cuts at 1.4 TeV and `tight` timing cuts at 3 TeV.

The isolated charged lepton in the event is identified using the isolated lepton finding procedure described in [Section 4.3](#). In addition we require that the p_T of the isolated lepton candidate is larger than 10 GeV. In cases where several candidates exist, the candidate with the highest p_T is selected. The resulting isolated lepton efficiency is about 90% (80%) for final states with a muon (electron) out of which 99% (98%) are identified with the correct charge.

The remaining PFOs are clustered in two subsequent steps following the approach outlined in [\[122\]](#). Here, a pre-clustering is done in an inclusive mode using the Generalised- k_t algorithm (with beam jets) for e^+e^- collisions (“gen- k_t algorithm”) [\[78\]](#) with a radius $R = 0.4$ and a minimum p_T thresh-

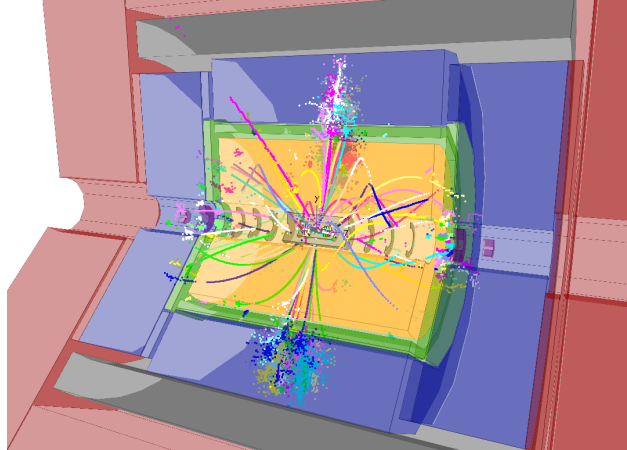


Figure 19: An illustration of a highly boosted $t\bar{t} \rightarrow q\bar{q}q\bar{q}\nu_\mu$ event in CLIC_ILD with an effective collision energy $\sqrt{s'} = 3$ TeV. The event includes overlay of $\gamma\gamma \rightarrow \text{hadrons}$ background as described in [Section 4.2](#). An isolated lepton is clearly seen along with two large boosted jets.

P(e ⁻) Process	σ [fb]		ϵ_{Pre} [%]		ϵ_{MVA} [%]		N	
	-80%	+80%	-80%	+80%	-80%	+80%	-80%	+80%
e ⁺ e ⁻ ($\rightarrow t\bar{t}$) \rightarrow qqqqlv (l = e, μ) ^a	18.4	9.83	43	44	85	87	5,051	2,854
e ⁺ e ⁻ ($\rightarrow t\bar{t}$) \rightarrow qqqqlv (l = e, μ) ^b	28.5	14.9	2.5	2.7	68	56	357	167
e ⁺ e ⁻ ($\rightarrow t\bar{t}$) \rightarrow qqqqlv (l = τ)	23.2	12.3	4.7	4.8	63	57	517	250
e ⁺ e ⁻ ($\not\rightarrow t\bar{t}$) \rightarrow qqqqlv	72.2	16.5	6.0	7.2	35	59	1137	522
e ⁺ e ⁻ \rightarrow qqqqqq	116	44.9	2.3	2.4	9.2	9.5	187	77
e ⁺ e ⁻ \rightarrow qqllvv	44.1	15.3	1.2	1.5	27	40	107	68
e ⁺ e ⁻ \rightarrow qqqq	2,300	347	0.31	0.47	0.22	0.56	12	7
e ⁺ e ⁻ \rightarrow qqlv	6,980	1,640	0.02	0.01	0.00	0.00	-	-
e ⁺ e ⁻ \rightarrow qqll	2,680	2,530	0.01	0.08	0.00	0.00	-	-
e ⁺ e ⁻ \rightarrow qq	4,840	3,170	0.21	0.16	1.3	0.00	97	-

^aKinematic region defined as $\sqrt{s'} \geq 1.2$ TeV

^b $\sqrt{s'} < 1.2$ TeV

Table 8: Event selection summary for the analysis of $t\bar{t}$ events at $\sqrt{s} = 1.4$ TeV, assuming 750fb^{-1} for each polarisation state considered. The cross section quoted for the signal sample in the uppermost row is defined in the kinematic region $\sqrt{s'} \geq 1.2$ TeV. The fractional pre-selection and MVA selection efficiencies are shown in the subsequent columns along with the number of events in the final sample.

old of 5 GeV. The resulting PFOs are re-clustered into two exclusive jets using the VLC algorithm with a large radius $R = 1.4$ (1.0) for the sample at 1.4 (3) TeV. The use of a large radius is essential to fully capture the boosted top quarks as seen in Figure 6. The effect of this two-stage clustering is similar to that of grooming (and in particular trimming): the effective area of the jet is reduced and soft emission does not obscure the reconstruction of its substructure. The resulting jets are used as input to the top-quark tagger that constitutes the basis for the identification of the hadronically decaying top quark in this analysis.

The pre-selection consists of choosing events with one isolated lepton, one top-quark tagged jet, no isolated high-energy photons, and a reconstructed centre-of-mass energy, $\sqrt{s'_R}$, above 1.2 TeV. Isolated high-energy photons are defined as photons from the particle flow reconstruction with a p_T in excess of 75 GeV, a polar angle in the range $10^\circ \leq \theta \leq 170^\circ$, and low activity in a cone around the candidate PFO. To reconstruct the effective centre-of-mass $\sqrt{s'}$ we first assume that the missing transverse momentum, estimated by adding up the 4-vectors of the two large- R jets and the isolated charged lepton, can be used as an estimator for the neutrino transverse momentum components. Here we neglect the effect from unidentified ISR and beamstrahlung photons. The z -component of the neutrino momentum, $p_{\nu,z}$, is retrieved by solving

$$M_W^2 = m_l^2 + 2(E_l E_\nu - \vec{p}_l \cdot \vec{p}_\nu), \quad (7.3)$$

given a constraint on M_W , the mass of the leptonically decaying W boson. Here, the indices l and v

P(e ⁻) Process	σ [fb]		ϵ_{Pre} [%]		ϵ_{MVA} [%]		N	
	-80%	+80%	-80%	+80%	-80%	+80%	-80%	+80%
$e^+e^- (\rightarrow t\bar{t}) \rightarrow qqqlv$ ($l = e, \mu$) ^a	3.48	1.89	41	43	80	85	1,711	1,038
$e^+e^- (\rightarrow t\bar{t}) \rightarrow qqqlv$ ($l = e, \mu$) ^b	13.7	7.26	0.98	0.86	65	76	132	72
$e^+e^- (\rightarrow t\bar{t}) \rightarrow qqqlv$ ($l = \tau$)	8.45	4.51	3.6	3.8	58	47	262	121
$e^+e^- (\not\rightarrow t\bar{t}) \rightarrow qqqlv$	99.6	22.6	1.4	1.4	23	51	504	233
$e^+e^- \rightarrow qqqqq$	54.0	18.0	3.4	3.8	4.7	6.1	129	62
$e^+e^- \rightarrow qqllv$	59.7	14.9	0.28	0.37	23	40	58	33
$e^+e^- \rightarrow qqqq$	963	130	0.36	0.38	0.21	0.39	11	3
$e^+e^- \rightarrow qqlv$	8,810	2,310	0.01	0.01	0.00	0.00	-	-
$e^+e^- \rightarrow qqll$	3,230	3,060	0.02	0.02	0.44	0.00	5	-
$e^+e^- \rightarrow qq$	3,510	2,390	0.15	0.11	0.29	0.00	23	-

^aKinematic region defined as $\sqrt{s'} \geq 2.6$ TeV

^b $\sqrt{s'} < 2.6$ TeV

Table 9: Event selection summary for the analysis of $t\bar{t}$ events at $\sqrt{s} = 3$ TeV, assuming 1.5 ab^{-1} for each polarisation state considered. The cross section quoted for the signal sample in the uppermost row is defined in the kinematic region $\sqrt{s'} \geq 2.6$ TeV. The fractional pre-selection and MVA selection efficiencies are shown in the subsequent columns along with the number of events in the final sample.

denote the lepton and neutrino candidate quantities, respectively. Equation 7.3 is quadratic in $p_{v,z}$ and has no solution if the observed missing transverse energy fluctuates such that the invariant mass of the combined neutrino-lepton system is above M_W . In such cases the missing transverse energy is scaled to provide real solutions. The resulting neutrino-lepton system solutions are combined with each of the large- R jets and the final solution is chosen as the one that yields a mass closest to the generated top-quark mass. This method yields an RMS on $\sqrt{s'}$ of ~ 140 GeV. A cut is placed on the reconstructed quantity, $\sqrt{s'_R}$, corresponding to the kinematic regions of the signal.

The remaining events are analysed using multivariate classification algorithms based on BDTs. In light of the large variety of the different backgrounds considered, two initial MVAs are trained focussing on slightly different topologies. The first MVA is trained using backgrounds with two quarks and either 0, 1, or 2 leptons, while the second MVA focuses on fully-hadronic four-quark and six-quark jet topologies. The final MVA considers all relevant backgrounds and includes the score from the two initial MVAs. Each MVA is trained on the 20 most important variables and the parameters of the algorithm are tuned to reduce overtraining. In addition to the scores from the initial MVAs, the most important variables include those derived from the kinematics of both the hadronically and leptonically decaying top quark (including the detailed output from the top-tagger), event missing p_T , visible energy and event shape, lepton kinematics, flavour tagging information, jet splitting scales, and substructure variables such as N-subjettiness discussed in Section 7.2. Separate BDTs are applied for the 1.4 TeV and 3 TeV samples and for the two different polarisations

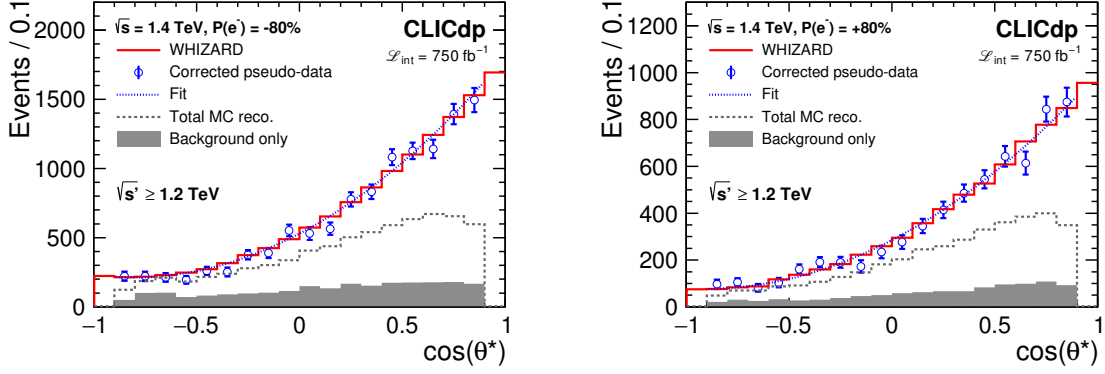


Figure 20: Top-quark polar angle distributions from the analysis of boosted semi-leptonic $t\bar{t}$ events, at a nominal collision energy of 1.4 TeV for $P(e^-) = -80\%$ (left) and $P(e^-) = +80\%$ (right), and an integrated luminosity of 750 fb^{-1} . The dashed black curve shows the reconstructed total MC distribution, while the grey area indicates the level of background only. The blue data points and dotted line represent one pseudo-experiment after subtraction of background and correction for finite selection efficiencies, and the corresponding fit, respectively. The red solid line represents the simulated parton-level distribution.

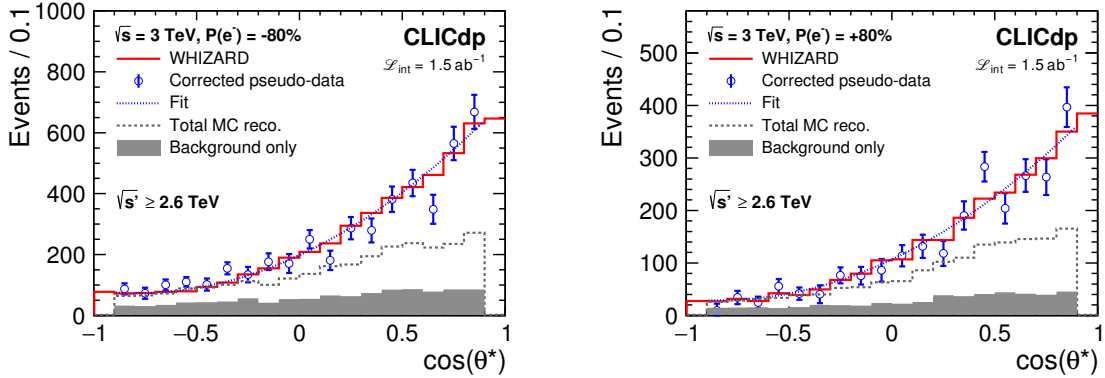


Figure 21: Top-quark polar angle distributions from the analysis of boosted semi-leptonic $t\bar{t}$ events, at a nominal collision energy of 3 TeV for $P(e^-) = -80\%$ (left) and $P(e^-) = +80\%$ (right), and an integrated luminosity of 1.5 ab^{-1} . See further details in [Figure 20](#).

considered. The cut applied on the classification score is chosen to minimise the statistical uncertainty on the two extracted observables A_{FB} and $\sigma_{t\bar{t}}$.

The fractional event selection efficiencies for the signal and dominant background processes along with the total number of events selected are shown in [Table 8](#) and [Table 9](#) for the samples at nominal collision energies of 1.4 and 3 TeV. Note that the cross sections quoted include the effect of ISR and the CLIC luminosity spectrum. The signal samples are further defined in the kinematic regions $\sqrt{s'} \geq 1.2\text{ TeV}$ and $\sqrt{s'} \geq 2.6\text{ TeV}$, respectively. Contributions from other backgrounds such as $e^+e^- \rightarrow qq\nu\nu$ and additional six-fermion processes are found to be negligibly small.

The polar-angle distributions of the hadronically decaying top-quark candidates are shown in [Figure 20](#) and [Figure 21](#). See [Section 7.2](#) for a full description of the different distributions shown.

7.4 Cross section and asymmetry measurements

[Equation 7.1](#) and [Equation 7.2](#) are used to extract $\sigma_{t\bar{t}}^{\text{xv}}$ and A_{FB} after background subtraction and correction for finite selection efficiencies. The fiducial region $-0.9 \leq \cos(\theta^*) \leq 0.9$ is used for the fit, motivated by the limited acceptance in the very forward region. For the analysis at $\sqrt{s} = 380$ GeV the overall shape of the polar-angle distribution is restored by the quality (D^2) cut and an overall constant factor is used to correct for the finite efficiency. For the analyses at higher centre-of-mass energy the limited acceptance of the event selection in the forward region significantly distorts the reconstructed polar-angle distributions as seen in for example [Figure 20](#). To compensate for the finite selection efficiencies, a correction is applied, estimated bin-by-bin using half of the available sample and applied to the other half, and vice versa.

The results from the analyses discussed in [Section 7](#) are summarised in [Table 10](#) and [Table 11](#). The tables show the reconstructed quantities $\sigma_{t\bar{t}}$ and A_{FB} . These agree well with the MC prediction for the SM. Note that $\sigma_{t\bar{t}}$ is significantly higher for left-handed than for right-handed electrons as expected from the underlying chiral structure of the electroweak interaction. Results at 1.4 TeV,

^{xv}Note that the extracted cross sections represent a convolution of $\sigma_{t\bar{t}}$ with the luminosity spectrum in a range of effective collision energies.

\sqrt{s}	380 GeV ^a		1.4 TeV ^b		3 TeV ^b	
$P(e^-)$	-80%	+80%	-80%	+80%	-80%	+80%
$\sigma_{t\bar{t}}^c$ [fb]	161.00	75.97	18.44	9.84	3.52	1.91
stat. unc. [fb]	1.09	0.73	0.34	0.23	0.12	0.08
A_{FB}	0.1761	0.2065	0.567	0.620	0.596	0.645
stat. unc.	0.0094	0.0084	0.014	0.016	0.022	0.028

Table 10: Results from the analysis of semi-leptonically decaying top quarks at the three stages of CLIC with an integrated luminosity of 250 fb^{-1} , 750 fb^{-1} , and 1500 fb^{-1} for each polarisation state, respectively. The values are obtained from full simulation studies using the CLIC_ILD detector concept. Note that the cross section, $\sigma_{t\bar{t}}$, and A_{FB} are defined in the kinematic region of $\sqrt{s'} \geq 1.2(2.6) \text{ TeV}$ for operation at $\sqrt{s} = 1.4 \text{ TeV}$ (3 TeV). For operation at $\sqrt{s} = 380 \text{ GeV}$ the A_{FB} for $P(e^-) = -80\%$ is extracted using the event sample defined by $D^2 < 1$; the other results at $\sqrt{s} = 380 \text{ GeV}$ are obtained using the sample with a looser selection cut, $D^2 < 15$.

^aResults from [Section 7.1](#)

^bResults from [Section 7.3](#)

^cConvolution of $\sigma_{t\bar{t}}$ with the CLIC luminosity spectrum in the kinematic region studied.

$P(e^-)$	$\sqrt{s'} \in [400, 900) \text{ TeV}$		$\sqrt{s'} \in [900, 1200) \text{ TeV}$		$\sqrt{s'} \geq 1200 \text{ GeV}$	
	-80%	+80%	-80%	+80%	-80%	+80%
$\sigma_{t\bar{t}}^a \text{ [fb]}$	16.56	8.63	11.01	5.87	18.41	9.84
stat. unc. [fb]	1.31	0.83	0.38	0.29	0.37	0.28
A_{FB}	0.458	0.514	0.546	0.588	0.562	0.621
stat. unc.	0.081	0.105	0.034	0.045	0.018	0.024

Table 11: Results for radiative events at $\sqrt{s} = 1.4 \text{ TeV}$ with an integrated luminosity of 750 fb^{-1} for each polarisation state. Values are shown from three intervals of $\sqrt{s'}$ below the nominal collision energy.

^aConvolution of $\sigma_{t\bar{t}}$ with the CLIC luminosity spectrum in the kinematic region studied.

for the region $\sqrt{s'} \geq 1.2 \text{ TeV}$, were computed for each of the two analyses presented in [Section 7.2](#) and [Section 7.3](#), respectively. These show good agreement taking into account the different event selection efficiencies, and serve as a useful cross-check.

The results presented in this section are the first studies of $t\bar{t}$ production in full simulation for a multi-TeV e^+e^- collider. Further improvements can be made by for example including fully-hadronic final states, or semi-leptonic tau events where the tau decays leptonically. However, for the former, the jet charge reconstruction, needed for the reconstruction of observables such as the A_{FB} , is challenging and needs to be studied in more detail. The BSM reach of these results is illustrated in [Section 10](#) where the sensitivity of top-philic operators is presented.

7.5 Systematic uncertainties

The expected uncertainties given in [Table 10](#) and [Table 11](#) are purely statistical and do not include potential sources of systematic uncertainty. The results presented illustrate the level of precision desirable for the control of systematic effects. Although a full investigation of systematic uncertainties is beyond the scope of this paper, the impacts of some ad-hoc variations are discussed for the analysis of radiative events at $\sqrt{s} = 1.4 \text{ TeV}$, presented in [Section 7.2](#). This analysis is used as an example because the statistical uncertainties are generally lower at $\sqrt{s} = 1.4 \text{ TeV}$ than at $\sqrt{s} = 3 \text{ TeV}$. Further, events with significant energy loss due to ISR and beamstrahlung, as studied in this analysis, are potentially more likely to be sensitive to systematic uncertainties as background rejection is more challenging. In this sense, systematic effects estimated for the radiative event analysis can be considered as conservative estimates for the other analyses. In each case studied, the effects on $\sigma_{t\bar{t}}$ and A_{FB} are considered.

- The normalisation of the background is varied by $\pm 5\%$. We consider only the dominant background processes: $qqq\bar{q}lv$ (non- $t\bar{t}$), $q\bar{q}lv$, and qq . This leads to an effect on the cross section of around 1–3%, and around 0.4–1.2% for A_{FB} ;

- The background shape modelling is studied by applying a linear gradient of $\pm 2\%$ to the shape of the total background in $\cos(\theta^*)$. This leads to an uncertainty of about 0.2–0.8% on $\sigma_{t\bar{t}}$ and 0.9–2.9% on A_{FB} ;
- To check for a possible bias in the event selection towards the generated A_{FB} , the MC datasets are reweighted to different values of A_{FB} according to [Equation 7.1](#) and [Equation 7.2](#). The relation between the reconstructed and generated values of A_{FB} is found to be linear and hence such an effect could be corrected for.

The analysis is found to be insensitive to the choice of fit range or MVA score cut value. In addition, it is expected that the integrated luminosity will be known with an accuracy of a few per mille using the luminometer envisaged for CLIC [94, 95], and therefore does not represent a significant systematic uncertainty for this analysis. In summary, the estimates presented above indicate that this analysis is not limited by systematic effects.

8 Associated $t\bar{t}$ production processes at high energy

At the higher CLIC energy stages, top-quark pairs can be produced in additional processes beyond $e^+e^- \rightarrow t\bar{t}$. The top Yukawa coupling can be directly obtained from the $e^+e^- \rightarrow t\bar{t}H$ cross section. This process also allows a study of the CP properties of the Higgs boson in the $t\bar{t}H$ coupling. The second CLIC stage at $\sqrt{s} = 1.5 \text{ TeV}$ is well suited for making these measurements. At $\sqrt{s} = 3 \text{ TeV}$ the production of top-quark pairs in the VBF process $e^+e^- \rightarrow t\bar{t}\nu_e\bar{\nu}_e$ can also be studied.

8.1 Study of $t\bar{t}H$ production

Results from a first study of $t\bar{t}H$ production at CLIC and projections for the precision on the top Yukawa coupling were presented in [6, 123, 124]. In the following, a refined version of this analysis is described. An improved version of the flavour tagging is used. The estimated precision on the top Yukawa coupling is based on NLO QCD calculations [34], whereas the previous analysis used LO predictions. The sensitivity to CP mixing in the $t\bar{t}H$ coupling is presented.

8.1.1 Cross section measurement and top Yukawa coupling

The $e^+e^- \rightarrow t\bar{t}H$ process has been studied for the CLIC_SiD detector concept using $H \rightarrow b\bar{b}$ decays at $\sqrt{s} = 1.4 \text{ TeV}$. The analysis focuses on fully-hadronic and semi-leptonic top-quark pair decays, which lead to final states with eight or six jets, respectively, including four b-quark jets.

The two channels are differentiated by the presence of an isolated electron, muon or tau lepton. If zero leptons are found, the event is classified as fully-hadronic. If one lepton is found, the event is classified as semi-leptonic. Events where more than one lepton is found are not considered further. The longitudinally-invariant k_t algorithm with $R = 1.0$ is used to cluster the particles of each event into a specific number of jets. Events classified as fully-hadronic are clustered into eight jets. In semi-leptonic events, the lepton candidate is removed and the remaining particles are clustered into six jets. The jets are then combined to form the W boson, top-quark, and Higgs boson candidates.

For example, in the case of the semi-leptonic channel, the jet assignment with the minimum value of

$$\chi^2 = \frac{(m_{ij} - m_W)^2}{\sigma_W^2} + \frac{(m_{ijk} - m_t)^2}{\sigma_t^2} + \frac{(m_{lm} - m_H)^2}{\sigma_H^2}, \quad (8.1)$$

gives the W boson, top-quark, and Higgs boson candidates, where m_{ij} is the invariant mass of the jet pair used to reconstruct the W candidate, m_{ijk} is the invariant mass of the three jets used to reconstruct the hadronically decaying top-quark candidate and m_{lm} is the invariant mass of the jet pair used to reconstruct the Higgs boson candidate. The expected invariant mass resolutions $\sigma_{W,t,H}$ were estimated from combinations of two or three reconstructed jets matched to the W boson, top-quark, and Higgs boson decay products at hadron level. A similar construction is used for the fully-hadronic channel with additional terms corresponding to the second hadronically decaying top quark.

Multivariate BDT classifiers are used in the final step of the analysis to separate signal and background events. These are constructed individually for the semi-leptonic and fully-hadronic event candidates. The classifiers were trained using variables related to flavour tagging and event kinematics, as well as variables derived following the pairing in Equation 8.1: the reconstructed Higgs mass, the χ^2 , and angular separations between the event constituents. For the semi-leptonic channel we also include lepton variables, while the fully-hadronic channel considers additional jet variables. Cuts on the BDT classifier outputs are chosen to maximise the signal significances, estimated as $S/\sqrt{S+B}$, where $S(B)$ represent the signal (background) sample.

The expected numbers of selected events for 1.5 ab^{-1} at $\sqrt{s} = 1.4 \text{ TeV}$ are listed in Table 12. The $t\bar{t}H$ cross section can be measured with a precision of 11.1 % in the semi-leptonic channel and 9.6 % in the hadronic channel. The combined precision of the two channels is 7.3 %. Note that all $t\bar{t}H$ processes are considered as signal in the final calculations.

The benchmark analyses described here use LO Monte Carlo samples. The K-factor defined as the ratio of the NLO to the LO cross section is 0.938 [125] including the effects of ISR and beamstrahlung. Scaling the projected precision to the NLO cross section leads to an uncertainty of 7.5 %.

When extracting the top Yukawa coupling value from the $t\bar{t}H$ cross section, a small contribution from the Higgsstrahlung diagram, where the Higgs boson is radiated off the intermediate Z boson, has to be taken into account [126]. The factor to translate the uncertainty of the $t\bar{t}H$ production cross section into an uncertainty on the top Yukawa coupling was calculated including NLO QCD corrections, ISR and beamstrahlung [125]:

$$\frac{\Delta y_t}{y_t} = 0.503 \frac{\Delta \sigma}{\sigma}.$$

Thus, the expected precision on the top Yukawa coupling is $\Delta y_t/y_t = 3.8\%$, for 1.5 ab^{-1} of data at $\sqrt{s} = 1.4 \text{ TeV}$ without beam polarisation.

It was recently demonstrated that an even better statistical precision on y_t can be achieved indirectly using loop contributions to decays such as $H \rightarrow gg$ [127]. However, this approach implies

Process	N	Selected as	
		fully-hadronic	semi-leptonic
$e^+e^- \rightarrow t\bar{t}H, 6 \text{ jet}, H \rightarrow b\bar{b}$	647	367	38
$e^+e^- \rightarrow t\bar{t}H, 4 \text{ jet}, H \rightarrow b\bar{b}$	623	1	270
$e^+e^- \rightarrow t\bar{t}H, 2 \text{ jet}, H \rightarrow b\bar{b}$	150	2	22
$e^+e^- \rightarrow t\bar{t}H, 6 \text{ jet}, H \not\rightarrow b\bar{b}$	473	54	11
$e^+e^- \rightarrow t\bar{t}H, 4 \text{ jet}, H \not\rightarrow b\bar{b}$	455	8	22
$e^+e^- \rightarrow t\bar{t}H, 2 \text{ jet}, H \not\rightarrow b\bar{b}$	110	0	1
$e^+e^- \rightarrow t\bar{t}b\bar{b}, 6 \text{ jet}$	824	326	26
$e^+e^- \rightarrow t\bar{t}b\bar{b}, 4 \text{ jet}$	794	57	226
$e^+e^- \rightarrow t\bar{t}b\bar{b}, 2 \text{ jet}$	191	2	18
$e^+e^- \rightarrow t\bar{t}Z, 6 \text{ jet}$	2,843	345	34
$e^+e^- \rightarrow t\bar{t}Z, 4 \text{ jet}$	2,738	59	217
$e^+e^- \rightarrow t\bar{t}Z, 2 \text{ jet}$	659	1	16
$e^+e^- \rightarrow t\bar{t}$	203,700	498	742

Table 12: Expected numbers of signal and background events in the fully-hadronic and semi-leptonic channels for 1.5 ab^{-1} at $\sqrt{s} = 1.4 \text{ TeV}$. The columns show the total numbers of events before selection and the numbers of events passing the fully-hadronic and semi-leptonic BDT selections. No preselection is applied in the analysis.

additional model dependence compared to the direct extraction described here.

8.1.2 CP mixing in the $t\bar{t}H$ coupling

The measurement of the $t\bar{t}H$ cross section can be used to search for a CP-odd contribution to the $t\bar{t}H$ coupling. CP mixing in the $t\bar{t}H$ coupling can be parameterised as

$$-ig_{t\bar{t}H}(\cos\phi + i\sin\phi\gamma_5),$$

where ϕ denotes the mixing angle ($\phi = 0$ for the SM case). Note that $\cos^2\phi + \sin^2\phi = 1$ is assumed. The SM is given by $\sin^2\phi = 0$ while $\sin^2\phi = 1$ corresponds to a pure CP-odd coupling. The dependence of the $t\bar{t}H$ production cross section as a function of $\sin^2\phi$ is shown in Figure 22 [67]. The cross section decreases linearly with increasing $\sin^2\phi$. Similarly to the approach used for the extraction of the top Yukawa coupling discussed above, the uncertainty on the cross section can be translated into an uncertainty on $\sin^2\phi$.

Signal event samples were generated assuming different values of $\sin^2\phi$ for the semi-leptonic and fully-hadronic final states. The semi-leptonic analysis described in Section 8.1.1 was repeated for each $\sin^2\phi$ value, while for the fully-hadronic analysis the cross section uncertainty for the SM assumption was extrapolated.

The expected precision as a function of $\sin^2\phi$ is shown in Figure 22. Although the cross section decreases by about a factor 3.5 for a pure CP-odd coupling compared with the SM, the sensitivity

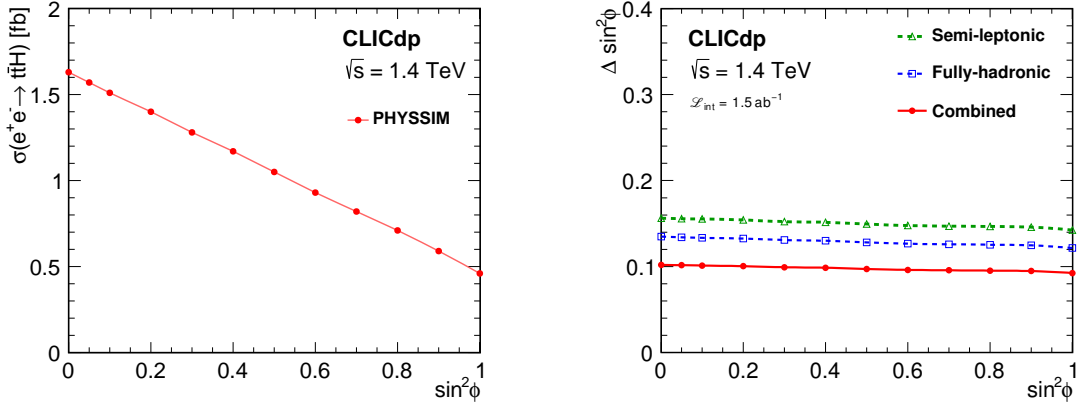


Figure 22: Cross section for the process $e^+e^- \rightarrow t\bar{t}H$ at $\sqrt{s} = 1.4$ TeV including the effects of initial-state radiation and beamstrahlung as a function of $\sin^2\phi$ (left). Sensitivity to the CP mixing angle $\sin^2\phi$ as a function of $\sin^2\phi$ from the $t\bar{t}H$ cross section at $\sqrt{s} = 1.4$ TeV assuming an integrated luminosity of 1.5 ab^{-1} (right). The sensitivities for both considered final states are shown separately in addition to the combined projection.

of $\Delta \sin^2\phi \approx 0.1$ for an integrated luminosity of 1.5 ab^{-1} at $\sqrt{s} = 1.4$ TeV is almost independent of $\sin^2\phi$. This precision can be improved further using additional information provided by beam polarisation and differential distributions [128].

8.2 Vector boson fusion production

The high-energy stages of CLIC allow the study of top-quark pair production initiated by low-virtuality (nearly on-shell) and highly energetic vector bosons, in the so-called vector boson fusion topology; see for example Figure 4e. This production mode is particularly interesting because it gives direct access to on-shell $W^+W^-t\bar{t}$ production, which might reveal large BSM effects. A particularly important role in this context is played by VBF production initiated by longitudinally polarised vector bosons, which are effectively equivalent to the Higgs field at high energy, owing to the Equivalence Theorem. In several new physics scenarios aimed at addressing the Naturalness problem, the Higgs boson and the top-quark interactions are largely modified, hence it is natural to study processes that are directly sensitive to such interactions. A specific example is the enhancement of “Higgs current” type operators (namely $Q_{\phi t}$, $Q_{\phi q}^{(1)}$, $Q_{\phi q}^{(3)}$, in Table 3) in the top-quark compositeness scenario [107] presented further in Section 10.

In this section we present a parton-level study of the CLIC sensitivity to EFT operators in VBF top-quark pair production focusing on the $W^+W^- \rightarrow t\bar{t}$ process and the four operators $Q_{\phi t}$, $Q_{\phi q}^{(1)}$, $Q_{\phi q}^{(3)}$ and Q_{tW} . The reason for this choice is that these operators are the only ones, out of the nine in Table 3, that give contributions to $W^+W^- \rightarrow t\bar{t}$ with an effect that grows quadratically with energy. Consequently these are the ones that are best probed by this channel.

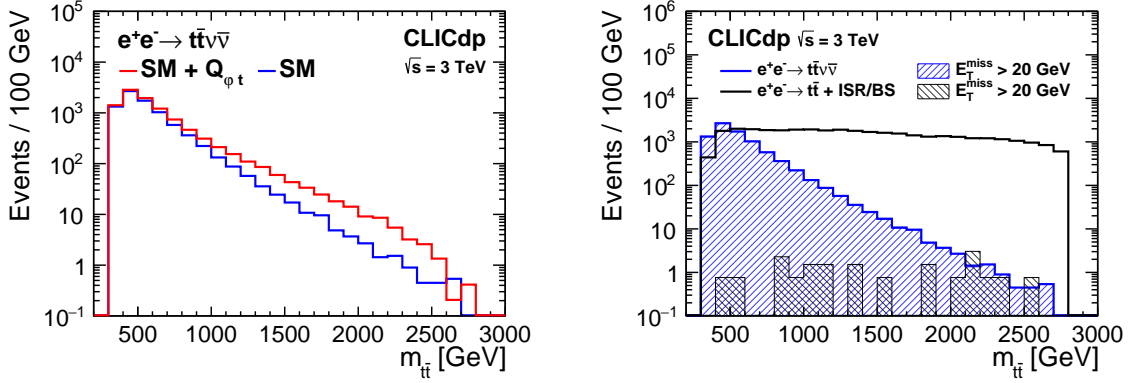


Figure 23: Top-quark pair invariant mass distributions for CLIC at $\sqrt{s} = 3$ TeV with 3 ab^{-1} . $e^+e^- \rightarrow t\bar{t}v\bar{\nu}$ (VBF) after a cut on the total invariant mass, illustrating the effect of including one example EFT operator, $Q_{\phi t}$, that grows with energy (left). VBF signal distribution and the $e^+e^- \rightarrow t\bar{t}$ SM background process before and after a cut on the total missing transverse energy, $E_T^{\text{miss}} > 20$ GeV (right). Note that $e^+e^- \rightarrow t\bar{t}$ includes both initial state radiation (ISR) and beamstrahlung (BS) effects.

The process $e^+e^- \rightarrow t\bar{t}v\bar{\nu}$ was simulated at tree-level using MADGRAPH [36] and the EFT UFO model [129]. WHIZARD [61] was used for the $e^+e^- \rightarrow t\bar{t}$ process in order to include the effects from beamsstrahlung and ISR.

The starting point for the analysis is to isolate the VBF topology in the complete $2 \rightarrow 4$ process $e^+e^- \rightarrow t\bar{t}v\bar{\nu}$. This is achieved by reconstructing the total invariant mass of the neutrinos from the final state top quarks and the initial state momenta, and imposing $M_{v\bar{v}} > 200$ GeV. The main role of this cut is to suppress $t\bar{t}Z$ production with the Z decaying to neutrinos, which constitutes a significant fraction of the total $t\bar{t}v\bar{\nu}$ cross section. Figure 23 shows the $t\bar{t}$ invariant mass distribution at $\sqrt{s} = 3$ TeV for an integrated luminosity of 3 ab^{-1} . The left plot shows the effect of the cut on the total invariant mass for the SM case and for a BSM scenario including one example EFT operator, $Q_{\phi t}$ ($C_{\phi t} = -0.83 \text{ TeV}^{-2}$), that grows with energy. Acceptance cuts $p_T > 20$ GeV and $|\eta| < 1.32$ are applied to the top-quark candidates. While a perfect top-quark reconstruction efficiency is assumed in this fiducial region for the figure, a 70% efficiency, compatible with the results of Section 5, is included in the fit. A potentially significant background originates from $e^+e^- \rightarrow t\bar{t}$, if the nominal 3 TeV collision energy is strongly reduced by initial state radiation or by beamstrahlung effects. However, a loose requirement on the total missing transverse energy, $E_T^{\text{miss}} > 20$ GeV, is sufficient to reduce this background to a negligible level, as shown to the right of Figure 23. At the same time, the cut has a negligible effect on the VBF signal.

The sensitivity to the EFT operators is estimated by performing a doubly-differential binned likelihood fit to the $t\bar{t}$ invariant mass and to the cosine of the $t\bar{t}$ scattering angle in the centre-of-mass frame. The latter variable improves the sensitivity because the contribution of the EFT operators has a different angular dependence than that of the SM. Uncorrelated 3% systematic relative uncertainties are assumed, and summed in quadrature with the statistical error. The 1σ sensitivity

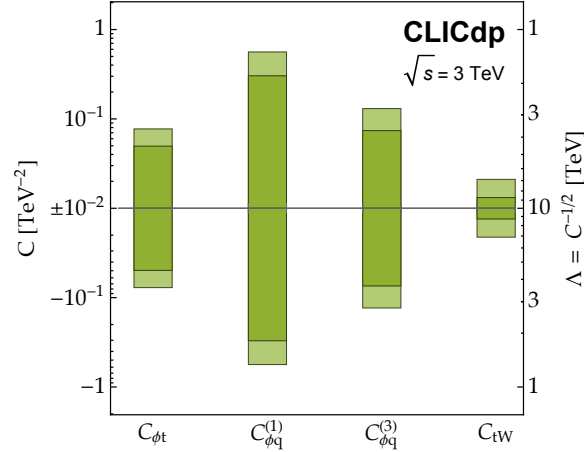


Figure 24: Single-operator sensitivity (68%) from vector boson fusion top-quark pair production at the 3 TeV CLIC. Both upper and lower limits are reported simultaneously on each side of the horizontal line. The stronger limits (dark green) assume perfect top-quark reconstruction and no systematic uncertainties; the weaker ones (light green) are derived with 50% $t\bar{t}$ reconstruction efficiency and 3% systematics.

to the four EFT operator coefficients is displayed in [Figure 24](#). Note that the ones reported in the figure are single-operator sensitivities, obtained by including only one operator at a time. The result should thus be interpreted with care, bearing in mind that cancellations are possible for certain combinations of operators, resulting in insensitive flat directions of the 4-dimensional operator space.

In conclusion, the result of this simplified analysis is that VBF top-quark pair production is a promising EFT probe that merits further study. A more detailed investigation, based on more realistic simulations and aimed at a more in-depth assessment of the impact of this channel in the CLIC EFT fit, is currently being performed and will be presented elsewhere.

9 Flavour-changing neutral current top-quark decays

The experimental sensitivity to rare top-quark decays is determined by the expected number of $t\bar{t}$ pairs produced, the efficiency of the rare decay reconstruction, and the effectiveness of the background suppression. As the cross section for top-quark pair production at higher-energy stages drops significantly (see [Figure 3](#)), we focus on the measurement of the FCNC top-quark decays at $\sqrt{s} = 380$ GeV.

We study FCNC couplings involving the charm quark, as many BSM models enhance these channels [53]. Channels involving the charm quark can be well reconstructed at CLIC thanks to good c-tagging capabilities, while they seem to be more difficult at the LHC. The cross section for single

top production in association with a photon measured at the HL-LHC can be translated to:

$$\text{BR}(t \rightarrow c\gamma) < 7.4 \cdot 10^{-5},$$

at 95% C.L. assuming 3 ab^{-1} collected at 14 TeV [130]. If the c-quark dominates $t \rightarrow qH$ decays, the following 95% C.L. limit is expected using top-quark pair production events at the HL-LHC [131]:

$$\text{BR}(t \rightarrow cH) < 2 \cdot 10^{-4}.$$

9.1 $t \rightarrow c\gamma$

The FCNC decay channel $t \rightarrow c\gamma$ is characterised by the presence of a high-energy photon, with an energy of at least 50 GeV. This gives a very clear signature, allowing for efficient separation of signal events from possible backgrounds. Top-quark pair production events for the signal sample were generated with WHIZARD 2.2.8 [61, 132] using a model with anomalous top-quark couplings (SM_top_anom). The vector coefficient of the tensor $tc\gamma$ coupling was tuned to obtain $\text{BR}(t \rightarrow c\gamma) = 10^{-3}$. This ensures that the contribution from the FCNC decay to the total top-quark width as well as the possibility of having two FCNC decays in the same event are negligible. Either the top or the anti-top quark (referred to as the “signal top quark” in the following) decays via the FCNC channel, and the other (denoted the “spectator top quark”) via the standard hadronic or leptonic decay. This analysis only considers the fully-hadronic decay channel where the spectator top quark decays into a b-quark and a W boson, the latter decaying hadronically into two light quarks. With the signal top quark decaying to a c-quark and a photon, the target events should contain a high-energy photon and a c-quark jet as well as one b-quark jet and two light jets from the W decay of the spectator top quark. The background sample considered consists of e^+e^- events compatible with top-quark pair production (6-fermion sample), four-fermion production events (dominated by W^+W^- contribution) and pair production of quarks other than the top quark.

The analysis uses a relatively loose event pre-selection based on the requirement of an isolated photon with at least 50 GeV of energy. This requirement reduces the background from standard $t\bar{t}$ decays by a factor of 20 while keeping 92% of the signal events. Contributions from four-fermion and quark-pair background events are reduced by factors of about 6 and 4, respectively. For the selected events, a reconstruction of the event kinematics is performed for a signal ($\gamma + 4$ jets) and a background (6 jet) hypothesis. Jets are reconstructed using the VLC algorithm in exclusive mode with a radius of 1.6 and $\beta = \gamma = 0.8$. For each hypothesis, all the possible jet combinations are considered, and the configuration that minimises a χ^2 value for the event is chosen. The χ^2 formula includes constraints on the invariant masses of the two reconstructed top-quark candidates and one (for signal hypothesis) or two (for background hypothesis) reconstructed W bosons. The discrimination of background events from signal events is based on a multivariate classifier analysis using a BDT approach with 42 input variables. The variables giving the largest impact on the classifier response include the photon properties, reconstructed invariant mass of the signal top quark, reconstructed b and c jet energies and the total energy of the event, flavour tagging results and the ratio of χ^2 values for the signal and background hypotheses. The resulting distributions of the BDT classifier response for the signal and background (SM top-quark decays plus other

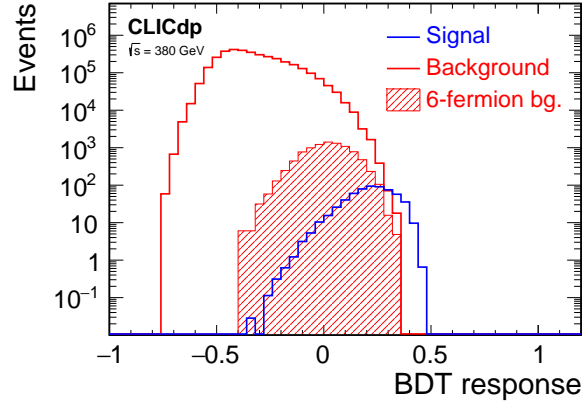


Figure 25: Distribution of the BDT classifier response for events with FCNC top-quark decay $t \rightarrow c\gamma$ (signal, blue histogram) and SM events (background, red histogram), for FCNC selection at 380 GeV CLIC. The background sample is normalised to 500 fb^{-1} while the signal (events with FCNC decay) is normalised to $\text{BR}(t \rightarrow c\gamma) = 10^{-3}$. The hatched histogram indicates the contribution from the six-fermion background.

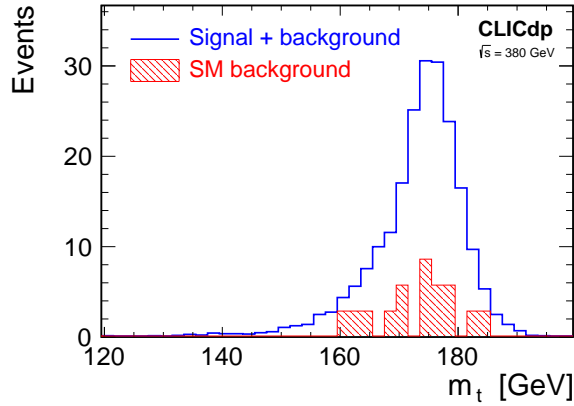


Figure 26: Invariant mass distribution of the top quark from the FCNC decay $t \rightarrow c\gamma$ reconstructed at 380 GeV CLIC after selection based on the BDT response. The distribution is normalised to 500 fb^{-1} and $\text{BR}(t \rightarrow c\gamma) = 10^{-3}$ for the signal events. The hatched histogram indicates the SM background contribution.

SM processes) samples are shown in Figure 25. Although there is a significant overlap of the two distributions, an almost clean sample of signal events can be selected by imposing a tight cut on the BDT response. This is illustrated in Figure 26, where the reconstructed invariant mass distribution for the signal top quark decays is shown after imposing a BDT response cut optimised for signal significance, $\text{BDT score} > 0.29$. With this cut, 28% of the signal events are selected while the background contributions are reduced by three to five orders of magnitude. The total selection efficiency for signal events is 26%. Details on the selection efficiency for the signal and considered

Sample	σ	$\epsilon_{\text{Pre}} (\%)$	$\epsilon_{\text{BDT}>0.29} (\%)$	$N_{\text{BDT}>0.29}$
FCNC $t \rightarrow c\gamma$	1.32 fb	92	28	170
6-fermion	691 fb	2.7	0.14	13
4-fermion	13 pb	16	0.003	33
$q\bar{q}$	21 pb	24	<0.001	-

Table 13: Cross section values, selection efficiencies and numbers of events expected for signal and background processes in the analysis searching for FCNC decay $t \rightarrow c\gamma$ at CLIC at 380 GeV. Numbers of events correspond to a luminosity of 500 fb^{-1} , assuming unpolarised beams, and $\text{BR}(t \rightarrow c\gamma) = 10^{-3}$ for signal events.

background processes are presented in Table 13. The expected limit on the branching ratio of the FCNC top-quark decay $t \rightarrow c\gamma$ is extracted from a comparison of the measured BDT response distribution with the distributions expected for the background and signal+background hypotheses. The expected 95% C.L. limit calculated using the CL_s approach [133] is

$$\text{BR}(t \rightarrow c\gamma) < 4.7 \cdot 10^{-5}$$

for 500 fb^{-1} collected at 380 GeV. The limit was calculated with RooStats [134] using the frequentist limit calculator method, assuming no signal contribution.

FCNC top-quark couplings to γc and $Z c$ can also be constrained from the limit on the single top-quark production $e^+e^- \rightarrow t\bar{c}$. Although these measurements have not been studied in detail for CLIC, estimates based on a fast simulation approach presented for the FCC-ee running at 350 GeV [135] indicate that the limit expected from a search for single-top production at 380 GeV CLIC would be weaker than the one resulting from the direct search for the decay $t \rightarrow c\gamma$, presented above.

9.2 $t \rightarrow cH$

For the top-quark FCNC decay $t \rightarrow cH$ we consider only the final state with the Higgs boson decaying to two b quarks, $H \rightarrow b\bar{b}$, which has the dominant contribution of about 58% in the SM. This FCNC decay channel is challenging as the expected final state is the same as for the SM top-quark pair decays (six jets for the fully-hadronic channel or four jets, an isolated lepton and missing energy for the semi-leptonic channel). Signal-background discrimination can only be based on the kinematic event properties and the flavour tagging.

Signal samples were generated with WHIZARD 2.2.8 [61, 132] using the 2HDM(III) model [136] implemented in SARAH [137]. The background sample considered in the analysis includes a full set of 6-fermion event samples produced for the study of top-quark pair production at $\sqrt{s} = 380 \text{ GeV}$ described in Section 7. Backgrounds from four-fermion final state events (dominated by $W^+ W^-$ production) and from pair production of quarks other than the top quark are also included. To maximize the experimental sensitivity, electron beam polarisation of -80% was assumed for this study.

Searches for FCNC decays of the top quark are made in both the fully-hadronic and semi-leptonic event samples. The analysis is divided into two steps: pre-selection and classification of $t\bar{t}$ candidate events, and final discrimination between FCNC and SM top-quark decays optimised for limit setting. For the first step, the pre-selection cut and BDT algorithm developed for top-quark pair event classification are used, as described in [Section 6.3](#). As expected, almost all FCNC signal events are classified as hadronic or semi-leptonic top-quark pair events, with both the pre-selection efficiency (ϵ_{Pre}) and classification efficiency (ϵ_{cl}) of about 99%, see [Table 14](#).

When reconstructing the decay kinematics we look for the jet combination that minimises the χ^2 value for the corresponding hypothesis. However, to reduce the number of possible jet configurations (30 possible combinations for the six-jet final state), an additional, tighter cut on the flavour tagging results is applied first. Only events with at least three jets with b-tag > 0.4 and one jet with c-tag > 0.4 are considered as FCNC signal candidates. Two of these b-jets and a c-jet are then considered as candidates for the FCNC top-quark decay products (with the Higgs boson decaying to two b-jets). While the efficiency of these cuts (ϵ_{FCNC}) for signal events is about 45%, all backgrounds from SM processes are significantly suppressed. Moreover, the number of jet configurations fitting the signal or background hypothesis is reduced. The valid configurations are then compared based on the χ^2 value for the event. For the SM top-quark pair decay hypothesis, the χ^2 formula from the top-quark mass reconstruction is used, as described in [Section 6.3](#). A similar χ^2 formula is used for the FCNC top-quark pair decay hypothesis, but with one of the W boson masses replaced by the mass of the Higgs boson.

The reconstructed final state kinematics and the flavour tagging results are used as an input for the final BDT selection optimised to discriminate between signal and background events. The following variables are used for BDT training: χ^2 values for signal and background hypotheses, reconstructed Higgs boson mass and W boson mass from the spectator top-quark decay, the smaller of the two b-tag values for the jets from Higgs boson decay, the c-tag and b-tag value for the c-quark from FCNC decay, the b-tag value for the b-jet from the spectator top-quark decay, the smaller of the two b-tag values for jets from top-quark decays (for the background hypothesis) and the responses of the BDT classifier used at the event classification stage (for hadronic and semi-leptonic event selection, see [Section 6.3](#)). The resulting response distributions from the BDT classifier are presented in [Figure 27](#), separately for the hadronic and the semi-leptonic samples. The background sample is normalised to 500 fb^{-1} while the signal (events with a FCNC top quark decay) are normalised to $\text{BR}(t \rightarrow cH) \times \text{BR}(H \rightarrow b\bar{b}) = 10^{-3}$. To select a signal-dominated sample a relatively tight selection cut on the BDT response is required. Details on the selection efficiency for the different event samples considered in the analysis are presented in [Table 14](#). For the cut on the response of the final BDT score, > 0.4 , the total selection efficiency for FCNC events is 11% while the suppression of the SM $t\bar{t}$ background is at the level of $1.4 \cdot 10^{-4}$ and the non- $t\bar{t}$ backgrounds are suppressed at the level of 10^{-6} .

The expected limit on the branching ratio of the FCNC top-quark decay $t \rightarrow cH$ is extracted from a comparison of the measured BDT response distribution with the distributions for the background and signal+background hypotheses. The 95% C.L. limit calculated with the CL_s approach [[133](#)] is

$$\text{BR}(t \rightarrow cH) \times \text{BR}(H \rightarrow b\bar{b}) < 1.2 \times 10^{-4},$$

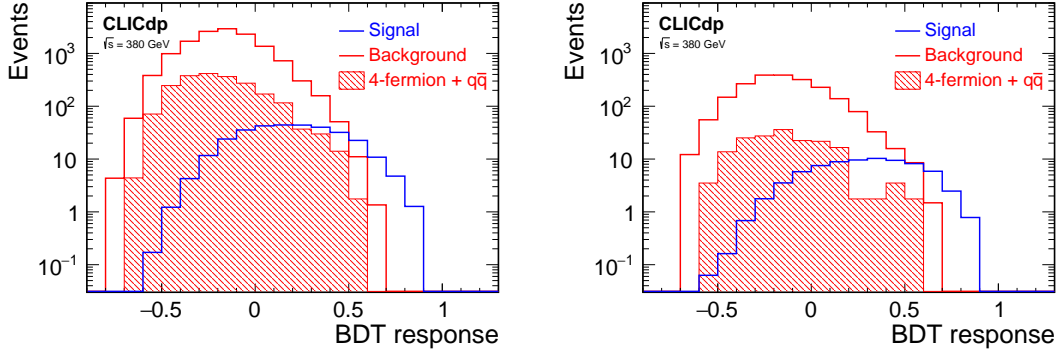


Figure 27: Response distribution of the BDT classifier used for the final $t \rightarrow cH$ event selection at $\sqrt{s} = 380$ GeV, for hadronic (left) and semi-leptonic (right) event samples. The total background (red histogram) is normalised to 500 fb^{-1} while the signal (events with a FCNC top quark decay; blue histogram) is normalised to $\text{BR}(t \rightarrow cH) \times \text{BR}(H \rightarrow b\bar{b}) = 10^{-3}$. The hatched histogram indicates the contribution from four fermion and quark-pair backgrounds.

Sample	σ	$\epsilon_{\text{Pre}} (\%)$	$\epsilon_{t\bar{t}} (\%)$	$\epsilon_{\text{FCNC}} (\%)$	$\epsilon_{\text{BDT} > 0.4} (\%)$	$N_{\text{BDT} > 0.4}$
FCNC $t \rightarrow cH$	1.79 fb	99	99	45	25	98
6-fermion	938 fb	88	90	3.6	0.51	68
4-fermion	21 pb	8.5	5.1	2.8	0.97	12
$q\bar{q}$	26 pb	20	1.1	3.3	0.94	9

Table 14: Cross section values, selection efficiencies, and numbers of events expected for signal and background processes in the analysis searching for FCNC decay $t \rightarrow cH$ at CLIC at 380 GeV. Selection efficiencies are quoted for pre-selection (ϵ_{Pre}) and classification ($\epsilon_{t\bar{t}}$) of $t\bar{t}$ events, as well as for selection of FCNC candidate events (ϵ_{FCNC}) and selection of signal dominated sample with cut on BDT response ($\epsilon_{\text{BDT} > 0.4}$). Numbers of events correspond to a luminosity of 500 fb^{-1} , assuming -80% electron beam polarisation, and $\text{BR}(t \rightarrow cH) \times \text{BR}(H \rightarrow b\bar{b}) = 10^{-3}$ for signal events.

for 500 fb^{-1} collected at 380 GeV with electron beam polarisation of -80%.

9.3 $t \rightarrow c\cancel{E}$

We search for events where the top quark decays into a charm quark and a heavy stable particle, which escapes from the detector, giving a characteristic ‘missing energy’ signature. As the mass of the produced heavy state has to be reconstructed from energy-momentum conservation, only the hadronic decay channel is considered for the spectator top quark. For the expected final state consisting of four jets, the dominant background contribution is from processes with four fermions in the final state, primarily from $W^+ W^-$ decays. To model the decay to an invisible scalar particle, dedicated samples of events with $t \rightarrow cH$ decay were generated, as described in [Section 9.2](#),

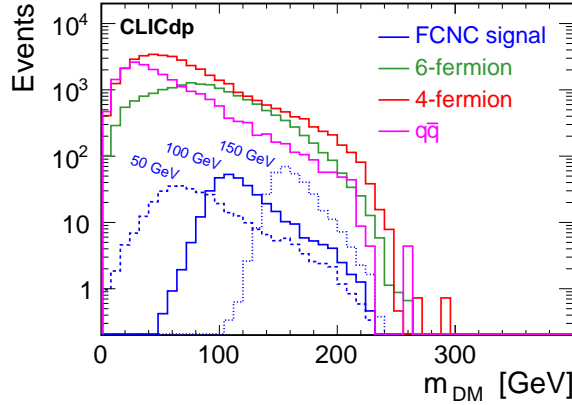


Figure 28: Distribution of the reconstructed invariant mass of the invisible decay product for the FCNC decay $t \rightarrow c \bar{\ell}$, reconstructed at 380 GeV CLIC after preselection cuts. The background contributions coming from 6-fermion (green histogram), four-fermion (red) and quark pair (magenta) production processes are normalised to 500 fb^{-1} while the signal samples, for the assumed mass of the invisible scalar of 50, 100 and 150 GeV (blue histograms) are normalised to $\text{BR}(t \rightarrow c \bar{\ell}) = 10^{-3}$.

with the Higgs boson defined as a stable particle in PYTHIA (and thus invisible in the detector). Signal samples for scalar masses from 25 to 150 GeV were generated assuming an electron beam polarisation of -80%.

To reduce large backgrounds coming from four-fermion and quark-pair production processes a set of pre-selection cuts is applied. We require the total invariant mass of the hadronic final state to be above 140 GeV, the total transverse momentum above 20 GeV, and the absolute value of the longitudinal momentum below 100 GeV. After clustering the hadronic final state into four jets, using the VLC algorithm with a radius of 1.6 and $\beta = \gamma = 0.8$, we require one of the resulting jets to have a b-tag value of at least 0.6 (for the b-jet candidate from the decay of the spectator top-quark) and all other jets to have a b-tag value below 0.4. We also reject all events with a reconstructed isolated lepton.

To reconstruct the kinematics of the event we assume that the jet with the highest c-tag value comes from the FCNC top-quark decay while the two remaining jets result from the W boson decay. This choice of jet configuration matches the true decay kinematics in about 70% to 75% of signal events (depending on the scalar mass). The invariant mass of the signal top-quark as well as the invariant mass of the invisible decay product can then be reconstructed from the energy-momentum conservation. Figure 28 shows the distribution of the reconstructed invariant mass of the invisible decay product for signal events (for the scalar masses of 50, 100 and 150 GeV) and for different background samples. For the signal samples the efficiency of the pre-selection cuts described above varies between 35% and 42% (depending on the scalar mass), while for the four-fermion and quark-pair background samples it is about 0.35% to 0.16%, respectively.

For the final discrimination between the FCNC decay events and the SM background processes, a

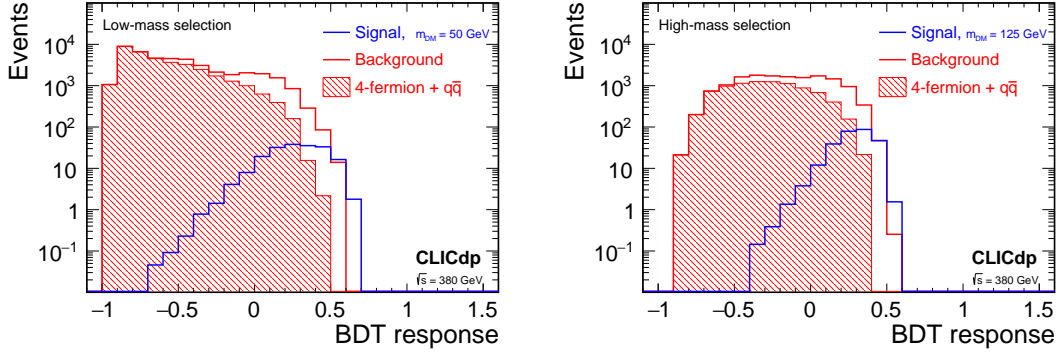


Figure 29: Response distributions of the BDT classifiers used for the final selection of $t \rightarrow c\cancel{E}$ events at $\sqrt{s} = 380 \text{ GeV}$, for an assumed mass of the invisible decay product of 50 GeV (low mass selection; left) and 125 GeV (high mass selection; right). The total background (red histogram) is normalised to 500 fb^{-1} while the signal (events with a FCNC top quark decay; blue histogram) is normalised to $\text{BR}(t \rightarrow c\cancel{E}) = 10^{-3}$. The hatched histogram indicates the contribution from four fermion and quark-pair backgrounds.

multivariate analysis is used. The BDT classification algorithm is trained, separately for low scalar masses (signal scalar masses of 25 GeV, 50 GeV and 75 GeV) and high scalar masses (signal scalar masses of 100 GeV, 125 GeV and 150 GeV). The set of variables includes: total energy of the event E_{tot} , total transverse momentum p_T , total invariant mass M_{inv} , missing mass M_{miss} , sphericity and acoplanarity of the event, minimum (y_{min}) and maximum (y_{max}) distance cuts for four-jet reconstruction with the VLC algorithm, b-jet energy and invariant mass, reconstructed masses of the two top quarks, reconstructed mass and energy of the invisible scalar, and the χ^2 value calculated from the reconstructed masses of the W boson and two top quarks. For each considered value of the invisible scalar particle mass the BDT response distribution was plotted for events in the $\pm 30 \text{ GeV}$ window in the reconstructed particle mass. Examples of the response distributions for the low mass and high mass BDT classifiers, for the selected masses of 50 GeV and 125 GeV, are shown in Figure 29. Details on the selection efficiency for the two selected values of the invisible scalar mass are summarised in Table 15. For high values of BDT response, $\text{BDT} > 0.25$, the background is dominated by the six-fermion sample, while the suppression factor for four-fermion and quark-pair background is at the level of 10^{-5} and 10^{-6} , respectively.

Expected limits on the branching ratio of the FCNC top-quark decay $t \rightarrow c\cancel{E}$ were calculated as a function of the scalar particle mass from a comparison of the measured BDT response distribution (in the $\pm 30 \text{ GeV}$ reconstructed mass window) with the distributions expected for the background only hypothesis and the one including signal contribution. The limits calculated using the CL_s approach [133] for 500 fb^{-1} collected at 380 GeV are summarised in Figure 30.

Sample	σ	$\epsilon_{\text{Pre}} (\%)$	$\epsilon_{\text{BDT}>0.25} (\%)$	$N_{\text{BDT}>0.25}$
<i>Low mass selection, $m_{DM} = 50 \text{ GeV}$</i>				
FCNC $t \rightarrow c\cancel{E}$	1.79 fb	41	29	105
6-fermion	938 fb	4.0	3.3	635
4-fermion	21 pb	0.35	0.17	64
$q\bar{q}$	26 pb	0.16	0.11	22
<i>High mass selection, $m_{DM} = 125 \text{ GeV}$</i>				
FCNC $t \rightarrow c\cancel{E}$	1.79 fb	40	51	181
6-fermion	938 fb	4.0	4.0	731
4-fermion	21 pb	0.35	0.20	76.3
$q\bar{q}$	26 pb	0.16	0.042	8.8

Table 15: Cross section values, selection efficiencies and numbers of events expected for signal and background processes in the analysis searching for FCNC decay $t \rightarrow c\cancel{E}$ at CLIC at 380 GeV. Results are presented for a mass of the invisible scalar particle, m_{DM} , of 50 GeV (upper part of the table) and 125 GeV (lower part). Selection efficiencies are quoted for pre-selection (ϵ_{Pre}) and the final selection of the signal enhanced sample with the BDT response cut, $\text{BDT}>0.25$. Numbers of events correspond to a luminosity of 500 fb^{-1} , assuming -80% electron beam polarisation, and $\text{BR}(t \rightarrow c\cancel{E}) = 10^{-3}$ for signal events.

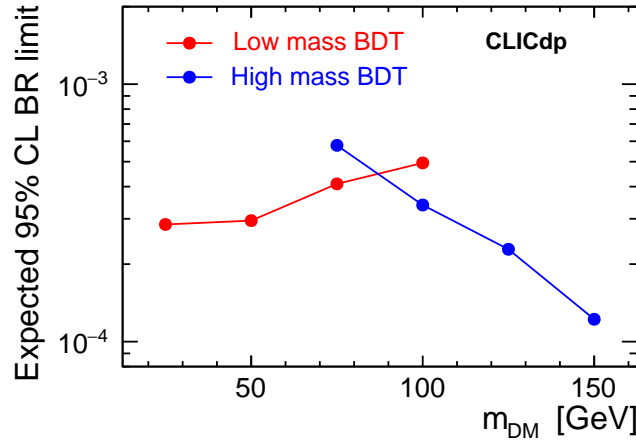


Figure 30: Limits at 95% C.L. on the top quark FCNC decay $t \rightarrow c\cancel{E}$ expected for 500 fb^{-1} collected at 380 GeV CLIC with -80% electron beam polarisation, as a function of the assumed mass of the invisible decay product, m_{DM} . Limits are calculated from the BDT response distribution in the $\pm 30 \text{ GeV}$ window in the reconstructed particle mass. Two BDT algorithms are trained separately for low and high mass range.

10 Phenomenological interpretations

The capabilities of CLIC to improve our knowledge of top-quark physics can be directly illustrated by studying the sensitivity to new physics in the top-quark sector. This section describes the BSM implications of such top-quark measurements. We start from a general EFT interpretation, followed by a more specific analysis in the context of top-quark compositeness scenarios.

The results presented are based on full simulation studies at all three stages of CLIC. Note however, that the results, to some extent, are partial in the sense that they do not include all the top-quark related measurements possible at CLIC. Furthermore, the results should be studied in the broader context of the global sensitivity of CLIC to the SM EFT, which will be discussed elsewhere. Still, the studies presented here clearly illuminate the physics potential of CLIC in the top-quark sector.

10.1 General top-philic interpretation

Under the simple hypothesis of top-philic BSM, motivated and outlined in [Section 3.5](#), it is possible to restrict the global EFT interpretation of top-quark physics to the nine operators reported in [Table 3](#). For simplicity, we further restrict the analysis presented below to CP-conserving BSM physics, which implies real operator coefficients, leading to a total of nine real parameters to be determined.^{xvi} The $e^+e^- \rightarrow t\bar{t}$ top-quark pair production process is sensitive to seven of these operators. The two missing ones are the combination $Q_{\phi q}^{(1)} + Q_{\phi q}^{(3)}$, which do not contribute to the top-quark electroweak couplings, and $Q_{t\phi}$. The latter operator modifies the top Yukawa coupling by an amount $\Delta y_t = v^2 C_{t\phi}$, where $v = 246$ GeV and $C_{t\phi}$ is the Wilson coefficient of the corresponding operator $Q_{t\phi}$. Hence it is probed at 1σ level by the $t\bar{t}H$ analysis reported in [Section 8.1](#)^{xvii}:

$$[C_{t\phi}]_{1\sigma} = \frac{1}{v^2} [\Delta y_t]_{1\sigma} \simeq 0.6 \text{ TeV}^{-2}. \quad (10.1)$$

While it corresponds to a rather low “operator scale” $\Lambda_{t\phi} \equiv 1/\sqrt{C_{t\phi}} \simeq 1.3$ TeV, we will see in the next section that this sensitivity allows to probe a much higher new physics scale in top-quark compositeness scenarios, where $C_{t\phi}$ can be enhanced by a strong coupling. The operator combination $Q_{\phi q}^{(1)} + Q_{\phi q}^{(3)}$ does not affect the electroweak interactions of the top-quark, as mentioned, but it does modify the left-handed $b\bar{b}Z$ coupling as $\delta g_{b,L}/g_{b,L} = (C_{\phi q}^{(1)} + C_{\phi q}^{(3)})v^2/(c_w^2 + s_w^2/3)$, where c_w (s_w) is the cosine (sine) of the weak mixing angle. The sensitivity of LEP to the bottom couplings was at the per mille level, corresponding to

$$[C_{\phi q}^{(1)} + C_{\phi q}^{(3)}]_{1\sigma} \simeq 1.4 \cdot 10^{-2} \text{ TeV}^{-2} \simeq [8 \text{ TeV}]^{-2}. \quad (10.2)$$

It is thus legitimate to restrict the EFT analysis of the top-quark pair production to the orthogonal combination $Q_{\phi q}^{(1)} - Q_{\phi q}^{(3)}$, i.e. to set $C_{\phi q}^{(1)} = -C_{\phi q}^{(3)}$ and report results for $C_{\phi q}^- = C_{\phi q}^{(1)} - C_{\phi q}^{(3)}$. Note

^{xvi} CP-breaking new physics could also be studied, but this would require taking into account potentially strong constraints from electric dipole moments and other low-energy probes. This goes beyond the scope of the present studies, see however [\[111\]](#).

^{xvii} This corresponds to the single-operator sensitivity to $C_{t\phi}$, i.e. the sensitivity when $Q_{t\phi}$ is the only operator with a BSM effect. A global EFT interpretation of the $t\bar{t}H$ analysis, duly combined with $t\bar{t}$ production and with the other probes of top-quark physics, would be needed for a more robust assessment of the sensitivity.

that $Q_{\phi q}^{(1)} + Q_{\phi q}^{(3)}$ is the only combination of the top-philic operators that modifies the bottom quark interactions with the gauge fields, hence no further LEP constraint needs to be taken into account.

The seven operators that contribute to top-quark pair production are probed through the measurement of statistically optimal observables. These are defined on the fully differential $e^+e^- \rightarrow t\bar{t} \rightarrow bW^+\bar{b}W^-$ final state and include total rate information. The differential distributions are computed at LO for a massless b-quark, in the narrow-width approximation for the top quark, ignoring ISR and beamstrahlung. For simplicity, covariance matrices in the EFT parameter space are obtained by numerical integration of leading-order analytical expressions. The EFT expansion is truncated at the linear level, an approximation which is found to be accurate for this set of observables and a full linear collider physics programme.

The realistic overall efficiencies for semi-leptonic final states, as presented in [Section 7.1](#) and [Section 7.3](#), are applied. As demonstrated in these analyses, the background levels are small compared to the signals; for technical reasons we have neglected the backgrounds in the following EFT studies. Including final-states with a tau lepton, or the fully-hadronic channel could ultimately also somewhat strengthen the constraints presented. The employment of the statistically optimal observable in the context of a global EFT fit is described in great detail in [111], together with a

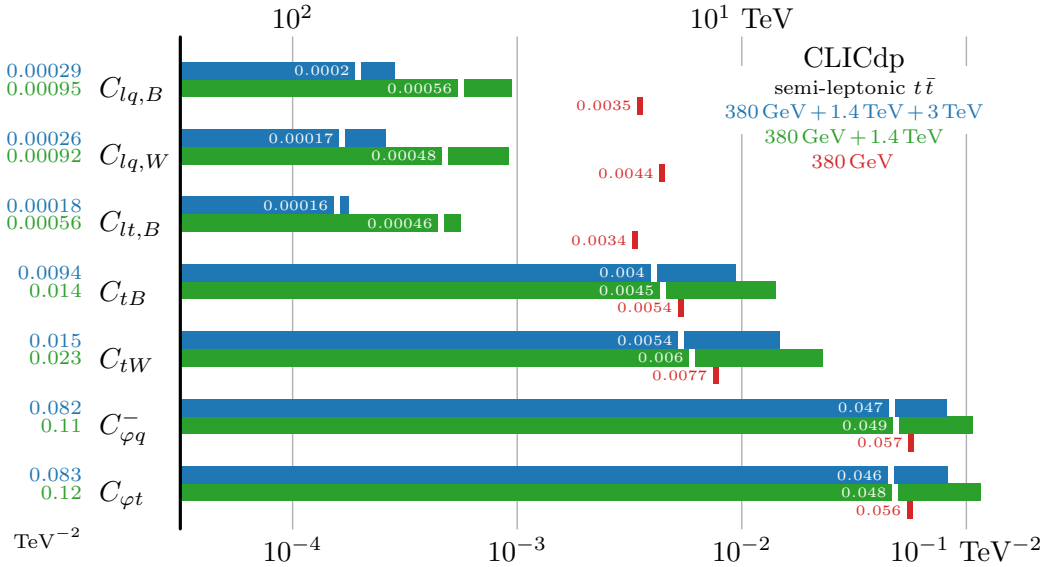


Figure 31: Summary of the global EFT analysis results using statistically optimal observables for the three CLIC energy stages. The colour bars indicate the 1σ constraints on each of the seven Wilson coefficients. The blue bars illustrate the results for the full CLIC programme of consecutive operation at 380 GeV, 1.4 TeV, and 3 TeV, using respectively 500 fb^{-1} , 1.5 ab^{-1} , and 3 ab^{-1} , equally shared between $P(e^-) = (\pm 80\%)$ beam polarisation configurations. Similarly, the green bars give the results of operation at 380 GeV and 1.4 TeV, excluding the 3 TeV stage. The corresponding individual operator sensitivities are shown as ticks. Note that a global fit is not possible for operation at 380 GeV alone, for which the individual operator constraints are shown in red.

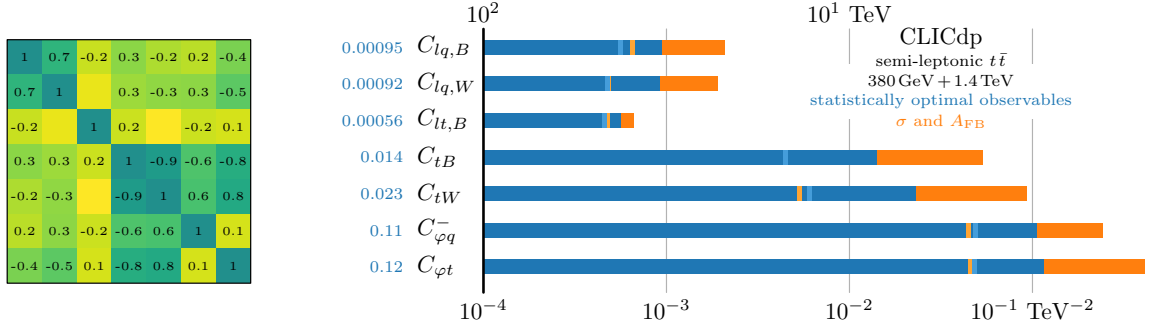


Figure 32: Global EFT analysis results for top-quark pair production at the 380 GeV and 1.4 TeV CLIC, using respectively 500 fb⁻¹ and 1.5 ab⁻¹ of integrated luminosity equally shared between $P(e^-) = (\pm 80\%)$ beam polarisation configurations. 1 σ sensitivities to the seven Wilson coefficients for the statistically optimal observables are shown in blue bars and for the combination of A_{FB} and $\sigma_{t\bar{t}}$ in orange bars. The corresponding single-operator sensitivities are shown as ticks of the same colour for the two set of operators. The correlation matrix among the Wilson coefficients for the fits using the statistically optimal observables (left).

comparison with previous studies [116–118].

Figure 31 displays the global and individual 1 σ constraints on the seven Wilson coefficients obtained for operation at $\sqrt{s} = 380$ GeV only, in combination with the 1.4 TeV stage, and including also the 3 TeV stage. Note that the reach of the initial CLIC stage alone does not allow for the simultaneous determination of the seven Wilson coefficients. The sensitivities are measured in TeV⁻² on the lower horizontal axis (and reported in numbers of the same unit), while the upper horizontal axis reports the sensitivity to the operator scale $\Lambda \equiv 1/\sqrt{C}$. The individual-operator constraints are reported as numbers and ticks along each colour bar.

We see that operation at high energy dramatically improves the sensitivity to the 4-fermion operators $Q_{lq,B}$, $Q_{lq,W}$, and $Q_{lt,B}$, and to a lesser extent, to Q_{tB} and Q_{tW} . This is due to the fact that the 4-fermion operators give a contribution to the amplitude that grows quadratically with the centre-of-mass energy. The contributions to the amplitude of the operators Q_{tB} and Q_{tW} also grow with energy, but only linearly, and so the improvement is less significant. The sensitivity to the 4-fermion operators improves by more than one order of magnitude with the high-energy stages.

The results of this global fit exploiting statistically optimal observables are compared with the ones obtained with measurements of cross sections and forward-backward asymmetries in Figure 32 and Figure 33. Uncertainties computed analytically and corrected with realistic efficiencies are also employed in this second fit. Note that individual limits are sometimes better for the latter operators due to larger efficiencies at $\sqrt{s} = 380$ GeV; such a feature is not seen for four-fermion operators whose constraints are driven by the high energy runs. Figure 32 includes the results for CLIC operation at 380 GeV and 1.4 TeV, while Figure 33 also include the 3 TeV results. Correlation matrices are displayed for the fits using the statistically optimal observables. By combining the sensitivities to the seven Wilson coefficients and the correlations among them one can reconstruct

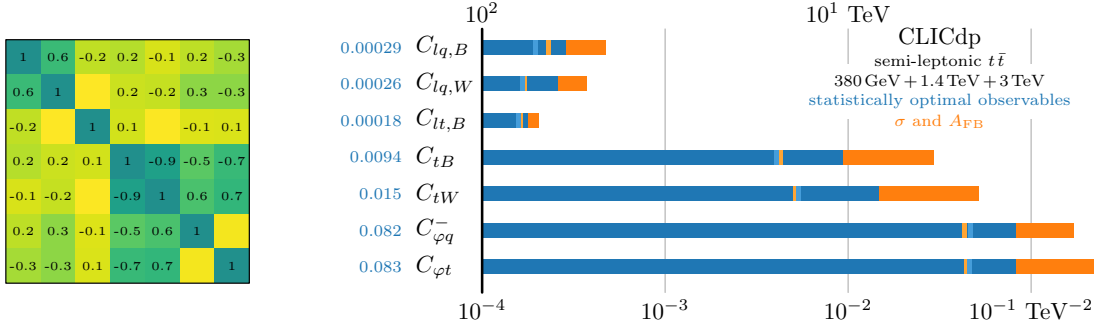


Figure 33: Same as Figure 32, but including operation at 3 TeV CLIC with 3 ab^{-1} integrated luminosity.

the likelihood and use it for a rigorous reinterpretation of the result in explicit BSM scenarios where theoretical correlations are present among the operator coefficients. This is done for two top-quark compositeness scenarios as presented in Section 10.2.

10.2 Top-quark compositeness

Scenarios where supposedly elementary SM particles are actually composite bound states originating from more fundamental dynamics are particularly well-motivated for the Higgs boson since Higgs compositeness at the TeV scale would arguably be the simplest solution to the Electroweak Naturalness Problem. The same is true also for the top quark, whose dynamics are strongly tied to that of the Higgs boson. Here we focus on the “canonical” scenario (see [138] for a recent review) where the Higgs boson is a pseudo-Nambu–Goldstone boson of an underlying strongly-interacting composite sector, broadly characterised by a mass scale m_* and by a coupling strength parameter g_* [139]. Top-quark compositeness emerges naturally in this framework [107], and it is actually believed to be the only viable option to generate the top Yukawa coupling [140].

In this model, top-quark compositeness is characterised by two couplings, y_L and y_R , that control the strength of the mixing of the q_L doublet and of the t_R singlet to the composite sector dynamics, respectively. In order for $y_{L,R}$ to produce a realistic top Yukawa coupling, they have to fulfil parametrically (i.e., up to dimensionless factors) the relation

$$y_t \simeq \frac{y_L y_R}{g_*}. \quad (10.3)$$

There are infinitely many ways to satisfy Equation 10.3; the only constraint is $y_{L,R} \leq g_*$ (out of which one derives $g_* > y_t$) for internal consistency of the construction. It is however sufficient to focus on two benchmark scenarios:

$$\text{Partial compositeness: } y_L = y_R = \sqrt{y_t g_*}, \quad (10.4)$$

$$\text{Total } t_R \text{ compositeness: } y_L = y_t, y_R = g_*. \quad (10.5)$$

The names reflect the fact that the presence of the $y_{L,R}$ mixings make the physical q_L and t_R particles an admixture of elementary and composite degrees of freedom, with a fraction of compositeness

y_L/g_* and y_R/g_* , respectively. For the partial compositeness scenarios in Equation 10.4, the two chiralities possess the same compositeness fraction, while for total t_R compositeness scenarios in Equation 10.5, the right-handed component is a fully composite state and the left-handed one is mostly elementary. The third logical possibility would be fully composite $q_L = \{t_L, b_L\}$; however, this is disfavoured by the constraints from bottom quark physics.

The couplings y_L , y_R and g_* control, together with the mass scale m_* of the BSM particles, the expected magnitude of the $d = 6$ EFT operators that are obtained in models of this sort by integrating out the composite sector dynamics. The power-counting formula reads

$$\mathcal{L}^{d=6} = \frac{1}{m_*^2} \frac{1}{g_*^2} \widehat{\mathcal{L}}[y_L q_L, y_R t_R, g_* \phi, g_V V_\mu], \quad (10.6)$$

where $\widehat{\mathcal{L}}$ is a generic (gauge-invariant) $d = 6$ local functional of the fields and their derivatives with dimensionless coefficients. The Higgs field ϕ is fully composite, hence it appears with coupling g_* . The SM gauge fields, which are collectively denoted as V , are elementary and couple through gauge interactions, i.e. with the ordinary SM gauge couplings g_V . The composite sector coupling g_* is necessarily larger than y_t , as previously mentioned, but apart from this it can a priori assume any value up to the maximal coupling strength of 4π . Large g_* values are perfectly plausible or even expected because of the underlying strongly interacting nature of the composite sector. It is thus important to explore the whole range $g_* \in [y_t, 4\pi]$, including values well above 1, for which Equation 10.6 predicts large departures from the naive $1/m_*^2$ estimate of the Wilson coefficients.

Based on Equation 10.6, the coefficients of the top-philic operators in Table 3 can be estimated up to dimensionless coefficients, denoted as “ γ ”. The coefficients are grouped into four categories:

Higgs current operators:

$$C_{\phi t} = y_R^2 \gamma_{\phi t} \frac{1}{m_*^2}, \quad C_{\phi q}^{(1)} = y_L^2 \gamma_{\phi q}^{(1)} \frac{1}{m_*^2}, \quad C_{\phi q}^{(3)} = y_L^2 \gamma_{\phi q}^{(3)} \frac{1}{m_*^2} \quad (10.7)$$

Most models enjoy an accidental symmetry, dubbed P_{LR} custodial [141], that enforces $C_{\phi q}^{(1)} + C_{\phi q}^{(3)} = 0$ up to small loop corrections. Hence in what follows we will set $\gamma_{\phi q}^{(1)} = -\gamma_{\phi q}^{(3)}$ and consequently we ignore the $b\bar{b}Z$ constraint in Equation 10.2. Ordinary custodial symmetry can also suppress $\gamma_{\phi t}$, which are thus also set conservatively to zero. At large g_* these operators (or at least the remaining combination) are significantly enhanced, particularly so in the total t_R compositeness scenario in Equation 10.5.

Modified top Yukawa:

$$C_{t\phi} = y_L y_R g_* \gamma_{t\phi} \frac{1}{m_*^2} = y_t g_*^2 \gamma_{t\phi} \frac{1}{m_*^2} \quad (10.8)$$

where we used Equation 10.3. Note the quadratic enhancement with g_* , which boosts the sensitivity to m_* of the y_t determination in Equation 10.1.

Four-fermion operators:

$$C_{lt,B} = g^2 \frac{y_R^2}{g_*^2} \gamma_{lt,B} \frac{1}{m_*^2} \quad C_{lq,B} = g^2 \frac{y_L^2}{g_*^2} \gamma_{lq,B} \frac{1}{m_*^2} \quad C_{lq,W} = g^2 \frac{y_L^2}{g_*^2} \gamma_{lq,W} \frac{1}{m_*^2} \quad (10.9)$$

These operators emerge from couplings with the gauge fields, as indicated in [Table 3](#), hence their coefficient is proportional to the corresponding gauge coupling. They are subsequently converted into four-fermion operators through equations of motion, and this brings a second power of the gauge coupling. Their coefficients are all suppressed at large g_* in the partial compositeness scenario, while for total t_R compositeness one of them, C_{tB} , is unsuppressed.

Dipole operators:

$$C_{tB} = y_t g' \gamma_{tB} \frac{1}{m_*^2} \cdot \left(\frac{g_*^2}{16\pi^2} \right) \quad C_{tW} = y_t g \gamma_{tW} \frac{1}{m_*^2} \cdot \left(\frac{g_*^2}{16\pi^2} \right) \quad (10.10)$$

The loop suppression factor clearly does not emerge from the power-counting formula in [Equation 10.6](#). It is included because in all known perturbative (i.e., $g_* < 4\pi$) realisations of the composite Higgs scenario these operators cannot be generated at tree-level. While we cannot exclude the existence of perturbative models that do not experience such a suppression, we include the loop factor in order to obtain a conservative estimate of the sensitivity.

The results from the global EFT fit reported in [Section 10.1](#) were employed for an assessment of the CLIC exclusion and discovery reach of the top-quark compositeness scenarios at 3 TeV. The results, focussing on 5σ discovery for brevity, are reported in [Figure 34](#). The figure is obtained by varying the dimensionless parameters γ in the range $[1/2, 2]$ independently, and taking the values that minimise or maximise the likelihood at each point of the (m_*, g_*) plane. This produces two discovery contours, that each correspond to optimistic and pessimistic assumptions on the values of γ that will be obtained in the underlying UV theory. The impact of the top-quark pair production analysis (from [Figure 31](#)) is shown separately from the top Yukawa determination in [Equation 10.1](#). For the latter we only display the optimistic case which is still less powerful than the reach of $t\bar{t}$.

The four-fermions operators, due to the very strong sensitivity from operation at $\sqrt{s} = 3$ TeV play a dominant role in the reach. The conclusion is that top-quark compositeness can be discovered at CLIC up to 7 TeV, and more than 20 TeV can be reached in favourable configurations. In particular, top-quark compositeness emerging in connection to the Naturalness Problem can be conclusively probed at CLIC.

11 Summary and conclusions

A detailed study of the top-quark physics reach of CLIC has been presented in this paper, in the context of CLIC operating at three energy stages: 500 fb^{-1} at $\sqrt{s} = 380$ GeV, 1.5 ab^{-1} at 1.4 TeV and 3 ab^{-1} at 3 TeV.

The initial stage of operation includes an energy scan in the top-quark pair production threshold region, which allows the top-quark mass to be extracted in a theoretically well-defined manner with a precision of around 50 MeV assuming an integrated luminosity of 100 fb^{-1} . Additional mass measurements at 380 GeV, based on the reconstruction of hadronic top-quark decays or the energy spectrum of ISR photons with complementary systematic uncertainties, might improve the overall understanding of the top-quark mass further.

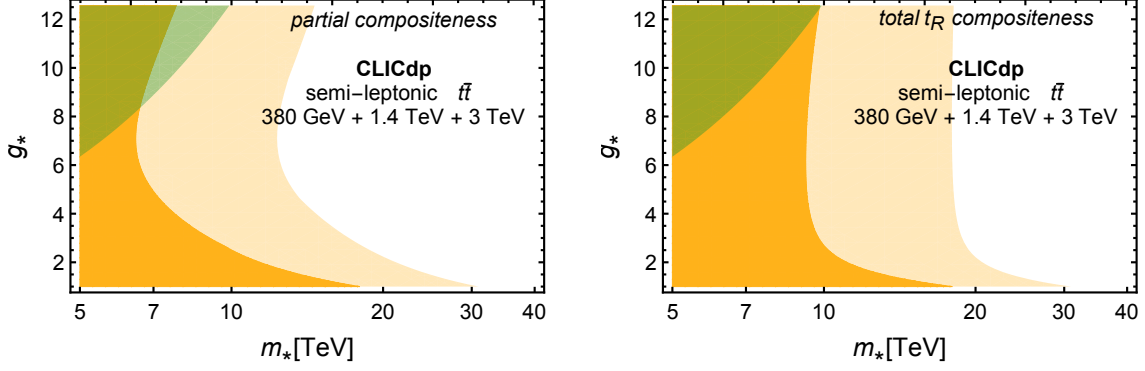


Figure 34: “Optimistic” (light color) and “pessimistic” (dark color) 5σ discovery regions for the partial compositeness (left) and the total t_R compositeness (right) scenarios. The orange contours are derived from the $t\bar{t}$ global fit in [Section 10.1](#), while the green contour is derived from the top Yukawa analysis in [Equation 10.1](#). Only the optimistic case is shown for the top Yukawa analysis.

The large number of top quarks produced at 380 GeV in combination with the relatively low background levels and c-tagging capabilities of the CLIC detector concepts allow competitive searches for FCNC decays with charm quarks in the final state, such as $t \rightarrow c\gamma$ and $t \rightarrow cH$.

Pair production of the top quark in electron-positron collisions gives access to its electroweak couplings. At 380 GeV the jets from top-quark decays are well separated and can be reconstructed individually. Boosted top tagging techniques based on jet substructure information are needed to reconstruct top-quark pair production events with sufficient precision at the higher-energy CLIC stages. Tagging efficiencies for hadronically decaying top quarks in the boosted regime of 50-70% are achieved due to the low background levels, and the high granularity and excellent jet energy resolution of detector concepts optimised for PFA.

A global interpretation of top-quark pair production using seven Wilson coefficients requires at least two energy stages. New physics scales of the order of tens of TeV can be reached. The results of the EFT fit have been used to assess the CLIC sensitivity for top-quark compositeness. The reach of CLIC extends to top-quark compositeness scales of up to about 10 TeV.

The higher-energy stages also allow to study top-quark pair production in association with other particles. At 1.4 TeV the top Yukawa coupling can be measured with a precision of 3.8% using $t\bar{t}H$ events. In addition, the $t\bar{t}H$ process allows to search for a CP-odd contribution to the $t\bar{t}H$ coupling. Further, operation at 3 TeV gives access to top-quark pair production in vector boson fusion.

Acknowledgments

The CLICdp collaboration gratefully acknowledges CERN for its continued support; This work benefited from services provided by the ILC Virtual Organisation, supported by the national resource providers of the EGI Federation. This research was done using resources provided by the Open Science Grid, which is supported by the National Science Foundation and the U.S. Depart-

ment of Energy’s Office of Science. This work was supported by the European Union’s Horizon 2020 Research and Innovation programme under Grant Agreement No. 654168; the European Commission through the Marie Curie Career Integration Grant 631962; the Helmholtz Association, Germany; the DFG Collaborative Research Centre “Particles, Strings and the Early Universe”, Germany; the DFG cluster of excellence “Origin and Structure of the Universe”, Germany; the German – Israel Foundation (GIF); the Israel Science Foundation (ISF); the I-CORE Program, Israel; the Israel Academy of Sciences; the Research Council of Norway; the Institute of High Energy Physics, China under Contract No. Y7515540U1; the National Science Centre, Poland, HARMONIA project under contract UMO-2015/18/M/ST2/00518 and OPUS project under contract UMO-2017/25/B/ST2/00496; the Spanish Ministry of Economy, Industry and Competitiveness under projects MINEICO/FEDER-UE, FPA2015-65652-C4-3-R, FPA2015-71292-C2-1-P and FPA2015-71956-REDT; the IFT Centro de Excelencia Severo Ochoa program, under grants SEV-2012-0249 and SEV-2014-0398, Spain; the Spanish MINECO Ramón y Cajal program (RYC-2014-16022) and the MECD grant FPA2016-78645-P, Spain; the Ministry of Education, Science and Technological Development of the Republic of Serbia under contract No. OI171012; the UK Science and Technology Facilities Council (STFC), United Kingdom; Gonville and Caius College, United Kingdom; and the U.S. Department of Energy, Office of Science under contract DE-AC02-06CH11357.

References

- [1] P. Burrows et al., eds., *Updated baseline for a staged Compact Linear Collider*, [CERN-2016-004](#). CERN, 2016.
- [2] R. Corsini, *Final Results from the CLIC Test Facility (CTF3)*, in [Proc. 8th Int. Particle Accelerator Conf.: Copenhagen, Denmark, May 2017](#), 2017.
- [3] M. Aicheler et al., eds., *A Multi-TeV Linear Collider based on CLIC Technology: CLIC Conceptual Design Report*, [CERN-2012-007](#). CERN, 2012.
- [4] L. Linssen et al., eds., *Physics and Detectors at CLIC: CLIC Conceptual Design Report*, [CERN-2012-003](#). CERN, 2012.
- [5] D. Arominski, *CLIC Beam-Beam Interactions* <http://clic-beam-beam.web.cern.ch/clic-beam-beam/>. CERN, 2018.
- [6] H. Abramowicz et al., *Higgs physics at the CLIC electron-positron linear collider*, [Eur. Phys. J. C77 \(2017\) 475](#) [[hep-ex/1608.07538](#)].
- [7] LINEAR COLLIDER ILD CONCEPT GROUP - collaboration, T. Abe et al., *The International Large Detector: Letter of Intent*, [FERMILAB-LOI-2010-03](#), [FERMILAB-PUB-09-682-E](#), [DESY-09-87](#), [KEK-REPORT-2009-6](#) (2010) [[hep-ex/1006.3396](#)].
- [8] T. Behnke, J. E. Brau, P. N. Burrows, J. Fuster, M. Peskin, M. Stanitzki et al., eds., *The International Linear Collider Technical Design Report - Volume 4: Detectors*. 2013, [physics.ins-det/1306.6329](#).
- [9] H. Aihara, P. Burrows and M. Oreglia, eds., *SiD Letter of Intent*. 2009, [physics.ins-det/0911.0006](#).

- [10] S. Poss and A. Sailer, *Luminosity Spectrum Reconstruction at Linear Colliders*, *Eur. Phys. J.* **C74** (2014) 2833 [[physics.ins-det/1309.0372](#)].
- [11] F. Bach, B. C. Nejad, A. Hoang, W. Kilian, J. Reuter, M. Stahlhofen et al., *Fully-differential Top-Pair Production at a Lepton Collider: From Threshold to Continuum*, [hep-ph/1712.02220](#).
- [12] J. Fuster, I. García, P. Gomis, M. Perelló, E. Ros and M. Vos, *Study of single top production at high energy electron positron colliders*, *Eur. Phys. J.* **C75** (2015) 223 [[hep-ex/1411.2355](#)].
- [13] M. Butenschoen, B. Dehnadi, A. H. Hoang, V. Mateu, M. Preisser and I. W. Stewart, *Top Quark Mass Calibration for Monte Carlo Event Generators*, *Phys. Rev. Lett.* **117** (2016) 232001 [[hep-ph/1608.01318](#)].
- [14] A. H. Hoang and T. Teubner, *Top-quark pair production close to threshold: Top-quark mass, width and momentum distribution*, *Phys. Rev.* **D60** (1999) 114027 [[hep-ph/9904468](#)].
- [15] M. Beneke, *A quark mass definition adequate for threshold problems*, *Phys. Lett.* **B434** (1998) 115 [[hep-ph/9804241](#)].
- [16] P. Marquard, A. V. Smirnov, V. A. Smirnov and M. Steinhauser, *Quark Mass Relations to Four-Loop Order in Perturbative QCD*, *Phys. Rev. Lett.* **114** (2015) 142002 [[hep-ph/1502.01030](#)].
- [17] ATLAS collaboration, G. Aad et al., *Determination of the top-quark pole mass using $t\bar{t}$ + 1-jet events collected with the ATLAS experiment in 7 TeV pp collisions*, *JHEP* **10** (2015) 121 [[hep-ex/1507.01769](#)].
- [18] CMS collaboration, V. Khachatryan et al., *Measurement of the $t\bar{t}$ production cross section in the $e\mu$ channel in proton-proton collisions at $\sqrt{s} = 7$ and 8 TeV*, *JHEP* **08** (2016) 029 [[hep-ex/1603.02303](#)].
- [19] V. S. Fadin and V. A. Khoze, *Threshold Behavior of Heavy Top Production in e^+e^- Collisions*, *JETP Lett.* **46** (1987) 525.
- [20] V. S. Fadin and V. A. Khoze, *Production of a pair of heavy quarks in e^+e^- annihilation in the threshold region*, *Sov. J. Nucl. Phys.* **48** (1988) 309.
- [21] M. J. Strassler and M. E. Peskin, *The Heavy top quark threshold: QCD and the Higgs*, *Phys. Rev.* **D43** (1991) 1500.
- [22] M. Beneke, Y. Kiyo, A. Maier and J. Piclum, *Near-threshold production of heavy quarks with $Q\bar{Q}$ threshold*, *Comput. Phys. Commun.* **209** (2016) 96 [[hep-ph/1605.03010](#)].
- [23] A. H. Hoang and M. Stahlhofen, *The Top-Antitop Threshold at the ILC: NNLL QCD Uncertainties*, *JHEP* **05** (2014) 121 [[hep-ph/1309.6323](#)].
- [24] S. Gusken, J. H. Kuhn and P. M. Zerwas, *Threshold behavior of top production in e^+e^- annihilation*, *Phys. Lett.* **B155** (1985) 185.
- [25] I. I. Y. Bigi, Y. L. Dokshitzer, V. A. Khoze, J. H. Kuhn and P. M. Zerwas, *Production and decay properties of ultraheavy quarks*, *Phys. Lett.* **B181** (1986) 157.
- [26] M. Martinez and R. Miquel, *Multiparameter fits to the $t\bar{t}$ threshold observables at a future e^+e^- linear collider*, *Eur. Phys. J.* **C27** (2003) 49 [[hep-ph/0207315](#)].
- [27] K. Seidel, F. Simon, M. Tesar and S. Poss, *Top quark mass measurements at and above threshold at CLIC*, *Eur. Phys. J.* **C73** (2013) 2530 [[hep-ex/1303.3758](#)].
- [28] T. Horiguchi, A. Ishikawa, T. Suehara, K. Fujii, Y. Sumino, Y. Kiyo et al., *Study of top quark pair production near threshold at the ILC*, [hep-ex/1310.0563](#).

- [29] J. Gao and H. X. Zhu, *Top Quark Forward-Backward Asymmetry in e^+e^- Annihilation at Next-to-Next-to-Leading Order in QCD*, *Phys. Rev. Lett.* **113** (2014) 262001 [[hep-ph/1410.3165](#)].
- [30] J. Gao and H. X. Zhu, *Electroweak production of top-quark pairs in e^+e^- annihilation at NNLO in QCD: the vector current contributions*, *Phys. Rev.* **D90** (2014) 114022 [[hep-ph/1408.5150](#)].
- [31] L. Chen, O. Dekkers, D. Heisler, W. Bernreuther and Z.-G. Si, *Top-quark pair production at next-to-next-to-leading order QCD in electron positron collisions*, *JHEP* **12** (2016) 098 [[hep-ph/1610.07897](#)].
- [32] L. Guo, W.-G. Ma, R.-Y. Zhang and S.-M. Wang, *One-loop QCD corrections to the $e^+e^- \rightarrow W^+W^-b\bar{b}$ process at the ILC*, *Phys. Lett.* **B662** (2008) 150 [[hep-ph/0802.4124](#)].
- [33] S. Liebler, G. Moortgat-Pick and A. S. Papanastasiou, *Probing the top-quark width through ratios of resonance contributions of $e^+e^- \rightarrow W^+W^-b\bar{b}$* , *JHEP* **03** (2016) 099 [[hep-ph/1511.02350](#)].
- [34] B. Chokouf  Nejad, W. Kilian, J. M. Lindert, S. Pozzorini, J. Reuter and C. Weiss, *NLO QCD predictions for off-shell $t\bar{t}$ and $t\bar{t}H$ production and decay at a linear collider*, *JHEP* **12** (2016) 075 [[hep-ph/1609.03390](#)].
- [35] C. Weiss, B. Chokouf  Nejad, W. Kilian and J. Reuter, *Automated NLO QCD Corrections with WHIZARD*, *PoS EPS-HEP2015* (2015) 466 [[hep-ph/1510.02666](#)].
- [36] J. Alwall, R. Frederix, S. Frixione, V. Hirschi, F. Maltoni, O. Mattelaer et al., *The automated computation of tree-level and next-to-leading order differential cross sections, and their matching to parton shower simulations*, *JHEP* **07** (2014) 079 [[hep-ph/1405.0301](#)].
- [37] W. Beenakker, S. C. van der Marck and W. Hollik, *e^+e^- annihilation into heavy fermion pairs at high-energy colliders*, *Nucl. Phys.* **B365** (1991) 24.
- [38] J. Fleischer, A. Leike, T. Riemann and A. Werthenbach, *Electroweak one loop corrections for e^+e^- annihilation into $t\bar{t}$ including hard bremsstrahlung*, *Eur. Phys. J.* **C31** (2003) 37 [[hep-ph/0302259](#)].
- [39] T. Hahn, W. Hollik, A. Lorca, T. Riemann and A. Werthenbach, *$O(\alpha)$ electroweak corrections to the processes $e^+e^- \rightarrow \tau^-\tau^+$, $c\bar{c}$, $b\bar{b}$, $t\bar{t}$: a comparison*, in *Proc. 4th ECFA / DESY Workshop on Physics and Detectors for a 90-GeV to 800-GeV Linear e^+e^- Collider: Amsterdam, Netherlands, April 2003*, 2003, [[hep-ph/0307132](#)].
- [40] P. H. Khien, J. Fujimoto, T. Ishikawa, T. Kaneko, K. Kato, Y. Kurihara et al., *Full $\mathcal{O}(\alpha)$ electroweak radiative corrections to $e^+e^- \rightarrow t\bar{t}\gamma$ with GRACE-Loop*, *Eur. Phys. J.* **C73** (2013) 2400 [[hep-ph/1211.1112](#)].
- [41] B. D. Pecjak, D. J. Scott, X. Wang and L. L. Yang, *Resummed differential cross sections for top-quark pairs at the LHC*, *Phys. Rev. Lett.* **116** (2016) 202001 [[hep-ph/1601.07020](#)].
- [42] S. Fleming, A. H. Hoang, S. Mantry and I. W. Stewart, *Jets from massive unstable particles: Top-mass determination*, *Phys. Rev.* **D77** (2008) 074010 [[hep-ph/0703207](#)].
- [43] S. Fleming, A. H. Hoang, S. Mantry and I. W. Stewart, *Factorization approach for top mass reconstruction at high energies*, *eConf* **C0705302** (2007) LOOP06 [[hep-ph/0710.4205](#)].
- [44] B. Grzadkowski, M. Iskrzynski, M. Misiak and J. Rosiek, *Dimension-six terms in the Standard Model Lagrangian*, *JHEP* **10** (2010) 085 [[hep-ph/1008.4884](#)].
- [45] R. Barbieri, A. Pomarol, R. Rattazzi and A. Strumia, *Electroweak symmetry breaking after LEP1 and LEP2*, *Nucl. Phys.* **B703** (2004) 127 [[hep-ph/0405040](#)].

- [46] J. D. Wells and Z. Zhang, *Effective theories of universal theories*, *JHEP* **01** (2016) 123 [[hep-ph/1510.08462](#)].
- [47] J. D. Wells and Z. Zhang, *Renormalization group evolution of the universal theories EFT*, *JHEP* **06** (2016) 122 [[hep-ph/1512.03056](#)].
- [48] D. Barducci et al., *Interpreting top-quark LHC measurements in the standard-model effective field theory*, [hep-ph/1802.07237](#).
- [49] J. A. Aguilar-Saavedra, *Effective four-fermion operators in top physics: A roadmap*, *Nucl. Phys.* **B843** (2011) 638 [[hep-ph/1008.3562](#)].
- [50] S. L. Glashow, J. Iliopoulos and L. Maiani, *Weak Interactions with Lepton-Hadron Symmetry*, *Phys. Rev.* **D2** (1970) 1285.
- [51] N. Cabibbo, *Unitary Symmetry and Leptonic Decays*, *Phys. Rev. Lett.* **10** (1963) 531.
- [52] M. Kobayashi and T. Maskawa, *CP Violation in the Renormalizable Theory of Weak Interaction*, *Prog. Theor. Phys.* **49** (1973) 652.
- [53] K. Agashe et al., *Snowmass 2013 Top quark working group report*, in *Proc. Community Summer Study 2013: Snowmass on the Mississippi (CSS2013): Minneapolis, MN, USA, 29 July–6 August 2013*, 2013, [hep-ph/1311.2028](#).
- [54] S. Bejar, J. Guasch and J. Sola, *FCNC top quark decays beyond the standard model*, in *Proc. 5th Int. Symp. on Radiative Corrections (RADCOR 2000): Carmel, CA, USA, Sept. 2000*, 2001, [hep-ph/0101294](#).
- [55] L. Diaz-Cruz and C. Pagliarone, *Perspectives of detecting CKM-suppressed top quark decays at ILC*, in *Proc. Int. Conf.: New Trends in High-Energy Physics: Yalta, Crimea, Ukraine, Sept. 2006*, 2006, [hep-ph/0612120](#).
- [56] B. Mele, *Top quark rare decays in the standard model and beyond*, in *Proc. 14th Int. Workshop, High energy physics and quantum field theory (QFTHEP'99): Moscow, Russia, 17 May–2 June, 1999*, 1999, [hep-ph/0003064](#).
- [57] GEANT4 collaboration, S. Agostinelli et al., *GEANT4: A simulation toolkit*, *Nucl. Instrum. Meth.* **A506** (2003) 250.
- [58] J. Allison et al., *Geant4 developments and applications*, *IEEE Trans. Nucl. Sci.* **53** (2006) 270.
- [59] CLICDP collaboration, C. Grefe et al., *ILCDIRAC, a DIRAC extension for the Linear Collider community*, *J. Phys. Conf. Ser.* **513** (2014) 032077.
- [60] A. Tsaregorodtsev et al., *DIRAC: a community grid solution*, *J. Phys. Conf. Ser.* **119** (2008) 062048.
- [61] W. Kilian, T. Ohl and J. Reuter, *WHIZARD: simulating multi-particle processes at LHC and ILC*, *Eur. Phys. J.* **C71** (2011) 1742 [[hep-ph/0708.4233](#)].
- [62] M. Skrzypek and S. Jadach, *Exact and approximate solutions for the electron nonsinglet structure function in QED*, *Z. Phys.* **C49** (1991) 577.
- [63] T. Sjöstrand, S. Mrenna and P. Z. Skands, *PYTHIA 6.4 physics and manual*, *JHEP* **0605** (2006) 026 [[hep-ph/0603175](#)].
- [64] OPAL collaboration, G. Alexander et al., *A comparison of b and uds quark jets to gluon jets*, *Z. Phys.* **C69** (1996) 543.
- [65] S. Chekanov, M. Demarteau, A. Fischer and J. Zhang, *Effect of PYTHIA8 tunes on event shapes and top-quark reconstruction in e^+e^- annihilation at CLIC*, *CLICdp-Note-2017-005*, 2017.

- [66] Z. Was, *TAUOLA the library for tau lepton decay, and KKMC / KORALB / KORALZ /... status report*, *Nucl. Phys. Proc. Suppl.* **98** (2001) 96 [[hep-ph/0011305](#)].
- [67] K. Fujii, *Physics Study Libraries* <http://www-jlc.kek.jp/subg/offl/physsim/>. Accessed 25 Aug, 2016.
- [68] S. Dittmaier et al., *Handbook of LHC Higgs Cross Sections: 2. Differential Distributions*, *CERN-2012-002* (2012) [[hep-ph/1201.3084](#)].
- [69] P. Mora de Freitas and H. Videau, *Detector simulation with MOKKA / GEANT4: Present and future LC-TOOL-2003-010*, in *Proc. Int. Workshop on Linear Colliders (LCWS 2002): JeJu Island, Korea, 2002*.
- [70] N. Graf and J. McCormick, *Simulator for the linear collider (SLIC): A tool for ILC detector simulations*, *AIP Conf. Proc.* **867** (2006) 503.
- [71] F. Gaede, *Marlin and LCCD: Software tools for the ILC*, *Nucl. Instrum. Meth.* **A559** (2006) 177.
- [72] N. A. Graf, *org.lcsim: Event reconstruction in Java*, *J. Phys. Conf. Ser.* **331** (2011) 032012.
- [73] D. Schulte, *Study of Electromagnetic and Hadronic Background in the Interaction Region of the TESLA Collider*, Ph.D. thesis, Universität Hamburg, TESLA Note-1997-08, 1997.
- [74] M. Thomson, *Particle Flow Calorimetry and the PandoraPFA Algorithm*, *Nucl. Instrum. Meth.* **A611** (2009) 25 [[physics.ins-det/0907.3577](#)].
- [75] J. Marshall, A. Münnich and M. Thomson, *Performance of Particle Flow Calorimetry at CLIC*, *Nucl. Instrum. Meth.* **A700** (2013) 153 [[physics.ins-det/1209.4039](#)].
- [76] J. S. Marshall and M. A. Thomson, *The Pandora Software Development Kit for Pattern Recognition*, *Eur. Phys. J.* **C75** (2015) 439 [[physics.data-an/1506.05348](#)].
- [77] A. Münnich, *Taufinder: A Reconstruction Algorithm for τ Leptons at Linear Colliders*, *LCD-Note-2010-009*, 2010.
- [78] M. Cacciari, G. P. Salam and G. Soyez, *FastJet User Manual*, *Eur. Phys. J.* **C72** (2012) 1896 [[hep-ph/1111.6097](#)].
- [79] S. Catani, Y. Dokshitzer, M. Seymour and B. Webber, *Longitudinally-invariant k_{\perp} -clustering algorithms for hadron-hadron collisions*, *Nucl. Phys. B* **406** (1993) 187.
- [80] S. D. Ellis and D. E. Soper, *Successive combination jet algorithm for hadron collisions*, *Phys. Rev.* **D48** (1993) 3160 [[hep-ph/9305266](#)].
- [81] M. Boronat, J. Fuster, I. Garcia, P. Roloff, R. Simoniello and M. Vos, *Jet reconstruction at high-energy lepton colliders*, *Eur. Phys. J.* **C78** (2016) 144 [[hep-ex/1607.05039](#)].
- [82] F. Simon and L. Weuste, *Light-flavor squark reconstruction at CLIC*, *Eur. Phys. J.* **C75** (2015) 379 [[hep-ex/1505.01129](#)].
- [83] T. Suehara and T. Tanabe, *LCFIPlus: A framework for jet analysis in linear collider studies*, *Nucl. Instrum. Meth.* **A808** (2016) 109 [[physics.ins-det/1506.08371](#)].
- [84] D. E. Kaplan, K. Rehermann, M. D. Schwartz and B. Tweedie, *Top Tagging: A Method for Identifying Boosted Hadronically Decaying Top Quarks*, *Phys. Rev. Lett.* **101** (2008) 142001 [[hep-ph/0806.0848](#)].
- [85] M. Cacciari and G. P. Salam, *Dispelling the N^3 myth for the k_t jet-finder*, *Phys. Lett.* **B641** (2006) 57.
- [86] F. Simon, *Perspectives for Top Quark Physics at the (I)LC*, in *Proc. 7th Int. Workshop on Top Quark Physics (TOP2014): Cannes, France, 28 September-3 October 2014*, 2014, [hep-ex/1411.7517](#).

- [87] A. H. Hoang and C. J. Reisser, *Electroweak absorptive parts in NRQCD matching conditions*, *Phys. Rev. D* **71** (2005) 074022 [[hep-ph/0412258](#)].
- [88] A. H. Hoang, C. J. Reisser and P. Ruiz-Femenia, *Implementing invariant mass cuts and finite lifetime effects in top-antitop production at threshold*, *Nucl. Phys. Proc. Suppl.* **186** (2009) 403 [[hep-ph/0810.2934](#)].
- [89] A. H. Hoang, C. J. Reisser and P. Ruiz-Femenia, *Phase Space Matching and Finite Lifetime Effects for Top-Pair Production Close to Threshold*, *Phys. Rev. D* **82** (2010) 014005 [[hep-ph/1002.3223](#)].
- [90] M. Beneke, B. Jantzen and P. Ruiz-Femenia, *Electroweak non-resonant NLO corrections to $e^+e^- \rightarrow W^+W^-b\bar{b}$ in the t \bar{t} resonance region*, *Nucl. Phys. B* **840** (2010) 186 [[hep-ph/1004.2188](#)].
- [91] M. Beneke, A. Maier, T. Rauh and P. Ruiz-Femenia, *Non-resonant and electroweak NNLO correction to the e^+e^- top anti-top threshold*, *JHEP* **02** (2018) 125 [[hep-ph/1711.10429](#)].
- [92] F. Simon, *A First Look at the Impact of NNNLO Theory Uncertainties on Top Mass Measurements at the ILC*, in *Proc. Int. Workshop on Future Linear Colliders (LCWS15): Whistler, B.C., Canada, 2-6 November 2015*, 2016, [hep-ex/1603.04764](#).
- [93] F. Simon, *Impact of Theory Uncertainties on the Precision of the Top Quark Mass in a Threshold Scan at Future e^+e^- Colliders*, *PoS ICHEP2016* (2017) 872 [[hep-ex/1611.03399](#)].
- [94] S. Lukić, I. Božović Jelisavčić, M. Pandurović and I. Smiljanić, *Correction of beam-beam effects in luminosity measurement in the forward region at CLIC*, *JINST* **8** (2013) P05008 [[physics.acc-ph/1301.1449](#)].
- [95] I. Božović Jelisavčić, S. Lukić, G. Milutinović Dumbelović, M. Pandurović and I. Smiljanić, *Luminosity measurement at ILC*, *JINST* **8** (2013) P08012 [[physics.acc-ph/1304.4082](#)].
- [96] A. H. Hoang, V. Mateu and S. Mohammad Zebarjad, *Heavy Quark Vacuum Polarization Function at $O(\alpha^2(s))$ and $O(\alpha^3(s))$* , *Nucl. Phys. B* **813** (2009) 349 [[hep-ph/0807.4173](#)].
- [97] A. Maier and P. Marquard, *Validity of Padé approximations in vacuum polarization at three- and four-loop order*, *Phys. Rev. D* **97** (2018) 056016 [[hep-ph/1710.03724](#)].
- [98] A. Widl, A. H. Hoang and V. Matheu, *Private communication*, (2018) .
- [99] A. H. Hoang, Z. Ligeti and A. Manohar, *B Decay and the Υ Mass*, *Phys. Rev. Lett.* **82** (1999) 277.
- [100] A. H. Hoang, Z. Ligeti and A. Manohar, *B decays in the ϵ expansion*, *Phys. Rev. D* **59** (1999) 074017.
- [101] A. H. Hoang, *$1S$ and \overline{MS} bottom quark mass from Υ sum rules*, *Phys. Rev. D* **61** (1999) 034005.
- [102] A. H. Hoang, A. Jain, I. Scimemi and I. W. Stewart, *Infrared Renormalization Group Flow for Heavy Quark Masses*, *Phys. Rev. Lett.* **101** (2008) 151602 [[hep-ph/0803.4214](#)].
- [103] A. H. Hoang et al., *The MSR Mass and the $O(\Lambda_{QCD})$ Renormalon Sum Rule*, [hep-ph/1704.01580](#).
- [104] A. H. Hoang, C. Lepenik and M. Preisser, *On the light massive flavor dependence of the large order asymptotic behavior and the ambiguity of the pole mass*, *JHEP* **09** (2017) 099 [[hep-ph/1706.08526](#)].
- [105] A. H. Hoang, P. Ruiz-Femenía and M. Stahlhofen, *Renormalization group improved bottom mass from Υ sum rules at NNLL order*, *JHEP* **2012** (2012) [[hep-ph/1209.0450](#)].

- [106] L. Randall and R. Sundrum, *A Large mass hierarchy from a small extra dimension*, *Phys. Rev. Lett.* **83** (1999) 3370 [[hep-ph/9905221](#)].
- [107] A. Pomarol and J. Serra, *Top quark compositeness: Feasibility and implications*, *Phys. Rev.* **D78** (2008) 074026 [[hep-ph/0806.3247](#)].
- [108] LEP ELECTROWEAK WORKING GROUP, SLD ELECTROWEAK AND HEAVY FLAVOUR GROUPS; ALEPH, DELPHI, L3, OPAL, AND SLD collaboration, S. Schael et al., *Precision electroweak measurements on the Z resonance*, *Phys. Rept.* **427** (2006) 257 [[hep-ex/0509008](#)].
- [109] M. S. Amjad et al., *A precise characterisation of the top quark electro-weak vertices at the ILC*, *Eur. Phys. J.* **C75** (2015) 512 [[hep-ex/1505.06020](#)].
- [110] J. A. Aguilar-Saavedra, M. C. N. Fiolhais and A. Onofre, *Top Effective Operators at the ILC*, *JHEP* **07** (2012) 180 [[hep-ph/1206.1033](#)].
- [111] G. Durieux, M. Perelló, M. Vos and C. Zhang, *Global and optimal probes for the top-quark effective field theory at future lepton colliders*, DESY 18-096, IFIC 18-27, [hep-ph/1807.02121](#).
- [112] W. Bernreuther, L. Chen, I. García, M. Perelló, R. Poeschl, F. Richard et al., *CP-violating top quark couplings at future linear e^+e^- colliders*, *Eur. Phys. J.* **C78** (2018) 155 [[hep-ex/1710.06737](#)].
- [113] D. Atwood and A. Soni, *Analysis for magnetic moment and electric dipole moment form-factors of the top quark via $e^+e^- \rightarrow t\bar{t}$* , *Phys. Rev.* **D45** (1992) 2405.
- [114] M. Davier, L. Duflot, F. Le Diberder and A. Rouge, *The optimal method for the measurement of tau polarization*, *Phys. Lett.* **B306** (1993) 411.
- [115] M. Diehl and O. Nachtmann, *Optimal observables for the measurement of three gauge boson couplings in $e^+e^- \rightarrow W^+W^-$* , *Z. Phys.* **C62** (1994) 397.
- [116] B. Grzadkowski and Z. Hioki, *Optimal observable analysis of the angular and energy distributions for top quark decay products at polarized linear colliders*, *Nucl. Phys.* **B585** (2000) 3 [[hep-ph/0004223](#)].
- [117] P. Janot, *Top-quark electroweak couplings at the FCC-ee*, *JHEP* **04** (2015) 182 [[hep-ph/1503.01325](#)].
- [118] P. H. Khien, E. Kou, Y. Kurihara and F. Le Diberder, *Probing New Physics using top quark polarization in the $e^+e^- \rightarrow t\bar{t}$ process at future Linear Colliders*, in *Proc. TYL-FJPPPL workshops on "Top Physics at ILC"*, 2015, [hep-ph/1503.04247](#).
- [119] I. García, *Future Linear Colliders: Detector R&D, Jet Reconstruction and Top Physics potential*, Ph.D. thesis, Universidad de Valencia, Valencia, CERN-THESIS-2016-214, 2016.
- [120] J. Thaler and K. Van Tilburg, *Identifying Boosted Objects with N-subjettiness*, *JHEP* **03** (2011) 15 [[hep-ph/1011.2268](#)].
- [121] B. List and J. List, *MarlinKinfitt: An object-oriented kinematic fitting package*, *LC-TOOL-2009-001*, 2009.
- [122] B. Nachman, P. Nef, A. Schwartzman, M. Swiatlowski and C. Wanotayaroj, *Jets from Jets: Re-clustering as a tool for large radius jet reconstruction and grooming at the LHC*, *JHEP* **02** (2015) 075 [[hep-ph/1407.2922](#)].
- [123] S. Redford, P. Roloff and M. Vogel, *Physics potential of the top Yukawa coupling measurement at a 1.4 TeV Compact Linear Collider using the CLIC_SiD detector*, *CLICdp-Note-2014-001*, 2014.
- [124] S. Redford, P. Roloff and M. Vogel, *Study of the effect of additional background channels on the top Yukawa coupling measurement at a 1.4 TeV CLIC* *CLICdp-Note-2015-001*, 2015.

- [125] J. Reuter and V. Rothe, *Private communication*, 2018.
- [126] A. Djouadi, J. Kalinowski and P. M. Zerwas, *Measuring the $Ht\bar{t}$ coupling in e^+e^- collisions*, *Mod. Phys. Lett.* **A7** (1992) 1765.
- [127] S. Boselli, R. Hunter and A. Mitov, *Prospects for the determination of the top-quark Yukawa coupling at future e^+e^- colliders*, [hep-ph/1805.12027](#).
- [128] R. M. Godbole, C. Hangst, M. Muhlleitner, S. D. Rindani and P. Sharma, *Model-independent analysis of Higgs spin and CP properties in the process $e^+e^- \rightarrow t\bar{t}\Phi$* , *Eur. Phys. J.* **C71** (2011) 1681 [[hep-ph/1103.5404](#)].
- [129] A. Alloul, B. Fuks and V. Sanz, *Phenomenology of the Higgs effective Lagrangian via FEYNRULES*, *JHEP* **04** (2014) 110 [[hep-ph/1310.5150](#)].
- [130] C. Collaboration, *The Phase-2 Upgrade of the CMS Endcap Calorimeter*, Tech. Rep. CERN-LHCC-2017-023. CMS-TDR-019, CERN, Geneva, Nov, 2017.
- [131] ATLAS Collaboration, *Expected sensitivity of ATLAS to FCNC top quark decays $t \rightarrow Zu$ and $t \rightarrow Hq$ at the High Luminosity LHC*, *ATL-PHYS-PUB-2016-019*, 2016.
- [132] M. Moretti, T. Ohl and J. Reuter, *O'Mega: An Optimizing matrix element generator*, [hep-ph/0102195](#).
- [133] A. L. Read, *Presentation of search results: The CL(s) technique*, *J. Phys.* **G28** (2002) 2693.
- [134] L. Moneta, K. Belasco, K. S. Cranmer, S. Kreiss, A. Lazzaro, D. Piparo et al., *The RooStats Project*, *PoS ACAT2010* (2010) 057 [[physics.data-an/1009.1003](#)].
- [135] H. Khanpour, S. Khatibi, M. Khatiri Yanehsari and M. Mohammadi Najafabadi, *Single top quark production as a probe of anomalous $tq\gamma$ and tqZ couplings at the FCC-ee*, *Phys. Lett.* **B775** (2017) 25 [[hep-ph/1408.2090](#)].
- [136] D. Atwood, L. Reina and A. Soni, *Phenomenology of two Higgs doublet models with flavor changing neutral currents*, *Phys. Rev.* **D55** (1997) 3156 [[hep-ph/9609279](#)].
- [137] F. Staub, *Exploring new models in all detail with SARAH*, *Adv. High Energy Phys.* **2015** (2015) 840780 [[hep-ph/1503.04200](#)].
- [138] G. Panico and A. Wulzer, *The Composite Nambu-Goldstone Higgs*, *Lect. Notes Phys.* **913** (2016) [[hep-ph/1506.01961](#)].
- [139] G. F. Giudice, C. Grojean, A. Pomarol and R. Rattazzi, *The strongly-interacting light Higgs*, *JHEP* **06** (2007) 045 [[hep-ph/0703164](#)].
- [140] R. Rattazzi, V. S. Rychkov, E. Tonni and A. Vichi, *Bounding scalar operator dimensions in 4D CFT*, *JHEP* **12** (2008) 031 [[hep-th/0807.0004](#)].
- [141] K. Agashe, R. Contino, L. Da Rold and A. Pomarol, *A Custodial symmetry for $Zb\bar{b}$* , *Phys. Lett.* **B641** (2006) 62 [[hep-ph/0605341](#)].

A Additional event selection tables

A.1 Radiative events at 1.4 TeV

P(e ⁻) Process	σ [fb]		ϵ_{Pre} [%]		ϵ_{MVA} [%]		N	
	-80%	+80%	-80%	+80%	-80%	+80%	-80%	+80%
$e^+e^- (\rightarrow t\bar{t}) \rightarrow qqql\nu$ ($l = e, \mu$) ^a	16.6	8.7	4.0	5.0	90	92	449	300
$e^+e^- (\rightarrow t\bar{t}) \rightarrow qqql\nu$ ($l = e, \mu$) ^b	30.2	16.0	0.49	0.51	79	82	88	50
$e^+e^- (\rightarrow t\bar{t}) \rightarrow qqql\nu$ ($l = \tau$)	23.2	12.3	0.65	0.65	45	50	51	30
$e^+e^- (\not\rightarrow t\bar{t}) \rightarrow qqql\nu$	72.3	16.5	0.42	0.63	62	73	139	57
$e^+e^- \rightarrow qqqqqq$	116	44.9	0.26	0.29	17	17	39	16
$e^+e^- \rightarrow qqll\nu$	44.1	15.3	0.68	1.3	73	64	162	98
$e^+e^- \rightarrow qqqq$	2,300	347	0.017	0.033	4.6	14	13	12
$e^+e^- \rightarrow qqll$	6,980	1,640	0.0051	0.0044	3.4	18	9	10
$e^+e^- \rightarrow qqll$	2,680	2,530	0.0041	0.0022	13	25	10	11
$e^+e^- \rightarrow qq$	4,840	3,170	0.015	0.0074	10	7.9	55	14

^aKinematic region defined as $\sqrt{s'} \in [400, 900)$ TeV

^b $\sqrt{s'} \notin [400, 900)$ TeV

Table 16: Pre-selection and final event selection efficiencies and expected number of events for the $t\bar{t}$ analysis of radiative events in the interval $400 \text{ GeV} \leq \sqrt{s'} < 900 \text{ GeV}$, assuming 750 fb^{-1} for each polarisation state considered.

P(e ⁻)	σ [fb]		ϵ_{Pre} [%]		ϵ_{MVA} [%]		N	
	-80%	+80%	-80%	+80%	-80%	+80%	-80%	+80%
Process								
$e^+e^- (\rightarrow t\bar{t}) \rightarrow qqqqlv$ ($l = e, \mu$) ^a	11.0	5.79	33	30	86	85	2,352	1,116
$e^+e^- (\rightarrow t\bar{t}) \rightarrow qqqqlv$ ($l = e, \mu$) ^b	35.8	18.9	6.3	5.5	80	81	1,349	631
$e^+e^- (\rightarrow t\bar{t}) \rightarrow qqqqlv$ ($l = \tau$)	23.2	12.3	10	9.5	34	27	618	241
$e^+e^- (\not\rightarrow t\bar{t}) \rightarrow qqqqlv$	72.3	16.5	3.7	9.5	49	34	994	405
$e^+e^- \rightarrow qqqqqq$	116	44.9	2.5	2.8	7.9	7.3	170	68
$e^+e^- \rightarrow qqlllv$	44.1	15.3	3.0	4.8	62	55.9	619	311
$e^+e^- \rightarrow qqqq$	2,300	347	0.24	0.39	2.2	3.2	90	32
$e^+e^- \rightarrow qqlv$	6,980	1,640	0.042	0.021	3.2	8.6	69	22
$e^+e^- \rightarrow qqll$	2,680	2,530	0.024	0.016	6.4	6.8	31	21
$e^+e^- \rightarrow qq$	4,840	3,170	0.18	0.14	4.4	6.4	291	218

^aKinematic region defined as $\sqrt{s'} \in [900, 1200)$ TeV

^b $\sqrt{s'} \notin [900, 1200)$ TeV

Table 17: Pre-selection and final event selection efficiencies and expected number of events for the $t\bar{t}$ analysis of radiative events in the interval $900 \text{ GeV} \leq \sqrt{s'} < 1200 \text{ GeV}$, assuming 750 fb^{-1} for each polarisation state considered.

P(e ⁻)	σ [fb]		ϵ_{Pre} [%]		ϵ_{MVA} [%]		N	
	-80%	+80%	-80%	+80%	-80%	+80%	-80%	+80%
Process								
$e^+e^- (\rightarrow t\bar{t}) \rightarrow qqqqlv$ ($l = e, \mu$) ^a	18.4	9.83	37	34	86	88	4,349	2,244
$e^+e^- (\rightarrow t\bar{t}) \rightarrow qqqqlv$ ($l = e, \mu$) ^b	28.5	14.9	3.1	3.3	83	86	550	313
$e^+e^- (\rightarrow t\bar{t}) \rightarrow qqqqlv$ ($l = \tau$)	23.2	12.3	12	13	31	27	639	313
$e^+e^- (\not\rightarrow t\bar{t}) \rightarrow qqqqlv$	72.2	16.5	4.8	7.1	47	63	1,231	553
$e^+e^- \rightarrow qqqqqq$	116	44.9	2.2	2.2	5.2	5.9	102	43
$e^+e^- \rightarrow qqlllv$	44.1	15.3	1.5	2.4	56	65	277	182
$e^+e^- \rightarrow qqqq$	2,300	347	0.45	0.71	1.1	2.0	82	38
$e^+e^- \rightarrow qqlv$	6,980	1,640	0.048	0.026	2.2	6.2	54	20
$e^+e^- \rightarrow qqll$	2,680	2,530	0.031	0.021	3.8	6.5	24	26
$e^+e^- \rightarrow qq$	4,840	3,170	0.30	0.21	1.6	2.7	175	130

^aKinematic region defined as $\sqrt{s'} \geq 1.2 \text{ TeV}$

^b $\sqrt{s'} < 1.2 \text{ TeV}$

Table 18: Pre-selection and final event selection efficiencies and expected number of events for the $t\bar{t}$ analysis of radiative events in the interval $\sqrt{s'} \geq 1200 \text{ GeV}$, assuming 750 fb^{-1} for each polarisation state considered.